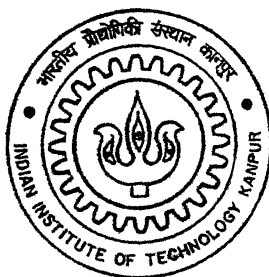


# IN-SITU SYNTHESIS OF $\text{Fe}_x\text{Al}_y\text{-Al}_2\text{O}_3$ COMPOSITE BY ADDITION OF $\text{Fe}_2\text{O}_3$ INTO THE Al-Si MELT

By

Abani Kanta Mohapatra



13  
ME/2002/17  
0725A

DEPARTMENT OF MATERIALS AND METALLURGICAL ENGINEERING

INDIAN INSTITUTE OF TECHNOLOGY KANPUR

OCTOBER, 2003

# **IN-SITU SYNTHESIS OF $\text{Fe}_x\text{Al}_y\text{-Al}_2\text{O}_3$ COMPOSITE BY ADDITION OF $\text{Fe}_2\text{O}_3$ INTO THE Al-Si MELT**

*A thesis submitted in partial fulfillment of the  
Requirements for the Degree of*

**MASTER OF TECHNOLOGY**

*By*

**Abani Kanta Mohapatra**



*to the*

**DEPARTMENT OF MATERIALS AND METALLURGICAL ENGINEERING  
INDIAN INSTITUTE OF TECHNOLOGY, KANPUR-208016  
OCTOBER, 2003**

27 III 2003/MME

सुखोत्तम गैवाय केलकर बुध्दभण्ड  
भारतीय प्रौद्योगिकी संस्थान मुंबई  
प्राप्ति क्र० A...148415...

TH

MME/2003/M

M725i

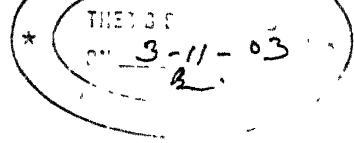


A148415

DEDICATED  
TO

*Late Dr. N. K. BATRA.*





# CERTIFICATE

This is to certify that the work contained in the thesis entitled "In-situ synthesis of Fe-Al<sub>3</sub>-Al<sub>2</sub>O<sub>3</sub> composites by addition of Fe<sub>2</sub>O<sub>3</sub> into the Al-Si melt" by Abani Kanta Mohapatra (Roll No- Y120601), has been carried out under my supervision and to the best of my knowledge this work has not been submitted elsewhere for a degree.

for Late Dr. ~~N. K.~~ BATRA.

Professor

Department of Materials

and Metallurgical Engineering.

I.I.T. Kanpur.

# ACKNOWLEDGEMENT

With a profound sense of gratitude, I express my sincere thanks to my esteemed thesis supervisor late Prof N K. BATRA for his invaluable guidance and encouragement through out this work. I am indebted to him for providing me all the facilities and help in every possible way at I.I.T. KANPUR.

I sincerely acknowledge the help and support rendered by Prof. V S. R MURTHY in correcting my thesis.

I would also like to gratefully acknowledge Dr. M. N. Mounle, Mr. U. S. Singh, B. K. Jain, Suren and Mr. Sharma who has helped me throughout the experimental work, carried out in the laboratory. Thanks are due to all my friends who have made my stay at IIT Kanpur a memorable and pleasant.

Finally, I would like to thank my parents and sisters, who have been a constant source of moral encouragement and inspiration to me.

Abani Kanta Mohapatra.

## LIST OF SYMBOLS

---

$T_1$	Ignition temperature
$t_i$	Time of ignition, respectively;
$\lambda_{\text{eff}}$	Effective thermal conductivity of the bed of particulate reactants
$k$	Reaction rate constant at the ignition temperature
$\eta$	Degree of advancement of reaction
$\Delta H_r$	Enthalpy of the reaction
$T$	Temperature (Kelvin)
$t$	Time of immersion
$\lambda$	Wavelength
$R_B$	Rockwell hardness (B scale)
$W$	Width
$h$	Thickness
$D$	Diameter
$A$	Cross sectional area
MMCs	Metal matrix composites
ODS	Oxide dispersion strengthening
DIMOX	Directed metal oxidation
PRIMEX	Pressureless metal infiltration
$C^4$	Co-continuous ceramic composite processing
RMP	Reactive metal penetration
HIP	Hot isostatic pressing

SHS	Self-propagating high temperature synthesis
AMCs	Aluminium matrix composites
SQC	Squeeze-casting
GPI	Gas pressure infiltration
3A	Aluminium Aluminide Alloys
MA	Mechanical alloying
P/M	Powder metallurgy
MASHS	Mechanically activated self-propagating high temperature synthesis
SEM	Scanning electron microscopy
XRD	X-ray Diffraction
DTA	Differential Thermal Analysis
EDX	Energy Dispersive X-ray
BSE	Back-scattered electron
EDS	Energy Dispersive Spectra
UTM	Universal Testing Machine

# CONTENTS

CERTIFICATE .....	iii
ACKNOWLEDGEMENTS .....	v
LIST OF SYMBOLS .....	v
CONTENTS .....	vii
LIST OF TABLES .....	x
LIST OF FIGURES .....	xii
ABSTRACT .....	xvii
CHAPTER 1: INTRODUCTION .....	1
1.1 Definition .....	1
1.2 Classification of composites .....	2
1.3 Processing of metal matrix composite .....	2
1.3.1 Solid-state processes .....	2
1.3.2 Liquid-state processes .....	3
1.3.3 Other fabrication techniques .....	4
1.3.4 In-Situ Composite processing .....	5
1.4 Aluminum Matrix Composites (AMCs) .....	6
References .....	8
CHAPTER 2: LITERATURE REVIEW .....	10
2.1 Introduction .....	10
2.2 Basic principle of combustion synthesis .....	11
2.3 Alumina Aluminide Alloys by in-situ exothermic reactions (3A process)....	13
2.3.1 Processing .....	13
2.3.2 Densification behavior .....	14
2.3.2 Microstructural studies .....	14
2.3.3 Mechanical properties .....	14
2.4 Alumina Aluminide Alloys by in-situ exothermic reactions (MA process)....	15
2.4.1 Processing .....	15
2.4.2 Consolidation .....	16
2.4.3 Microstructural studies .....	17

2.5 Aluminium-iron oxide system .....	18
2.5.1 Processing .....	18
2.5.2 Characterization .....	19
2.6 Reaction between molten aluminium and iron sample .....	23
2.6.1 Processing .....	25
2.6.2 Characterization .....	25
References .....	29
CHAPTER 3: EXPERIMENTAL PROCEDURE .....	34
3.1 Introduction .....	34
3.2 Raw materials .....	34
3.3 Melting and composite preparation .....	34
3.3.1 Pure Al melts .....	34
3.3.2 Melts with pure Fe additions .....	35
3.3.3 Melts with iron oxide addition .....	35
3.3.4 Melts with $\text{Al}_2\text{O}_3$ or SiC additions .....	36
3.4 Preparation of tensile test coupons .....	36
3.5 Characterization techniques .....	36
3.5.1 X-Ray diffraction analysis .....	36
3.5.2 Optical microscopy .....	37
3.6 Mechanical testing .....	37
3.6.1 Tensile test .....	37
3.6.2 Hardness test .....	37
CHAPTER 4: RESULTS AND DISSCUSSIONS .....	38
4.1 Introduction .....	38
4.2 Microstructure and mechanical properties of Al-Si alloy at different temperatures .....	38
4.3 Microstructure and mechanical properties of Al-Si-Fe at different temperatures .....	39
4.4 Microstructure and mechanical properties of Al-Si- $\text{Fe}_2\text{O}_3$ at different temperatures .....	41

4.5 Microstructure and mechanical properties of particulate (Al/Al<sub>2</sub>O<sub>3</sub> and Al/SiC) composites .....42

4.6 Comparison of in-situ composites with Al/Al<sub>2</sub>O<sub>3</sub> and Al/SiC composites.....43

CHAPTER 5: CONCLUSIONS .....44

Suggestion for future work .....46

## LIST OF TABLES

---

Table 2.1 Heat capacity of different materials [51].....	[47]
Table 2.2 Crystal structure and stability range of the phases formed in Fe–Al binary system at room temperature) [44, 76].....	[47]
Table 2.3 Thermodynamic constants for the intermetallic phases form in Fe–Al binary system [62].....	[47]
Table 2.4 Phase reactions in Fe–Al phase diagram [76].....	[48]
Table 3.1 Weight gain of pure cast Al-Si in various conditions.....	[49]
Table 3.2 Weight gain, loss of pure Al-Si/Fe when Fe was inserted into the Al melt at temp 800°C / 1100°C.....	[50]
Table 3.3 Weight loss or gain when iron ore added to the Al-Si melt at different temperatures i.e. 800°C/1100°C.....	[51]
Table 4.1 Mechanical properties of cast Al-Si alloy at various conditions.....	[52]
Table 4.2 Mechanical properties of cast Al- Si alloy with pure Fe at various conditions. ....	[53]
Table 4.3 Mechanical properties of cast Al- Si alloy with Fe <sub>2</sub> O <sub>3</sub> at various conditions... ..	[54]



Table 4.4 Mechanical properties of cast Al- Si alloy with 2% Al<sub>2</sub>O<sub>3</sub> at 1100°C... [55]

Table 4.5 Mechanical properties of cast Al-Si alloy with 2% SiC at 1100°C..... [56]

# LIST OF FIGURES

---

Fig. 1.1 Classification of in situ Composites.....	[57]
Fig. 2.1(a) Schematic representation of SHS process.....	[58]
Fig. 2.1(b) Schematic representation of the temperature profile associated with passage of a combustion front.....	[59]
Fig. 2.1(c) Schematic representation of combustion wave propagation: (a) Steady state, (b) Oscillatory, (c) Spin.....	[60]
Fig. 2.2 Two different 3A processing routes.....	[61]
Fig. 2.3 Transmission electron micrographs of the shock consolidated specimens of (a) Al-10.7 pct Fe powder MA for 65h and (b) Al-25 pct Fe powder MA for 15h showing the presence of 25-30 nm nanocrystals [21].....	[62]
Fig. 2.4 A plot showing the summary of results of MA in different powder mixtures [21].....	[63]
Fig. 2.5 Scanning electron micrographs of the Al-4 pct Fe powder (a) as-blended (b) milled for 10h and (c) milled for 20h showing a decrease in the particle size with milling time [21].....	[64]
Fig. 2.6 Scanning electron micrograph of the Al-10.7 pct Fe powder MA for 30h, showing the presence of nanometer sized particles [21].....	[64]

Fig. 2.7 Backscattered SEM micrograph showing the cross section of the aluminum and  $\text{Fe}_2\text{O}_3$  interface reacted at  $1000^\circ\text{C}$  for 2 hours. A: Al, B:  $\text{Al}_2\text{O}_3$  and  $\text{FeAl}_x$  composite. C:  $\text{FeO}_x$  phase i, D:  $\text{FeO}_x$  phase 1, E:  $\text{FeO}_x$  phase ii, F:  $\text{Fe}_2\text{O}_3$  [23]..... [65]

Fig. 2.8 DTA spectra of mixed Al/ $\text{Fe}_2\text{O}_3$  samples. Top: pressed pellet, bottom: powder sample [23]..... [66]

Fig. 2.9 SEM images of the top surface of the pressed discs of Al and  $\text{Fe}_2\text{O}_3$  after a reaction at  $960^\circ\text{C}$  or  $1060^\circ\text{C}$  for 1 hour in an argon atmosphere. (a).  $960^\circ\text{C}$ , (b),  $1060^\circ\text{C}$  [23]..... [67]

Fig. 2.10 X-ray diffraction patterns of the reaction products between Al and  $\text{Fe}_2\text{O}_3$  Top: spectrum of the sample reacted at  $960^\circ\text{C}$  in powder form, middle: spectrum of the sample reacted at  $1060^\circ\text{C}$ . peak A: Al, peak B: Fe, peak C:  $\text{Fe}_2\text{O}_3$ , peak D:  $\text{Al}_2\text{O}_3$ , peak E:  $\text{Fe}_3\text{O}_4$ , peak F:  $\text{FeAl}_2\text{O}_4$  [23]..... [68]

Fig. 2.11 SEM image of the cross section of the reaction product between Al and  $\text{Fe}_2\text{O}_3$  at  $960^\circ\text{C}$ . A: Al, D:  $\text{Al}_2\text{O}_3$ , E:  $\text{Fe}_3\text{O}_4$  [23]..... [69]

Fig. 2.12 SEM images of the cross section of Al and  $\text{Fe}_2\text{O}_3$  reacted at  $1060^\circ\text{C}$ , (a), the region near to the top of the surface showing a layer of Fe or Iron oxide formed on the surface, (b), needle shaped single crystals of Fe or its oxide (labeled as C) formed on the top surface, R: embedding resin [23]..... [70]

Fig. 2.13 Phase diagram of Fe-Al-O at  $1000^\circ\text{C}$ . sp =  $\text{Fe}(\text{Fe},\text{Al})_2\text{O}_4$  spinel, W= Wustite, ss =solid solution [23]..... [71]

Fig. 2.14 Schematic view of the device used for immersion tests [51]..... [72]

Fig. 2.15 BSE micrographs of the interface layer to show the formation of both $\text{FeAl}_3$ and $\text{Fe}_2\text{Al}_5$ intermetallic phases (a, b), and cracking and detachment of the $\text{FeAl}_3$ (c) [51]..	[73]
Fig. 2.16 EDS spectra of the intermetallic phases in Fig. 2.15 [51].....	[74]
Fig. 2.17 XRD spectra of phases formed within iron coupons dipped into molten aluminum [51].....	[75]
Fig. 2.18 Intermetallic compounds observed between solid iron and liquid aluminium at $T=800^\circ\text{C}$ : (a) and (b), optical micrographs, respectively for $t=30\text{ s}$ and $t=30\text{ min}$ ; (c) scanning electron micrograph showing $\text{Fe}_2\text{Al}_5$ and $\text{FeAl}_3$ formed after an immersion time equal to 15 min [51].....	[76]
Fig. 2.19 Al-Fe phase diagram [44].....	[77]
Fig. 2.20 Temperature dependence of the $\text{Fe}_2\text{Al}_5$ layer thickness: (a) $t=30\text{ s}$ ; (b) $t=15\text{ min}$ [51].....	[78]
Fig. 2.21 Thickness loss of the solid versus temperature for two immersion times [51].....	[79]
Fig. 2.22 Variation of the layer average thickness with $t^{1/2}$ at $T=800^\circ\text{C}$ : (a) $\text{Fe}_2\text{Al}_5$ ; (b) $\text{FeAl}_3$ [51].....	[80]
Fig. 2.23 Microstructure of the interface zone ( $T=800^\circ\text{C}$ , $t=15\text{ min}$ ) after etching: Fe is etched with 5% Nital and $\text{Fe}_2\text{Al}_5$ is etched with 10% NaOH [51].....	[81]
Fig 3.1 Dimension of tensile test specimen die.....	[82]

Fig 4.1 XRD pattern of cast Al-Si base alloy (a) at 800°C, (b) at 1100°C.. [83]

Fig. 4.2 Shows the optical micrograph of cast Al- Si base alloy at 200 X. (a), (b) at 800°C, and (c) at 1100°C. Micrograph shows the Si flakes along with some modified Si and some distributed alumina..... [84]

Fig. 4.3 XRD pattern of cast Al-Si base alloy with pure Fe (a) at 800°C, (b) at 1100°C ..... [85]

Fig. 4.4 Shows the optical micrograph of cast Al- Si base alloy with pure Fe at 200 X. (a) at 800°C, (b) and (c) at 1100°C. Micrograph shows the presence of distributed alumina in the Al- Si matrix..... [86]

Fig. 4.5 XRD pattern of cast Al-Si base alloy with 5% Fe<sub>2</sub>O<sub>3</sub> (a) at 800°C, (b) at 1100°C. .... [87]

Fig. 4.6 Shows the optical micrograph of cast Al- Si base alloy with 5% Fe<sub>2</sub>O<sub>3</sub> at 200 X. (a) at 800°C, (b) and (c) at 1100°C. Micrograph shows the presence of distributed alumina in the Al- Si matrix..... [88]

Fig. 4.7 XRD pattern of cast Al-Si base alloy with 2% Fe<sub>2</sub>O<sub>3</sub> at 1100°C. .... [89]

Fig. 4.8 Shows the optical micrograph of cast Al- Si base alloy with 2% Fe<sub>2</sub>O<sub>3</sub> at 200 X. (a) and (b) both are at 1100°C. Micrograph shows the presence of distributed alumina in the Al- Si matrix..... [90]

Fig. 4.9 XRD pattern of cast Al-Si base alloy with 2% SiC at 1100°C. .... [91]

Fig. 4.10 Shows the optical micrograph of cast Al- Si base alloy with 2% SiC at 200 X. (a) and (b) both are at 1100°C. Micrograph shows the presence of distributed alumina in the Al- Si matrix..... [92]

Fig. 4.11 XRD pattern of cast Al-Si base alloy with 2% Al<sub>2</sub>O<sub>3</sub> at 1100°C... [93]

Fig. 4.12 Shows the optical micrograph of cast Al- Si base alloy with 2% Al<sub>2</sub>O<sub>3</sub> at 200 X. (a) and (b) both are at 1100°C. Micrograph shows the presence of distributed alumina in the Al- Si matrix..... [94]

Fig. 4.13 Comparison of XRD pattern between (a) 2 % (b) 5 % Fe<sub>2</sub>O<sub>3</sub> at 1100°C. .... [95]

Fig. 4.14 Hardness comparison of different samples prepared with different composition. .... [96]

Fig. 4.15 Harrdness comparision of Al-Si- 2% Fe<sub>2</sub>O<sub>3</sub> and Al-Si- 5% Fe<sub>2</sub>O<sub>3</sub> at 1100°C. .... [97]

Fig. 4.16 Strength comparison of different samples prepared with different composition. .... [98]

Fig. 4.17 Strength comparison of Al-Si- 2% Fe<sub>2</sub>O<sub>3</sub> and Al-Si- 5% Fe<sub>2</sub>O<sub>3</sub> at 1100°C. .... [99]

# CHAPTER 1

## INTRODUCTION

---

### 1.1 Definition

A composite may be defined as a material produced via a physical combination of pre-existing ingredient materials to obtain a new material with unique properties when compared to the monolithic material [1]. This definition distinguishes a composite from other multiphase materials which are produced by bulk processes where one or more phases result from phase transformation. The terms matrix and reinforcement are often used to describe composites consist of one or more discontinuous phases embedded in a continuous phase. The discontinuous phase is usually harder and stronger than the continuous phase and is called the “reinforcement”, whereas the continuous phase is termed as the “matrix”. The matrix is a percolating “soft” phase with excellent ductility, formability and thermal conductivity while reinforcements exhibit high stiffness and low thermal expansion. The reinforcements can be continuous or discontinuous, orientated or random. As per recent definition, composites are considered as materials consisting of two or more chemically distinct constituents, on a macroscale, with a distinct interface separating them. Different components in a composite do not dissolve or completely merge [2]. They maintain an interface between matrix and reinforcement and act in coherent manner to provide synergetic characteristics not obtainable by any of the original components acting singly. Composites consist of one or more discontinuous phases embedded in a continuous phase. Composite materials have many advantages over conventional materials because of their superior performance in terms of mechanical properties e.g., strength, stiffness, toughness, high-temperature performance.

## **1.2 Classification of composites**

The composites are classified by [3]: (a) their matrix (polymer, ceramic, metal), (b) their reinforcement, which includes the chemical nature (oxides, carbides, nitrides) shape (continuous fibers, short fibers, whiskers, particulates) and orientation (random or aligned), (c) their processing routes e.g. solid state, liquid state, and in-situ processing.

These composites find application in many engineering applications (especially metal matrix composites). Hence the main focus of current research is on metal matrix composites (MMCs).

Metal matrix composites (MMCs) are a class of advanced engineering materials in which a strong ceramic reinforcement is incorporated into a metal matrix to tailor its physical, mechanical and tribological properties for specific applications according to the design requirements [4]. MMCs, especially Al base composites, play an important role in aerospace, automotive applications. Metal matrix composites are reported to have advantages such as high temperature hardness, high strength, high elastic modulus, high toughness, superior impact resistance, improved wear resistance, durability and good thermal shock resistance. Metal matrix composites are known to have disadvantages such as- they possess less ductility than the matrix materials, poor fracture toughness, high production cost.

## **1.3 Processing of metal matrix composite**

In the development of metal matrix composites, the following three processing methods are primarily used: (i) high pressure diffusion bonding, (ii) casting, and (iii) powder metallurgy techniques. More specifically, these processes can also be viewed as solid state, liquid state, plasma spray techniques and in-situ fabrication techniques.

### **1.3.1 Solid-state processes**

Powder metallurgy is the most important route by which metal matrix composites are produced. In the majority of cases, the strengthening phase is a stable oxide usually of another metal. The term ODS (oxide dispersion strengthening) is often used to describe such composites [5]. A number of different processes are available for producing the very fine dispersions. In one process, an alloy is heated in an atmosphere that is reducing to the matrix metal but oxidizing to the second (alloyed) metal is created. The latter is converted to oxide uniformly distributed throughout the matrix. The internal oxidation



process occurs as a result of the diffusion of oxygen through the lattice. In large sections, this is a lengthy process. However, if powder is used, a relatively short oxidizing cycle is required. The matrix metal sometimes in the form of salt is mixed with a solution of another salt of the metal, which has more stable oxide. This mixture is heated in an atmosphere that is reducing to the matrix metal but oxidizing to the second metal to get a composite material. Other composites use fibres or whiskers as the strengthening agent. The most recent process that is used for very high temperature applications (e.g., gas turbines for jet engines) are prepared by mechanical alloying [6]. This process involves milling, usually in an attritor, a mixture of a metal powder and a refractory material are milled for long periods during which the refractory particles are broken up and incorporated in the soft metal. Another class of wrought sintered material that is beginning to make an impact is based on particulate material - powder or a chopped ribbon, that has been solidified and cooled at a very high rate such that metastable non-equilibrium microstructure result in the ribbon. They may be microcrystalline or amorphous. The process is applicable only to certain alloys. One important feature is that the matrix metal can retain in solid solution with a much higher than the equilibrium percentage of the alloying element. Providing that the densification and mechanical working is carried out at a temperature low enough to avoid destroying the non-equilibrium structure, remarkably enhance mechanical properties can be achieved [7]. A major development programme is underway with alloys of Al, Ti, and Mg, the hope being that their use in aircraft structures will significantly reduce the weight and increase the payload.

The main disadvantages associated with solid state processing of composites are: they require long time to manufacture, equipment used is costly and the processes are complex.

### **1.3.2 Liquid-state processes**

The simplest method of liquid infiltration is to pour the molten metal/alloy into a vessel containing the fibres. The method is quite suitable if the fibre-matrix combination is nonreactive [8]. In the case of a mutually reactive fibre-matrix combination (e.g.,

aluminium and silica), each individual fibre may be coated by drawing it singly through a bead of molten metal. Continuous single fibers can be moved very quickly through small metal beads to give adequate coating thicknesses with very little time for the chemical reaction. In this method, the coated fibers must be hot-pressed to make the composite. With less reactive systems (e.g., carbon/aluminium) a fiber tow can be drawn through a crucible containing the molten metal. The fibers can be protected against attack to some degree by a suitable metal coating (e.g., nickel for carbon-aluminium system) or reducing the rate of reaction through lowering the processing temperature obtained as a result of alloying the metal with a substance that reduces its melting point (e.g., 12 % Si in the molten Al reduces the processing temperature from just over 660 to 580°C).

In plasma spray technique, the matrix is sprayed onto the fibers, which are supported on a foil, also made of the matrix material. The resulting tape is very porous, easily deformable, and suitable for cutting to the shape and size required for hot-pressing to the finished product. Here, the metal rapidly cools and freezes in contact with the fibers, and thus minimizes the undesirable interaction between the fibers and the matrix [9].

The main advantages associated with solid state processing of composites are lower production cost, time consumed is less, simple in operation, secondary processes are minimized and intricate shapes can be produced.

### **1.3.3 Other fabrication techniques**

MMCs can also be formed by a chemical vapour deposition process, coextrusion of matrix and pellet-shaped particles producing fibers, or forming fibers in situ during the controlled solidification of some off-eutectic or eutectic alloys. Metal matrix composites reinforced with ceramic particles, fibers, and whiskers are produced [10]. The metal matrix includes Mg, Al, Cu and select alloys and intermetallics such as TiAl, NiAl and FeAl. The reinforcements include a variety of ceramic particles such as B<sub>4</sub>C, SiC, Al<sub>2</sub>O<sub>3</sub>, Fe<sub>2</sub>O<sub>3</sub>, AlN, CBN, mullite, etc.; whiskers of SiC and Si<sub>3</sub>N<sub>4</sub> and various forms of carbon including graphite, diamond and graphite foam. Nanoparticle size (10-100 nm) particles have been infiltrated with exemplary properties of hardness, strength, elongation and

fracture toughness. The reinforcement content in the metal matrix can be varied from about 5% up to about 90% in a graded manner. Multilayer compositions or mixtures containing particles, fibers and whiskers or metals infiltrated in composite systems such as C-C, SiC/SiC and C/SiC etc can also be produced. Examples are engine components such as pistons, blocks, valves, etc., and sporting goods such as golf clubs.

### **1.3.4 In-Situ Composite processing**

In-situ composites are multiphase materials where the reinforcing phase is synthesized with in the matrix during composite fabrication [11]. There are a number of processes and classes of in-situ composites, including processes where the precipitation of reinforcements occurs in the liquid state and processes where precipitation occurs in the solid state. Processes in which precipitation occurs in the liquid state include those occurring with low under cooling, such as traditional and directionally solidified eutectics. Rapid solidification in which a supersaturation is created by rapidly cooling a liquid with the reinforcement constituents already in solution and processes in which a larger supersaturation is created by rapidly bringing the constituents of the reinforcement together to react [12]. Solid state in-situ processes include internal oxidation, displacement reaction, reactive milling, mechanical alloying and cryomilling. The in-situ composite are broadly classified on the basis of reinforcement such as metal-ceramic, intermetallic-ceramic, ceramic-ceramic composites [13]. The metal-ceramic composites are further classified based on reactant phases such as liquid-gas, liquid-solid, and solid-solid reaction based composites. Classification of the in-situ composite and its processing is shown in Fig 1.1. However, these established processing routes e.g directed metal oxidation (DIMOX), co-continuous ceramic composite processing ( $C^4$ ), reactive metal penetration (RMP) are mainly restricted to the manufacturing of aluminium containing composites. For the fabrication of refractory metal or intermetallics composites, methods like gas pressure infiltration, hot extrusion, hot pressing or hot isostatic pressing (HIP) are generally employed but they are expensive. Combustion synthesis or self-propagating high temperature synthesis (SHS) is an innovative technique to produce intermetallic/ceramic composites. In-situ Composites are reported to have advantages such as (i) in-situ formed reinforcements are thermodynamically stable in the matrix, leading to less degradation in elevated temperature service conditions, (ii) in situ formed

reinforcement particles are finer in size and their distribution in the matrix is more uniform (with no segregation of reinforcements), (iii) yield better mechanical properties, (iv) the most impressive feature about this is, the matrix and the reinforcement phases form interpenetrating and interconnected network structure, which is generally not seen in the conventional composites [14]. Keeping aforementioned advantages in mind, several in-situ composites with interpenetrating structures of metal and ceramic are being developed. Reactive Metal Penetration (RMP) is also a novel in-situ method for the development of Al-Al<sub>2</sub>O<sub>3</sub> composite. The process is based on liquid-solid reaction, where molten Al is reacted with a silica perform to produce composites of interconnected aluminium and alumina phases ( $\text{Al} + \text{SiO}_2 \rightarrow \text{Al}_2\text{O}_3 + \text{residual Al with dissolved Si}$ ) [15].

The synthesis of Al-Al<sub>2</sub>O<sub>3</sub> composite by adding Fe<sub>2</sub>O<sub>3</sub> in to the Al melt is one of the example of in-situ composite. Here Fe<sub>2</sub>O<sub>3</sub> is added to the Al melt to produce some Al<sub>2</sub>O<sub>3</sub> particles which uniformly distributed throughout the Al<sub>x</sub>Fe<sub>y</sub> matrix ( $\text{Al} + \text{Fe}_2\text{O}_3 \rightarrow \text{Al}_2\text{O}_3 + \text{residual Al with dissolved Fe}$ ) [16].

## 1.4 Aluminum Matrix Composites (AMCs)

Aluminum is the most popular matrix for the metal matrix composites (MMCs). The Al alloys are quite attractive due to their low density, their capability to be strengthened by precipitation, their good corrosion resistance, high thermal and electrical conductivity, and their high damping capacity [17]. Aluminum matrix composites (AMCs) have been widely studied since the 1920s and are now used in sporting goods, electronic packaging, armours and automotive industries. They offer a large variety of mechanical properties depending on the chemical composition of the Al-matrix. They are usually reinforced by Al<sub>2</sub>O<sub>3</sub>, SiC, C but SiO<sub>2</sub>, B, BN, B<sub>4</sub>C, AlN are also be considered. The aluminum matrices are in general Al-Si, Al-Cu, 2xxx or 6xxx alloys [18]. They are very attractive for their isotropic mechanical properties (higher than their unreinforced alloys) and their low costs (cheap processing routes and low prices of some of the discontinuous reinforcement such as SiC particles or Al<sub>2</sub>O<sub>3</sub> short fibers). There are many

processes viable to fabricate AMCs; they can be classified in: solid state, liquid-state and deposition processes. In solid-state processes, the most spread method is powder metallurgy (P/M); it is usually used for high melting point matrices and avoids segregation effects [19], where brittle reaction product formation prone to occur in liquid state processes. This method permits to obtain discontinuously particle reinforced AMCs with the highest mechanical properties [20]. These AMCs are used for military applications [21] but remain limited for large scale productions. In liquid-state processes, one can distinguish the infiltration processes where the reinforcements form a preform which is infiltrated by the alloy melt with pressure applied by a piston (squeeze-casting, SQC) or by an inert gas (gas pressure infiltration, GPI) and without pressure [22]. In the last case, it can be distinguished the reactive infiltration processes using the wetting between reinforcement and melt obtained by reactive atmosphere, elevated temperature, alloy modification or reinforcement coating (reactive infiltration) and the dispersion processes, such as *stir-casting*, where the reinforcements are particles stirred into the liquid alloy. Process parameters and alloys are to be adjusted to avoid reaction with particles. In deposition processes, droplets of molten metal are sprayed together with the reinforcing phase and collected on a substrate where the metal solidification is completed [23].

This technique has the main advantage that the matrix microstructure exhibits very fine grain sizes and low segregation, but has several drawbacks: the technique can only be used with discontinuous reinforcements, the costs are high, and the products are limited to the simple shapes that by obtained by extrusion, rolling or forging [24].

If one can use in-situ processes (discovered earlier) to produce Al matrix composites, the production cost can be cheaper. Cheap oxide raw materials along with small proportion of metal can be used for producing various shapes. Further, most of these reactions are exothermic in nature and can be processed at very low temperature. Hence in the present investigation  $\text{Al}_2\text{O}_3/\text{Fe}_x\text{Al}_y$  cast composites are produced using in-situ reaction of  $\text{Al}/\text{Fe}_2\text{O}_3$  or  $\text{Al}/\text{Fe}$  and compared with conventional particulate ( $\text{Al}/\text{Al}_2\text{O}_3$  or  $\text{Al}/\text{SiC}$ ) reinforced composites.

## References

1. J. G. Baetz, "Introduction to Composite Material," Vol.13, 1997, 86-89.
2. S. Biswas, S. Nangia and G. Srikanth, "Advanced Composite Mission – An Enabling Mechanism for composite development," 2<sup>nd</sup> Ed, 1994, 122-125.
3. T. L. Richardson, "Composites," 4<sup>th</sup> Ed, 1996, 27-31.
4. A.R Begg, Arnold, "Metal Matrix Composite," 4<sup>th</sup> Ed, 1992, 64-69.
5. S. Lee, Dictionary of Composite Materials, TECHNOMIC publication, 22 (1989).
6. G. Akovali, "Handbook of Composite fabrication," Vol.14, 1987, 118-123.
7. A. Buekers, "Handbook of Composite fabrication," Vol.18, 1989, 227-233.
8. Warren, Ceramic Matrix Composites, Blackie, Glasgow, and London, 1992, 167-196.
9. R. B. Bhagat, Metal Matrix Composites, Processing and Interfaces, 1993, P 43.
10. X. Liu and M. Nilmani, Processing, Properties, and applications of Cast Metal Matrix Composites, 1996, P 297.
11. B.S.S. Daniel, V.S.R. Murthy, and G.S. Murthy, "Metal-Ceramic composites via in-situ methods, "
12. C. McCullough, P. Galuska, and S.R. Pittman. "Criteria for matrix selection in continuous fiber aluminum matrix composites in design fundamentals of high temperature composites, intermetallics and metal-ceramics systems" Vol.5, 1996, 15-28.
13. S.C. Tjong and Z.Y. Ma, "Microstructural and mechanical characteristics of in-situ metal matrix composites," Mater. Sci. and Engg., Vol.29, 2000, 49-113.
14. D.L. Anton, D.M. Shah, D.N. Dulh and F.H. Giamei, "Selecting high-temperature structural intermetallic compounds: the engineering approach," JOM, Vol.41, 1989, 12-17.
15. R. E. Loehman, K. Ewsuk and A. P. Tomsia, "Synthesis of  $\text{Al}_2\text{O}_3$ -Al composites by reactive metal penetration," J. Am. Ceram. Soc., Vol.79, 1996, 27-32.
16. S. Schicker, D.E. Garcia, J. Bruhn, R. Janssen and N. Claussen, "Reaction processing of  $\text{Al}_2\text{O}_3$  composites containing iron and iron aluminides," J. Am. Ceram. Soc., Vol.80, 1997, 2294-2300.

17. E. Neussl,, P.R. Sahm, and H.M. Flower,. Continuous fibre reinforced aluminium matrix composites, the influence of the alloy composition on the mechanical properties. *Advanced Engineering Materials*, Vol.2, 2000, 587-592.
18. R.B. Bhagat, "Composites", Vol.19, 1988, 393.
19. R.B. Bhagat, *J. Mater. Sci.* Vol.24, 1989, 1496.
20. S. Suresh, A. Montensen, A. Needleman (Eds.), *Fundamentals of Metal Matrix Composites*, Butterworth/Heinemann, London, Vol.17, 1993, P 24.
21. J. Surbrahmanyam, M. Vijayakumar, *J. Mater. Sci.* Vol.27, 1992, 6249- 6273.
22. A.W. Urquhart, *Mater. Sci. Eng.* Vol.144, 1991, 75- 82.
23. R.M. Aikin, Jr, *J. Organomet.* Vol.49, 1997, 35- 39.
24. M.J. Koczak, M.K. Premkumar, *J. Min. Met. Mater. Soc.* Vol.45, 1993, 44 -48.

## CHAPTER-2

### LITERATURE REVIEW

---

#### 2.1 Introduction

In this chapter, processing and properties of recently developed in-situ composites are reviewed. Conventionally the term “in-situ” composites has been applied to align two-phase materials in which the reinforcing phase is produced simultaneously with the matrix e.g. directionally solidified eutectic, monotectic and cellular-dendritic polyphase alloys. But today, in-situ composites consist of metals, intermetallics, ceramics and organic compounds whose microstructural control led to new avenues in magnetic, electrical, optical, thermal, chemical and structural applications [1].

Self-propagating high temperature synthesis (SHS) or combustion synthesis is an innovative technique where refractory metal, intermetallic and ceramic composites are produced by in-situ chemical reactions [2-5]. The key principle of this process is conversion of chemical energy to thermal energy. A large amount of heat is generated instantly (in few seconds) and different reactant phases are formed in a short span of time. In this chapter the broad principles of combustion synthesis are outlined. A deviation from combustion synthesis is 3A (Aluminium Aluminide Alloys) process. In 3A process, the reactions are exothermic like in SHS process but are of low intensity. 3A process makes use of cheap oxide powders instead of expensive elemental powders that are generally used in SHS reaction. Additionally, the reaction times in 3A process are much longer compared to conventional combustion synthesis process. The longer times are used to ensure complete reaction of powders. Unlike combustion synthesis, in 3A process, the phases generated attain complete equilibrium due to long reaction times. Moreover, the volume fraction and distribution of phases could be tailored to specific property requirements by controlling the processing variables. The unique feature of composites processed via 3A process is, the microstructures contain bicontinuous networks of intermetallic and ceramic phases. Such



microstructures offer better properties compared to conventional composites. For example, let us consider Al-Fe system, which is the topic of investigation in this thesis. Alumina reinforced iron aluminide composites can be generated using 3A process using the following in-situ chemical reaction:



In the above reaction, there are two sequential steps. The first step is metallothermic reduction of the oxide to the metal, e.g.  $\text{Fe}_2\text{O}_3 \rightarrow \text{Fe}$ . The second step is the formation of the required intermetallic compound or reinforcing ceramic phase i.e.  $\text{Fe} \rightarrow \text{Fe}_x\text{Al}_y$  and  $\text{Al} \rightarrow \text{Al}_2\text{O}_3$ . So, it is also important to understand the reaction between elemental powders (Fe and Al and other related systems), interfacial reaction of Fe-Al and the influence of external parameters like reaction time, alloying elements and operating temperature on the evolution of final microstructures. Keeping this in view, the literature is presented in two different sections. In the first half of the literature review, the basic processing, microstructure and mechanical properties of aluminides obtained by 3A and MA (mechanical alloying) process are summarized. In the later part, the reaction between Al melt with iron oxide and pure iron are reviewed. Finally, most of the aluminides are brittle in nature. It is important to obtain more ductile phases from the viewpoint of mechanical properties. Keeping this in perspective, recent research methodologies adopted for controlling the brittleness are also reviewed [6-10].

## 2.2 Basic principle of combustion synthesis

The main trend in materials science and engineering at present is the extension of materials spectrum by using energy and time efficient technologies, which are also environmentally friendly. One such attempt is combustion synthesis. The distinct feature of combustion synthesis is utilization of exothermic reactions between reactants until complete conversion of reactants to products occurs in a short time [11-13]. The basic principle of combustion synthesis is shown schematically in Fig 2.1a. The reactant powders are mixed and ignited using a DC source or a high-energy beam. Once initiated, highly exothermic reaction can be self-sustaining and will propagate through the reactant mixture in the form of

a combustion wave. As the combustion wave front advances, the reactants are converted to the products. When the ignition takes place, the sample's temperature rises abruptly to a maximum value, which is the adiabatic temperature as shown in **Fig 2.1b**. It has been found that ignition can be realized in system of reactants where the reaction enthalpies are of the order of 100 KJ mole<sup>-1</sup> or higher. For a spherically symmetric bed of particulate reactants and a single reaction the ignition should occur [5] when:

$$(-\Delta H_r) k (T_i, \eta) > \frac{1}{r^2} \frac{\partial}{\partial r} \left[ r^2 \lambda_{\text{eff}} \frac{\partial T}{\partial r} \right]_{t_i} \quad (2.2)$$

Where  $T_i$  ,  $t_i$  are temperature and time of ignition, respectively;  $\eta$  is the degree of advancement of reaction;  $\Delta H_r$  is the enthalpy of the reaction in J mol<sup>-1</sup>;  $k(T_i, \eta)$  is the reaction rate constant (mol m<sup>-3</sup> s<sup>-1</sup>) at the ignition temperature;  $\lambda_{\text{eff}}$  is the effective thermal conductivity of the bed of particulate reactants and  $r$  is the radial position. From the Eq 2.2, it can be seen that the sustainable propagation is possible when the two temperature gradients in the bed remain low. Two major factors are expected to affect temperature gradient in a bed of reacting particles. One is the thermal conductivity of the bed because high conductivity favours high thermal gradients and vice versa. Another factor is the size of reactant particles. In a porous particulate bed, the heat flux from particles increases inversely to the particle size; the smaller the particle size lower will the thermal conductivity of the porous bed. The influence of these factors further varies if liquid is formed during the reaction.

As discussed earlier, once the combustion wave is initiated, the rate of propagation depends on two competing process. They are heat generation and dissipation. Any changes that are brought in these two heat transfer processes can alter the velocity of the front from a steady state to non-steady state. Depending on the propagation of the wave front with time, the combustion process divided further in to oscillatory or a spin motion (**Fig 2.1c**). In the oscillatory mode, the wave moves in successions of rapid and slow displacements, and in the spin mode, the reaction proceeds in a spiral motion from one end to the other. Generally, oscillation motion can be recognized by formation of layered structures in the final product (**Fig 2.1c**).

Sometimes, the instability of combustion wave can lead the reaction from a steady state to unsteady state, ultimately extinguishing the combustion process. Since instability can come from insufficient heat generation, weak exothermic reactions are susceptible to

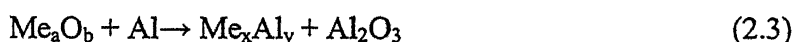
extinction (e.g. formation of SiC, B<sub>4</sub>C and some intermetallics). To sustain such reactions two approaches are adopted. Since the adiabatic temperature is function of the initial temperature of the reactants, preheating of the mixture can help to some extent to push the temperature. This approach is called “thermal explosion”.

## 2.3 Alumina Aluminide Alloys by in-situ exothermic reactions (3A process)

For the low cost manufacturing of Alumina Aluminide Alloys (3A) a novel powder metallurgy technique has been developed. The process involves the reaction sintering of attrition milled powder [14,15] mixtures consisting of cheap raw materials like aluminium, metal oxides (e.g. Fe<sub>2</sub>O<sub>3</sub>, TiO<sub>2</sub>, Nb<sub>2</sub>O<sub>5</sub>, ZrO<sub>2</sub> etc) and/or elemental metals like Fe, Ni, Cr, Mo etc. to produce alumina/aluminide composites with interpenetrating network structures [16,17]. The main advantages of 3A process is that it can be suitably modified to suit industrial production methods.

### 2.3.1 Processing

In general, the processing involves attrition milling (usually 7-10 hours) in acetone media using zirconia balls, subsequently dried and passed through a 200 µm sieve. Green samples were formed by uniaxial pressing at 50 MPa followed by static pressing at 900 MPa. Heat treatments up to 1550 °C were performed in air or in vacuum (10<sup>-3</sup> bar). Using a powder containing metal oxide and aluminium, the reaction sequence includes the aluminothermic reduction as well as the formation of corresponding aluminides. Additionally, Al<sub>2</sub>O<sub>3</sub> is formed in-situ as a product from the reaction between the metal oxide and aluminium. The general reaction scheme is as follows:



Where, Me<sub>x</sub>O<sub>y</sub> refers to any metal oxide, which has a favorable Gibbs free energy for the above reaction. The general fabrication routes for 3A materials are shown in the Fig. 2.2. In the first process (route.a), Al is attrition milled with an oxide powder (MeO). Upon reaction sintering, very small volume fraction of aluminium oxidizes to alumina, and the rest of the aluminium is utilized in reduction of the oxide powder. The reduced powder further reacts to form an in-situ aluminide (Me<sub>x</sub>Al<sub>y</sub>). In the second reaction process (route. b), Al<sub>2</sub>O<sub>3</sub>, Al and metal (metal is suitably chosen to form a desired aluminide) are mechanically milled and

sintered at an appropriate temperature. Most of the aluminium reacts with metal to form respective aluminide, and a small amount of aluminium converts to alumina during processing and increases the total alumina content marginally. In some cases, residual aluminum can also be noticed. Further, by adjusting the starting powder composition, it is possible to vary the final composition of 3A alloys over a wide range. The aluminide/  $\text{Al}_2\text{O}_3$  volume ratio can be tailored in a broad range up to ~60 vol % aluminides. It was hypothesized that the fine  $\text{Al}_2\text{O}_3$  grain size is the main driving force for complete densification of composite on pressureless sintering. The results further indicate that all thermal and compositional treatments known within the intermetallic community can be applied to control the mechanical behavior of the intermetallic phase incorporated in the 3A.

### **2.3.2 Densification behavior**

In case of Fe-Al system, up to 580 °C samples expanded. At temperatures around 1200 °C, samples begin to sinter but while low aluminium (16.8 vol% Al) samples nearly densified with an overall linear shrinkage of 15%. On the contrary, the final shrinkage observed for high aluminium (29.2 vol% Al) is only 5%. Low densification of high Al demonstrated that large amounts of liquid phase have a detrimental effect on the sintering behavior of FeAl/  $\text{Al}_2\text{O}_3$  composites.

### **2.3.3 Microstructural studies**

Microstructure of 3A composites can be tailored in a wide range. Principally there are 3 sources of alumina in any of the 3A process (a) admixed alumina powder, (b) alumina resulted from Al oxidation during milling and (c) alumina from redox reaction. Adjusting the green compaction using these principles, the final metal/ceramic ratio can be varied between 5 and 60 vol % aluminide. Schicker et al. [18] observed, the sample of composition 16.8 Al – 65.1  $\text{Al}_2\text{O}_3$  – 18.1 Fe vol %. Microstructure consisted of ~ 30 vol % of FeAl of size about 1-5  $\mu\text{m}$  and some residual pores not larger than 3  $\mu\text{m}$ . Claussen et al. [17] achieved a microstructure of 3  $\mu\text{m}$  with a composition of the sample 13.1 vol % Al – 64.8 vol %  $\text{Al}_2\text{O}_3$  – 22.1 vol % Fe.

### **2.3.4 Mechanical properties**

Mechanical behavior depends strongly on the processing conditions. Bending strength of 570 MPa have been obtained in the system 16.5 vol. % Al – 64.8 vol. %  $\text{Al}_2\text{O}_3$  – 22.1 vol. % Fe and a VHN of 5.7 GPa. Maximum bending strength of 700 MPa were obtained with 7.4

vol. % Al – 70 vol. %  $\text{Al}_2\text{O}_3$  – 22.6 vol. % Fe, indicating a strong toughening potential by crack bridging of the Fe ligaments. It has been reported that further improvement in mechanical properties may be expected with optimization of milling process and process parameters e.g. green density, initial composition and heating cycle optimization.

## **2.4 Alumina Aluminide Alloys by in-situ exothermic reactions (MA process)**

Mechanical alloying is a solid state powder processing technique involving repeated welding, fracturing and rewelding of particles in a high energy ball mill. The mechanically driven chemical reduction process (mechano synthesis) has a number of advantages over the commercial metal processing techniques. It enables the reduction of metal oxides ( and halides) directly to pure metals or alloys without first having to convert the oxides to pure metals and then to the desired alloy. For P/M applications it allows the direct formation of a powder product without first having to manufacture the bulk alloy and then convert it to the powder form. Additional benefits accrue because the reactions occur at room temperature. Mechanical alloying is capable of synthesizing a variety of equilibrium and non-equilibrium alloy phases starting from blended elemental or prealloyed powders. Disordering of ordered intermetallics and mechanical synthesis of materials could also be done by mechanical alloying method [19, 20]. Mechanical alloying (MA) is a high energy ball milling technique, in which elemental blends are milled to achieve alloying at the atomic level. However, mechanically activated self-propagating high temperature synthesis (MASHS), which is based on a combination of mechanical alloying (MA) and self-propagating high temperature synthesis (SHS). In this process, the powder mixture is mechanically alloyed to produce a nanocrystalline structure and then the SHS reaction initiated by pressing the powder into a pellet and igniting it in a furnace. The prior mechanical alloying step decreases the ignition temperature by as much as 100 °C [2]. Several iron aluminide, niobium aluminide and Mo silicide intermetallics were synthesized by this method.

### **2.4.1 Processing**

The ordered nature of intermetallics leads to attractive elevated temperature properties such as high strength, increased stiffness, and excellent oxidation/ corrosion resistance. These attributes are a result of the reduced dislocation motion (since pairs of

dislocations, namely super dislocations need to move together to retain the ordered nature of the lattice) and low diffusivities. Also, associated with the reduced dislocation activity is the low ambient temperature ductility and fracture toughness, which restricted large scale industrial applications of intermetallics. Hence, several attempts have been made in recent years to overcome this problem. The common routes adopted to improve the room temperature ductility of intermetallics are: (i) reduction in grain size, (ii) disordering of the lattice, to improve the dislocation motion and (iii) modifying the crystal structure of the phase into a more symmetric. e.g cubic one. MA can achieve all the above effects simultaneously and therefore, this processing step is an extremely important step to synthesize intermetallics.

The actual process of mechanical alloying starts with the mixing of the powders in the right proportion and loading the powder mix into the mill along with the grinding medium. This mix is then milled for the desired length of time until a steady state is reached where every powder particle reaches to the same proportion of elements in the powder mix. The milled powder is then consolidated in to bulk shape and heat treated to obtain the desired microstructure and properties. Thus, the important components of the mechanical alloying process are the raw materials, the mill and the process variables [20].

Nominally pure Al (>99.4% and -100 mesh) and Fe (>99.4% and -325 mesh) powders were used as starting powders to make up mixtures containing 1, 4, 7.3, 10.7 and 25 pct Fe, the last composition corresponding to stoichiometric  $\text{Al}_3\text{Fe}$  intermetallic. MA was carried out at room temperature in a SPEX 8000 Mixer mill. The grinding medium was 3/16" diameter hardened 52100 steel balls. For each run approximately 10 g powder mixture and 100 g steel balls were used and milled using forced air cooling [21].

#### **2.4.2 Consolidation**

The Al-10.7 pt and 25 pct Fe powders MA for 65h and 15h, respectively, were consolidated by shock companion techniques [16] to form pellets. Near 100% density was achieved in both the specimens [22]. X-ray diffraction patterns of the consolidated specimens indicate the presence of  $\text{Al}_3\text{Fe}$  and  $\text{Al}_3\text{Fe}_2$  compound, respectively, in the 10.7 and 25 pct Fe powders suggesting that the solid solution phase has transformed to  $\text{Al}_3\text{Fe}$  in the powder with 10.7 pct Fe and to  $\text{Al}_5\text{Fe}_2$  in the 25 pct Fe during shock consolidation. Transmission electron

micrographs of the consolidated specimens (**Fig.2.3**) confirmed the retention of 25-30nm grains in both the compositions after the shock consolidation. A summary of the results of MA in different compositions is shown in **Fig.2.4**.

### **2.4.3 Microstructural studies**

In all the five alloys investigated (Al-1, 4, 7.3, 10.7 and 25 pct Fe), a decrease in the particle size was observed with increasing milling time. **Fig.2.5** shows SEM micrographs of the Al-4 pct Fe powder in as-blended condition and after milling for 10h and 20h, indicating that the particle size decreases with increasing milling time. A similar situation was obtained in all the other compositions. At a high magnification (**Fig.2.6**) it can be seen that the observed particles are composite in nature and are made up of agglomerated nanometer-sized particles; the particles are less than 100nm in size in the Al-10.7 pct Fe powder MA up to 30h [21].

## 2.5 ALUMINIUM-IRON OXIDE SYSTEM



Where, M is a metal and A is either a metal or a non-metal, MO and AO are their corresponding oxides, and  $\Delta H$  is the heat generated by the reaction. Because of the large exothermic heat, reaction of this type generally be initiated locally and can become self-sustaining. This type of reactions are important in the synthesis of refractory ceramic and composite materials and in the preparation of ceramic coatings in metallic pipes. However, due to the very intensive reaction between liquid aluminium and  $Fe_2O_3$ , it is very difficult to study reaction mechanisms of the process. Moreover, due to this fast reaction process, it is extremely difficult to control the process for producing reaction product of controlled microstructure. The reaction rate was reduced either by reducing the contact area between aluminium and iron oxide or by controlling the heat treatment procedure [23].

### 2.5.1 Processing

Aldrich Chemical Co., UK has done this experiment to conclude about the reaction between Al melt and  $Fe_2O_3$ . Besides this they have also studied the reaction product by taking both (Al &  $Fe_2O_3$ ) in powder form. In the later part they mixed and sintered to get some pellets and placed them in a furnace at different temperature to study the reaction product. The first step was to investigate the interfacial reaction between liquid aluminium and sintered iron oxide [24]. The iron oxide ( $Fe_2O_3$ ) with average particle size of 5 mm was obtained from the Aldrich Chemical Co., UK. The iron oxide powder was ball milled for four hours with methanol as a suspension solvent. The dried powder was cold pressed into pellets for sintering. The pellets were sintered at 1100°C in air for 2 hours. The sintered iron oxide was placed into a crucible large enough to facilitate immersion of the iron oxide in aluminium. Liquid aluminium of commercial purity at 700°C was poured into the crucible containing the iron oxide. The crucible was then placed in a furnace at 1000°C for different periods of time. In the second step, they had taken aluminium powder with a purity of 99.1% and an average particle size of 20 mm and iron oxide ( $Fe_2O_3$ ) powder with a purity of 99.1% and a maximum particle size of 5 mm (Aldrich Chemical Co., UK) were mixed thoroughly by grinding using a mortar and pestle in a molar ratio of 2:1. The mixed powder was pressed into discs with a diameter of 10 mm and a thickness of 2 mm using a hydraulic press with a



pressure of 150 bar. A heating rate of 10°C/min was used and the experiment was carried out under argon atmosphere with a flow rate of 40 ml/min. Cold-pressed specimens were placed in a tube furnace at 960°C and 1060°C, respectively for 1 hour under constant flow of argon.

### 2.5.2 Characterization

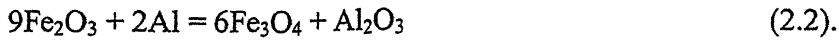
The cooled samples were sectioned for characterization of the microstructure of the Fe<sub>2</sub>O<sub>3</sub>/Al interface using electron microscopy. Microanalysis was carried out using a Jeol JXA840 Microprobe scanning electron microscope. The surface and the polished cross section of the reaction products were examined using scanning electron microscopy (SEM) coupled with energy dispersive spectroscopy. Then the reaction products were ground into powder and analyzed using X-ray diffraction [25].

The cross-section of the aluminium/Fe<sub>2</sub>O<sub>3</sub> interface produced from the reaction between liquid aluminum and sintered Fe<sub>2</sub>O<sub>3</sub> were studied at 1000°C (Fig 2.7). A reaction layer of about 600 nm consisting of an Al<sub>2</sub>O<sub>3</sub> and FeAl<sub>x</sub> composite (B) adjacent to the aluminum, and FeO<sub>x</sub> (D and E) was produced between the aluminum and the Fe<sub>2</sub>O<sub>3</sub>. The FeO<sub>x</sub> layer of grey colour shows at least two phases present, labeled as D and E. However, it is impossible to identify the phase composition due to difficulties in analyzing oxygen using EDX. To determine the reaction temperature, thermal analysis was carried out on the mixture of aluminum and iron oxide powder (Fig 2.8). One endothermic reaction peak at 660°C and two exothermic reaction peaks at about 960°C and 1060°C are shown in the spectra. The endothermic reaction is due to the melting of the aluminum powder and is the same for both the powder sample and the pressed sample [26].

The two exothermic reaction peaks indicate that the reactions between the aluminum and iron oxide were initiated at about 960°C and 1060°C respectively. However, the reaction temperature in the pressed specimen is slightly lower than that in the powder specimen. This is due to more contact between the Fe<sub>2</sub>O<sub>3</sub> and the Al in the pressed specimen than in the powder specimen, so that the reaction in the pressed specimen can be initiated more easily than that in the powder specimen [27].

Fig 2.4 shows the SEM images of the top surface of the pressed specimens produced at temperatures of 960°C and 1060°C. At 960°C, needle-like crystals were formed at the surface of the specimen (Fig 2.9.a). These were identified as aluminium using EDX. Such needle-like crystals are only present at the centre of the top surface of the cylindrical pellet,

not around the edges. This suggests that aluminium vapour was generated during the thermite process and deposited on the surface of the specimen when it cooled outside of the specimen. It was observed that the deposition of Al mainly occurred at the central area of the top surface of the specimen. This is because the reaction heat is more easily lost around the edges of the specimen [28]. A similar specimen was crushed into powder for XRD (Fig 2.10, top). The specimen mainly consists of Fe<sub>3</sub>O<sub>4</sub> and Al. The concentration of Al<sub>2</sub>O<sub>3</sub> is too low to be detected using XRD. The reaction would be



After reaction was initiated at the 1060°C, equiaxed crystals were found at the surface of the specimen (Fig 2.9b). The composition was identified using EDX as mainly Fe. In addition, the rod-like crystals were also formed at the surface and were identified as Fe and Al with ratio of 3:1. XRD of the top surface showed the presence of Fe<sub>2</sub>O<sub>3</sub> and Fe<sub>3</sub>O<sub>4</sub> (Fig 2.10, bottom). There was no Fe or Fe<sub>3</sub>Al peaks, which suggested that product at the top surface could be mainly iron oxide with much less of the Fe<sub>3</sub>Al phase. The temperature inside the specimen during the reaction process should be much higher than 1060°C. The high temperature inside the specimen induced the evaporation of Fe, oxygen and some unreacted Al, which then deposited at the surface of the specimen to produce an iron oxide layer and Fe<sub>3</sub>Al crystals. It was noted that there was no such formation at the bottom surface of the specimens produced both at 960°C and 1060°C [29].

XRD on a crushed sample of the specimen showed that there were Fe, Al<sub>2</sub>O<sub>3</sub> and FeAl<sub>2</sub>O<sub>4</sub> (Fig 2.10, middle). The chemical reactions would be

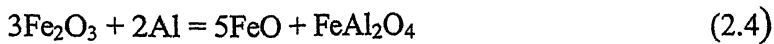


Fig 2.11 shows an SEM image of the cross section of the reaction zone between Fe<sub>2</sub>O<sub>3</sub> and Al produced at 960°C. The major bright area was identified as Fe<sub>3</sub>O<sub>4</sub> and the dark particle is aluminium. There was a reaction product surrounding the aluminium particles between the aluminium and iron oxide which is assumed to be Al<sub>2</sub>O<sub>3</sub>.

Fig 2.12 shows the SEM image of the cross-section of the specimen produced at 1060°C. The product shows a high porosity with different phases present. Using EDX, they have identified the phases of  $\text{Al}_2\text{O}_3$  and  $\text{FeAl}_2\text{O}_4$  and Fe, labelled as D, F, and B. It is interesting to note that the composition of the product at the top surface is different from that of the bulk. There is a layer 10 mm thick at the top surface which is mainly Fe or iron oxide (Fig 2.12a) and many needle shaped single crystals of Fe or its oxide appear to be deposited on the top surface (Fig 2.12b). This phenomenon could be a further indication suggesting that there are evaporation and precipitation of Fe on the top surface of the sample [30]. DTA results indicate that the reactions between liquid aluminium and  $\text{Fe}_2\text{O}_3$  were initiated at 960° and 1060°C. The reactions are very different at these two temperatures, therefore, different reaction heats were generated. According to the Gibbs energy of formation for reaction 2.2, the reaction heat will be 1036 KJ. Assuming 9 mole of  $\text{Fe}_2\text{O}_3$  and 18 mole of Al as reactants since the molar ratio of Al and  $\text{Fe}_2\text{O}_3$  was 2:1 as prepared in the experiments, the reaction products will be 6 mole  $\text{Fe}_3\text{O}_4$ , 1 mole of  $\text{Al}_2\text{O}_3$ , and 16 mole of Al, according to equation 2.2. The total heat capacity of these product will be 763 J/K [see Table 2.1]. If the total reaction heat is used for heating the reaction products, the temperature of the product will be 2317°C after the reaction. The boiling temperature of aluminium is 2520°C, which is very close to the calculated adiabatic temperature. The presence of aluminium at the top surface indicated that there was some evaporation of aluminium during the reaction. The evaporation of Al will also absorb significant heat. However, the undisturbed microstructure of the reaction products suggested that most of reaction product did not become liquid phase during the reaction, so there must have been some heat loss to environment, may be by evaporation and deposition of aluminium. The phase diagram of Fe-Al-O system at 1000°C [31] shows a three phase region of  $\text{Fe}_2\text{O}_3$ ,  $\text{Al}_2\text{O}_3$  and  $\text{Fe}_3\text{O}_4$ , which confirms the reaction 2.2 (Fig 2.13), although the presence of  $\text{Al}_2\text{O}_3$  could not be identified using XRD. The reactions initiated at 1060°C converted Al and  $\text{Fe}_2\text{O}_3$  completely into  $\text{Al}_2\text{O}_3$ , Fe, and  $\text{FeAl}_2\text{O}_4$ , according to the XRD analysis. These reaction products are more likely from the solidification of liquid phases based on the observation of the SEM images (Fig 2.12). This suggests that the reaction temperature in this specimen was considerably higher than that in the specimen produced at 960°C.

Moreover, there should be some FeO present in the product according to reaction 2.4. However, the XRD results showed that the main products are Fe,  $\text{Al}_2\text{O}_3$ ,  $\text{FeAl}_2\text{O}_4$  with no Al unreacted. Therefore, it is reasonable to assume there was some other reaction occurring as well, which could be the decomposition of  $\text{Fe}_2\text{O}_3$  at high temperature in an inert atmosphere. It indicates that the  $\text{Fe}_2\text{O}_3$  becomes liquid Fe-O phase at decreasing temperature as the oxygen partial pressure decreases. We believe that some  $\text{Fe}_2\text{O}_3$  decompose into oxygen and FeO during the reaction, so the FeO reacted with  $\text{Al}_2\text{O}_3$  to form  $\text{FeAl}_2\text{O}_4$  [32]. The reaction between the FeO and  $\text{Al}_2\text{O}_3$  is a fast reaction, so there was no FeO left. The undecomposed  $\text{Fe}_2\text{O}_3$  reacted with Al to form  $\text{Al}_2\text{O}_3$  and Fe. In summary, the increased reaction temperature and inert atmosphere leads to the decomposition of  $\text{Fe}_2\text{O}_3$  into FeO and oxygen which escapes from the specimen. The oxygen could react with evaporated Fe to form the iron oxide deposited on the top surface [33]. The presence of a thin layer of Fe or iron oxide layer further proves the decomposition of the  $\text{Fe}_2\text{O}_3$  into oxygen and FeO. Two stages of reaction were discovered in the thermite process of the  $\text{Fe}_2\text{O}_3$  -Al system. The first stage reaction was initiated at  $960^\circ\text{C}$ , producing  $\text{Fe}_3\text{O}_4$  and  $\text{Al}_2\text{O}_3$ . The second stage reaction was initiated at  $1060^\circ\text{C}$ , producing Fe,  $\text{FeAl}_2\text{O}_4$  and  $\text{Al}_2\text{O}_3$ . There was evaporation of Al during the reaction initiated at  $960^\circ\text{C}$ , and evaporation of Fe and oxygen during the reaction initiated at  $1060^\circ\text{C}$ . The high reaction temperature and inert atmosphere leads to decomposition of  $\text{Fe}_2\text{O}_3$ , therefore, inducing the formation of the  $\text{FeAl}_2\text{O}_4$  phase in the final product.

## 2.6 Reaction between molten aluminium and iron sample:

The process of aluminizing [34], permanent mould casting [35], master-alloy production [36] and solidification of iron containing aluminium alloys [37 and 38], bimetal formation, and welding and brazing [39 and 40], and more recently the fabrication of iron aluminide-based intermetallic matrix composites [41, 42 and 43], are principally dependent upon the interfacial reaction between the molten aluminium and solid iron. It would therefore be quite beneficial to have a thorough knowledge and understanding of the reaction products and kinetics to devise, design and control experiments to achieve products with the required characteristics in such diverse fields as mentioned above. The system is characterized with an iron-based solid solution and six non-stoichiometric intermetallic compounds of  $\text{Fe}_3\text{Al}$ ,  $\text{FeAl}$ ,  $\text{FeAl}_2$ ,  $\text{Fe}_2\text{Al}_3$ ,  $\text{Fe}_2\text{Al}_5$  and  $\text{FeAl}_3$ . Table 2.2, Table 2.3 and Table 2.4 gives the physical, thermodynamical and phase reactions for this phase diagram with special emphasis on the intermetallic phases, respectively [44].

Eggeler et al. [45, 46] studied the reactions between low alloyed steels and pure as well as iron-saturated aluminium melts. The purpose of this work is to examine the interaction between solid iron sample and liquid aluminium. They detected two intermetallic layers (the  $\text{Fe}_2\text{Al}_5$  phase adhering to the steel substrate by an irregular interface and the  $\text{FeAl}_3$  phase adhering to the solidified aluminium) with a growth showing negative deviations from the parabolic relationship after long reaction times. The interaction between solid iron and liquid aluminium is studied by immersion tests. At first, the intermetallic layers formed at the solid-liquid interface and their growth mechanisms are characterized. The  $\text{Fe}_2\text{Al}_5$  and  $\text{FeAl}_3$  phases are identified in the temperature range from 700 to 900°C, and their growth is found to be mainly controlled by a diffusion regime. Then, a theoretical approach of the phase growth based on the solutions of the diffusion equations is presented.

The formation and growth of intermetallic compound layers during dissimilar metal contact at high temperatures is a common phenomenon. Such behaviour in the solid state is often observed in diffusion bonding and in fiber-matrix reactions in composites [47, 48]. This occurs also when a liquid metal is used as terminal component, for example, in the case of hot-dip coating, liquid metal corrosion, composites prepared by liquid infiltration, soldering and brazing [49-52]. It is established that the growth of the intermediate phases can be

governed by chemical reactions at the interfaces (linear kinetics) and by interdiffusion of the reacting species through the different phases (parabolic kinetics). Description of the growth kinetics in multiphase binary couples can be found in many papers [53-57]. In near equilibrium conditions, the interfacial phases formed at a given temperature during contact are closely related to the phase diagram of the system. However, according to experimental observations, some equilibrium phases seem to be missing. This indicates that various effects have to be considered in growth mechanisms such as nucleation conditions at the beginning of the process, chemical reactions and low diffusivity in the missing phases. It is clear that the types of intermetallic layers formed and their thicknesses play an important part in obtaining materials with optimum performances. Thus, it is essential to understand the phase formation at the interfaces, the interface morphology and the growth mechanisms to provide guidelines for the prediction and control of interface reactions.

The Fe–Al system has been selected because of its technological applications. Previous studies were mainly concerned with steels and effort was often directed towards adherence. Their results showed kinetic discrepancies with those reported by Eremenko et al. [58]. More recently, Dybkov [59] studied the interaction of stainless steel with liquid aluminium by using the rotating disc method. The time dependence of the total thickness of both layers was described in terms of parabolic kinetics. With regard to earlier works dealing with the reaction between pure iron and pure liquid aluminium, Gebhardt and Obrowski [60] detected the  $\text{Fe}_2\text{Al}_5$  phase layer but they were unable to formulate unambiguously the growth kinetics whereas Heumann and Dittrich [61] identified the  $\text{Fe}_2\text{Al}_5$  phase as the major constituent of the layer and found a parabolic time dependence. In another investigation, Denner and Jones [62] reported that the thickness of the layer also obeyed a parabolic time relationship but the activation energy deduced from their work was higher than that obtained in previous studies. Reasons for this discrepancy were given in terms of simultaneous growth and spalling of the intermetallic layer for long dipping times. A tongue-like interface was also observed between the iron and the  $\text{Fe}_2\text{Al}_5$  phase as in the case of studies with low alloyed steels [63] but the  $\text{FeAl}_3$  phase was not detected. Therefore, the literature shows that the determination of the types of intermetallic layers and the knowledge of the growth kinetics are still incomplete and contradictory in the Fe–Al system. They have done the experiments with pure iron in contact with static and unsaturated molten aluminium, so that dissolution of iron could take

place simultaneously with the interlayer growth. The intermetallic layers formed at the solid-liquid interface at various temperatures and for different dipping times were identified. Their microstructures, their growths and probable growth mechanisms were determined. The experimental data were then used and discussed taking into account the theoretical aspects of the reactive diffusion.

### 2.6.1 Processing

Eggeler et al. [64] had studied the interaction between iron and liquid aluminium by immersion tests performed in isothermal conditions. Armco iron (99.78%) was used for this work, the surfaces of specimens ( $35 \times 5 \times 3 \text{ mm}^3$ ) were electrolytically polished. Aluminium (99.997%) was cleaned of its oxide film in 5% NaOH solution for 1 min before melting. The tests were carried out in the device presented in **Fig 2.14**. A small quantity of aluminium (10 g) was melted in a 15 mm internal diameter alumina crucible under vacuum ( $10^{-5}$  mbar). A tungsten wire surrounded by tantalum thermal shields was used for the heating of the crucible in order to achieve a good temperature homogeneity. The temperature was measured ( $\pm 1^\circ\text{C}$ ) using a thermocouple put in contact with the crucible. The iron sample was attached to a specimen holder fixed at the top of the vacuum chamber, its longer axis parallel to the crucible axis. When the aluminium reached the required temperature ( $T=700, 800$  and  $900^\circ\text{C}$ ), the sample was lowered for preheating above the surface of the melt during 20 min and then dipped into the static molten Al for a fixed time ( $t=30 \text{ s}$ – $45 \text{ min}$ ). The solid-liquid interaction was interrupted by switching off the heating system and cooling the crucible together with the melt and the sample under flowing gas (helium gas pre-cooled with liquid nitrogen).

### 2.6.2 Characterization

The Fe-Al couples were sectioned normal to the long axis of the solid sample (i.e. normal to the solid-liquid interface) and then mechanically polished (mirror finished). The bimetallic samples were examined by both optical and scanning electron microscopy. Composition of the phases and concentration profiles were obtained by electron microprobe. Identification of the phases was also verified by X-ray diffraction. Here, the samples were sectioned parallel to the solid-liquid interface. Then, the aluminium part was polished step by step to remove successively the various phases until the iron was reached. At different stages of the metal removal, X-ray diffraction patterns were made. For all experiments

carried out in the temperature range from 700 to 900°C, two phase layers were observed whatever the time of contact between solid Fe and molten Al. It is almost impossible to distinguish different phases within the interface layer and therefore the back-scattered electron (BSE) micrographs are presented in **Fig.2.15** to clearly show the formation of at least two phases at the interface layer. The EDS spectra for these phases are given in **Fig.2.16**, which may suggest that both phases are principally the same with slightly different iron and aluminium contents. The XRD spectra in **Fig.2.17** identify the phases as  $\text{Fe}_2\text{Al}_5$  and  $\text{FeAl}_3$  with  $\text{FeAl}_3$  being the minor phase. However, as can be seen from these spectra, increasing the exposure time of iron coupon within molten aluminium increases the number of  $\text{FeAl}_3$  reflections. In fact,  $\text{FeAl}_3$  was detected as small patches right from 90 s immersion time. In contrast to the interface morphology at  $\text{Fe}/\text{Fe}_2\text{Al}_5$ , the interface morphology at the  $\text{FeAl}_3/\text{Fe}_2\text{Al}_5$  and  $\text{FeAl}_3/\text{Al}$  is less irregular and closer to a near planar one as shown in **Fig.2.15**. Finally, if the BSE images are examined more closely, **Fig.2.15**, the formation of fine cracks are easily detectable within  $\text{FeAl}_3$  layer at  $\text{FeAl}_3/\text{Al}$  and also the detachment or breakage of this layer is noticeable at this region. Furthermore the darker phase,  $\text{FeAl}_3$ , has grown to form a solid layer of about 10–15  $\mu\text{m}$  at the interface. The aluminium region itself contains some needle-shaped intermetallic compounds, which may suggest that there is some mixing of iron within the molten aluminium.

**Fig 2.18.** shows a typical interfacial microstructure formed at 800°C. The electron microprobe analysis indicated that the phases were clearly identified to  $\text{Fe}_2\text{Al}_5$  (layer adjacent to iron) and  $\text{FeAl}_3$  (layer adjacent to aluminium). This was confirmed by the X-ray diffraction patterns which were consistently indexed assuming an orthorhombic structure for  $\text{Fe}_2\text{Al}_5$  ( $a=0.7675$  nm,  $b=0.6403$  nm,  $c=0.4203$  nm) and a monoclinic structure for  $\text{FeAl}_3$  ( $a=1.5489$  nm,  $b=0.8083$  nm,  $c=1.2476$  nm) [54]. The identified phases coincide with the Al-rich phases of the Fe–Al binary phase diagram (**Fig 2.19**). Moreover, the analyses showed that the values of the concentrations at the various phase boundaries corresponded to the equilibrium compositions dictated by the Fe–Al binary phase diagram.



The  $\text{Fe}_2\text{Al}_5$  layer is larger than the  $\text{FeAl}_3$  one. It can also be observed that the interface between Fe and  $\text{Fe}_2\text{Al}_5$  appears highly irregular with peaks orientated towards the iron [55]. This tongue-like morphology varies with time. Concerning the  $\text{Fe}_2\text{Al}_5/\text{FeAl}_3$  interface, irregularities observed for short contact times (30 s) decrease with a longer interaction (Fig 2.20). The boundary between  $\text{FeAl}_3$  and the liquid phase is also made of irregularities orientated towards the aluminium [56]. They were found to increase with time, forming thin platelets for longer times ( $t > 30$  min at  $800^\circ\text{C}$ ). Thin needles and platelets of  $\text{FeAl}_3$  were found to be uniformly dispersed in the solidified aluminium matrix. These elements are formed by eutectic reaction during the solidification of the melt containing some amount of dissolved iron. The platelets attached to the outer part of the  $\text{FeAl}_3$  layer and orientated towards the aluminium, mainly observed for long immersion times, were also formed during the cooling. The Fe enrichment was larger in the melt adjacent to the solid-liquid interface and thereby, the excess solute could precipitate in  $\text{FeAl}_3$  crystals during solidification. In fact, only a part of the  $\text{FeAl}_3$  layer is due to interdiffusion and thus the thick  $\text{FeAl}_3$  crystals due to solidification will be ignored for the study of the  $\text{FeAl}_3$  layer growth [57].

Fig 2.21 shows the thickness loss of the solid versus temperature for the two immersion times. The average thickness of each layer formed at  $T=800^\circ\text{C}$  is plotted as a function of the square root of time in Fig 2.22. The curve shows that the time and the thickness are related according to a parabolic law, suggesting that the layer growth is governed by diffusion [58]. However, the initial conditions ( $x=0$  at  $t=0$ ) are not satisfied, which indicates the existence of an initial short transient period of faster kinetics before the parabolic growth [59]. These results are in agreement with those presented in Fig 2.20. In fact, this indicates that the  $\text{Fe}_2\text{Al}_5$  and  $\text{FeAl}_3$  phase formation proceeds via an interface reaction control at the beginning of the process, their growth taking place without significant dissolution in the liquid [60]. At the end of this period when their thicknesses are large enough, the phases grow via a diffusion regime and their dissolution can be observed. However, the transient period being very short, the present experimental thickness measurements can only exhibit the parabolic stage of the process [62]. From a microstructural viewpoint, Fig 2.23 shows that the  $\text{Fe}_2\text{Al}_5$  phase has a polycrystalline structure in the part close to  $\text{FeAl}_3$ , while only a long grain seems to be present in the upper part adjacent to the iron [63]. Moreover, no relationship is observed between the grains of the

iron substrate and the  $\text{Fe}_2\text{Al}_5$  phase. In fact, this phase seems to cut the iron grains either transgranularly or intergranularly [64].

The intermetallic layers formed between solid iron and liquid aluminium have been characterized. Two phases,  $\text{Fe}_2\text{Al}_5$  and  $\text{FeAl}_3$ , have been identified in the temperature range from 700 to 900°C. It is shown that their growth is controlled by interdiffusion after a non-parabolic initial transient period [65-76]. The interface between iron and  $\text{Fe}_2\text{Al}_5$  has been found to be highly irregular. A theoretical approach of the phase growth based on the solutions of diffusion equations has been presented and a rather good description of the experimental data has been obtained through this numerical method. In particular, the absence of  $\text{FeAl}$  and  $\text{FeAl}_2$  phases can be attributed to their very low growth rates. The calculated values for the growth rate of the two intermediate phases,  $\text{Fe}_2\text{Al}_5$  and  $\text{FeAl}_3$ , are consistent with the experimental observations.

## References

1. B.S.S. Daniel, V.S.R. Murthy and G.S. Murthy, "Metal-ceramic composites via in-situ methods," *J. Mater. Process. Tech.*, Vol.68, 1997, 132-155.
2. Z.A. Munir, "Synthesis of high temperature materials by self-propagating combustion methods," *Am. Ceram. Soc. Bull.*, Vol.67, 1988, 342-349.
3. J.J. Moore, H.J. Feng, "Combustion synthesis of advanced materials: classification, application and modeling," *Prog. Mater. Sci.*, Vol.39, 1995, 275-316.
4. S.C. Tjong and Z.Y. Ma, "Microstructural and mechanical characteristics of in-situ metal matrix composites," *Mater. Sci. and Engg.*, Vol.29, 2000, 49-113.
5. R. Pampuch, "Some fundamental versus practical aspects of self-propagating high temperature synthesis," *Solid State Ionics*, Vol.101-103, 1997, 897-907.
6. F.H. Froes, "Structural intermetallics," *JOM*, Vol.41, 1989, 6-7.
7. R.L. Fleischer and A.I. Taub, "Selecting high-temperature structural intermetallic compounds: the materials science approach," *JOM*, Vol.41, 1989, 8-11.
8. D.L. Anton, D.M. Shah, D.N. Dulh and F.H. Giamei, "Selecting high-temperature structural intermetallic compounds: the engineering approach," *JOM*, Vol.41, 1989, 12-17.
9. C. Bassai, J.A. Peters and J. Wittenauer, "Processing of titanium aluminide foils," *JOM*, Vol.41, 1989, 18-20.
10. Y.W. Kim, "Ordered intermetallic alloys," Part III: gamma titanium aluminides, *JOM*, Vol.46, 1994, 30-39.
11. A.G. Merzhanov in "Combustion and plasma synthesis of high-temperature materials," (Eds.) Z.A. Munir and J.B. Holt, VCH publishers, Weinheim, Newyork, 1990, P1.
12. Z.A. Munir and U. Anselmi-tamburini, *Mater. Sci. Reports*, Vol.3, 1989, 277-365.
13. J.W. McCauley, "Historical and technical perspective on SHS," *Ceram. Engg. Sci. Proc.*, Vol.11, 1990, 1137-1188.
14. S. Schicker, D.E. Garcia, J. Bruhn, R. Janssen and N. Claussen, "Reaction synthesized  $\text{Al}_2\text{O}_3$ -based intermetallic composites," *Acta. Mater.*, Vol.46, 1998, 2485-2492.

15. S.P. Gaus, M.P. Harmer, H.M. Chan, H.S. Ceram, N. Claussen, "Alumina-aluminide alloys (3A) technology: I, model development, J. Am. Ceram. Soc., Vol.83, 2000, 1599-1605.
16. J. Bruhn, S. Scicker, D.E. Garcia, I. Gorlov, R. Janssen and N. Claussen, "Novel reaction-based processing of co-continuous ceramic-metal composites," Key. Engg. Mater, Vol.127-131, 1997, 73-80.
17. N. Claussen, J. Bruhn, D.E. Garcia, R. Janssen and S. Schicker, "Intermetallics reinforced alumina," Ceram. Engg. Sci. Proc., Vol.15, 1994, 395-399.
18. S. Schicker, D.E. Garcia, J. Bruhn, R. Janssen and N. Claussen, "Reaction processing of  $\text{Al}_2\text{O}_3$  composites containing iron and iron aluminides," J. Am. Ceram. Soc., Vol.80, 1997, 2294-2300.
19. B.S. Murthy, and S. Ranganathan, "Novel materials synthesis by mechanical alloying/milling," Inter. Mater. Rev., Vol.43, 1998, 101-141.
20. C. Suryanarayana, "Mechanical alloying and milling," Prog. Mater. Sci., Vol.46, 2001, 1-184.
21. D.K. Mukhopadhyay, "Structural Evolution in Mechanically Alloyed Al-Fe Powder Mixtures," TMS Outstanding Student Paper Contest Winner, 1994.
22. Y. Dong, W.H. Wang, L. Lin, K.Q. Xiao, S.H. Tong and Y.Z. He: Mater Sci. & Engg., Vol.A134, 1991, 867.
23. J. Mei, R.D. Haldearn and P. Xiao, "Mechanisms of the aluminium-iron oxide thermite reaction," Scripta Materialia, Vol.41, 1999, 541-548.
24. Z. A. Munir, Metall. Trans. A. Vol.23A, 1992, 7-13.
25. O. Odawara and J. Ikeuchi, J. Am. Ceram. Soc. Vol.69, 1986, 85.
26. A. Varma and J. P. Lebrat, Chem. Eng. Sci. Vol.47, 1992, 2179.
27. E. A. Brandes, Smithells Metal Reference Handbook, Butterworth-Heinemann, Oxford (1992).
28. D. R. Lide, CRC Handbook of Chemistry and Physics Reference Data, CRC Press, London (1998).
29. Y. M. Chiang, D. Birnie, and W. D. Kingery, Physical Ceramics, John Wiley & Sons, New York (1997).

30. E. M. Levin, Phase Diagrams for Ceramists, American Ceramic Society, Columbus, OH (1964).
31. P.C. Maity, P.N. Chakraborty and S.C. Panigrahi, "Preparation of Al-Al<sub>2</sub>O<sub>3</sub> in-situ composites by addition of Fe<sub>2</sub>O<sub>3</sub> particles to pure Al melt," Journal of Material Science Letters, Vol.16, Issue 14, 1997, 1224-1226.
32. R. Schmid-Fetzer: Principal Reviewer of "Ternary Alloys" Vol.2e; 8.
33. Journal of Alloys and Compounds, Volume 337, Issues 1-2, 2 May 2002, Pages 289-295, by Christian Noel C. Luciano, Koh-ichi Udoh, Masaharu Nakagawa, Shigeki Matsuya and Michio Ohta.
34. A. Bahadur , "Aluminum coating for steel," Mater. Manuf. Process. Vol.12, 1996, 225-232.
35. Z.W. Chen and M.Z. Jahedi *Mater. Des.* Vol.20, 1999, 303.
36. A. Shafyei, R.I.L. Guthrie, Alloying of liquid aluminum, in: Light Metals, Proceedings of the 125th TMS Annual Meeting, February 4-8, 1996, Anaheim, CA, TMS Publication, 1996, 1017.
37. M.R. Ghomashchi, Intermetallic Compounds in an Al-Si Alloy Used in High Pressure Die Casting, *Z. Metallkd.*, Band 78, Heft 11, 1987, 784.
38. M.R. Ghomashchi , "Die filling and solidification of Al-Si alloys in high pressure die casting,". *Scand. J. Met.* Vol.22, 1993, 61.
39. V.L. Najdek, G.D. Kostenko, Theory and practice of processes for producing bimetal (two-layer) castings based on iron alloys, *Liteinoe Proizvodstvo*, No. 5, P 9 0024-449X LIPRAX Mezhdunarodnaya Kniga, Moscow, Russia, May 1999.
40. V.I. Dybkov , Interaction of 18Cr-10Ni stainless steel with liquid aluminum. *J. Mater. Sci.* Vol.25, 1990, 3615.
41. K. Yoshimi and S. Hanada *JOM* 49 Vol.8, 1997, P 46.
42. R. Subramaian and J.H. Schneibel , Processing of iron-aluminide composite containing carbides or borides. *JOM* 49 Vol.8, 1997, P 50.
43. B.H. Rabin and R.N. Wright , Synthesis of iron aluminide from elemental powder, reaction mechanism and desification behaviour. *Metall. Trans. A* 22, 1991, P 277.
44. Metals Handbook, Vol.63, 10th Edition, ASM International, 1992.

45. A. Bahadur, Aluminium coating for steel, *Mater. Manuf. Process.* Vol.12, 1996, 225-232.
46. H.R. Shahverdi, M.R. Ghomashchi, S. Shabestari, *J. Mater. Sci.* 2001-2002, 1061-1066.
47. A.J. Hickel and R.W. Heckel. *Met. Trans. A* 6A (1975), P 431.
48. R.B. Bhagat. *Composites* Vol.95 (1988), P 393.
49. A.J. Stavros, in: J.R. Davis (Ed.), *Metals Handbook, Corrosion*, vol. 13, 9th edn., ASM, International, Materials Park, OH, 1987, P 432.
50. C. Bagnell, W.F. Brehm, in: J.R. Davis (Ed.), *Metals Handbook, Corrosion*, Vol.13, 9<sup>th</sup> edn. ASM, International, Materials Park, OH, 1987, P 91.
51. H.R. Shahverdi, M.R. Ghomashchi, S. Shabestari and J. Hejazi, "Microstructural analysis of interfacial reaction between molten aluminium and solid iron," *J. Mater. Processing Technology*, 2002, Vol.124, 345-352.
52. T. Ishida. "Processing of iron aluminide composite," *J. Mater. Sci.* Vol.21 (1986), p. 1171.
53. G.V. Kidson. "Aluminium diffusion coating on medium carbon steel," *J. Mater. Sci.* Vol.31 (1961), P 21.
54. C. Wagner. *Acta Met.* Vol.17 (1969), P 99.
55. F.M. D'Heurle. *Mater. Sci. Forum* 1 (1994), P 155.
56. V.I. Dybkov. "The effect of dissolution on the growth of the  $\text{Fe}_2\text{Al}_5$  interlayer in the solid iron-liquid aluminium system," *J. Mater. Sci.* Vol.21 (1986), P 3078.
57. J.J. Van Loo. *Prog. Solid State Chem.* Vol.20 (1990), P 47.
58. V.N. Yeremenko, Ya.V. Natanzon and V.I. Dybkov. *J. Mater. Sci.* Vol.16 (1981), P 1748.
59. V.I. Dybkov. "Interaction of 18Cr-10Ni stainless steel with liquid aluminium," *J. Mater. Sci.* Vol.25 (1990), P 3615.
60. E. Gebhardt and W. Obrowski. "Reactive infiltration synthesis of iron aluminides," *J. Mater. Sci.* Vol.4 (1953), P 154.
61. T. Heumann, O.N. Mohanty and S. Dittrich. "Structural studies of hot dip aluminized coating on mild steel," *Met. Trans.* 50 10 (1959), P 617.

62. S.G. Denner and R.D. Jones "Metallurgy of continuous hot dip aluminizing," Int. Mat. Rev. Vol.39 (1994), P 191.
63. W.B. Pearson, in: P. Villars, L.D. Calvert (Eds.), Handbook of crystallographic data for intermetallic phases, ASM, Metals Park, OH, 1985.
64. U.R. Kattner, in: T.B. Massalski (Ed.), Binary alloy phase diagrams, ASM International, Materials Park, OH, 1990, P 147.
65. C.A. Handwerker, J.W. Cahn and J.R. Manning. Mater. Sci. Eng. A Vol.126 (1990), P 173.
66. W. Jost, Diffusion in Solids, Liquids, Gases, Academic Press, New York, 1952.
67. J. Philibert, Diffusion et transport dans les solides, Editions de Physique, les Ulis, France, 1985.
68. K. Bouché, Etude thermocinétique de la dissolution de métaux solides (fer et nickel) dans l'aluminium liquide, Thesis, University of Provence, Marseille, France, 1995.
69. A. Coulet, K. Bouché, F. Marinelli, F. Barbier, J. Appl. Phys., Vol.82 (1997) P 6001.
70. H.S. Carslaw, J.C. Jaeger, Conduction of Heat in Solids, 2nd edn., Oxford University Press, Oxford, 1959, P 50.
71. L.N. Larikov, V.V. Geichenko, V.M. Fal'chenko, Diffusion processes in ordered alloys, Naukova Dumka Pub, Kiev, 1975, National Bur. Stand. New Delhi, 1981.
72. H. Bakker, Landolt-Börnstein, New Series, III/26, Springer Verlag, Berlin, 1990, P 221.
73. R. Drewett. Corrosion Sci. Vol.9 (1969), P 823.
74. R.K. Bamsla and L.L. Seigle. Met. Trans. A 20A (1989), P 2561.
75. H.R. Shahverdi, M.R. Ghomashchi, S. Shabestari, J. Hejazi, Kinetics of interfacial reaction in liquid aluminium-solid iron, J. Mater. Sci. 2001-2002, 1061-1066.
76. Bulletin of Binary Phase Diagrams, ASM International, 1994.

## CHAPTER 3

### EXPERIMENTAL PROCEDURE

---

#### 3.1 Introduction

In this study, a large number of composites have been produced using “liquid metallurgy route”. These composites can be broadly classified into two types (i) Particulate composites with dispersions of  $\text{Al}_2\text{O}_3$  or SiC in Al and (ii) Al/ Alumina/ Iron aluminide composites using “In-situ” reactions. Pure Al metal castings are also made for comparison purpose. The experimental part of the thesis includes preparation of various composites, their characterization and assessment of mechanical properties.

#### 3.2 Raw materials

A near eutectic Al-Si alloy was used for preparation of all the composites.  $\text{Fe}_2\text{O}_3$ ,  $\text{Al}_2\text{O}_3$  and SiC reinforcements of 35-65 mesh size (425  $\mu\text{m}$  to 224  $\mu\text{m}$  particle size) were added to the melt. Pure Armco iron (purity of 99.8%) was added in the form of small cubes ( $25 \times 15 \times 2 \text{ mm}^3$ ). The iron pieces were cleaned by grinding and polishing with a coarse emery paper. Prior to melting all the Al pieces were cleaned using soap solution followed by water and acetone. After cleaning, the pieces were thoroughly dried with hot-air before loading in to the furnace.

#### 3.3 Melting and Composite preparation

##### 3.3.1 Pure Al melts

Aluminium pieces were accurately weighed and placed in a alumina crucible. The crucible was kept in a raising hearth furnace (Bysakh & Co, Calcutta) and the



temperature was raised to 800 °C/1100 °C (with a heating rate of 5 °C /min) and the melt was held for 1hr. When the melt had reached appropriate temperature, the melt was stirred intermittently using a graphite rod. During melting the furnace temperature was monitored using a Chromel-Alumel thermocouple. Manual stirring was done with a graphite rod, the melt was stirred 5 or 10 times with 30 Sec duration. The time gap chosen between successive stirring is around 10 min when it was stirred 5 times on the other hand, when the melt was stirred 10 times, the gap was around 5 min. subsequently cooling was done in air and then the weight of the metal was taken. The difference in the initial weight and final weight in each melt is taken to monitor the loss/gain by evaporation/oxidation (Table 3.1).

### **3.3.2 Melts with pure Fe additions**

In case of pure iron addition, iron piece was dipped in the melt by hanging with Tungsten wire. The melt was left in the furnace for 1hr for thorough chemical reaction between iron and liquid Al. The melt was stirred with a graphite rod for 5 or 10 times with duration of 30 sec. At regular intervals, the iron piece was brought down to compensate the dissolved portion. Finally, the melt was cooled in air by removing the iron piece. Initial weight and final weight were monitored during each experiment (Table 3.2). The above experiment was done at two temperatures, 800 °C and 1100 °C.

### **3.3.3 Melts with iron oxide addition**

In this case, varying amounts 2, 5 and 10 Wt. % of Fe<sub>2</sub>O<sub>3</sub> were added to the Al melts maintained at different temperatures (800 °C and 1100 °C). The Fe<sub>2</sub>O<sub>3</sub> powders were preheated to 150 °C for 1hr before adding to the Al melt. Stirring was done at intermediate periods and the weight of metal, slag and remaining unreacted powder were taken after each experiment (Table 3.3).

### **3.3.4 Melts with Al<sub>2</sub>O<sub>3</sub> or SiC additions**

The procedure in the earlier section was repeated and the melts with dispersion of Al<sub>2</sub>O<sub>3</sub> or SiC were prepared with frequent stirring of the melt. Here the Wt. % of both reinforcement and the temperature (2% and 1100 °C respectively) were kept constant.

### **3.4 Preparation of tensile test coupons**

After addition of reinforcements, the melts were cast in the form of tensile test coupons. The die for above purpose is a mild steel plate having a cavity of tensile test specimen shape. Thin plate is supported with 15mm thick base plate. The dimensions of dies are shown in Fig 3.1. The specimens formed are of rectangular and circular cross sections. Before pouring molten metal in to the die cavity, the die was preheated to 600 °C to minimize the casting defects. An asbestos insulation was also provided around the small cross sectional area to have controlled solidification. But for circular cross section specimen, the melt was sucked into the mould cavity i.e a long alumina tube of 12mm diameter was dipped in to the melt and sucked the molten metal in the same way as ink is sucked by a dropper. Then machining was done to the middle portion to make a specimen of perfect circular cross section. The details of these specimens are given in Table 3.4 – 3.7.

## **3.5 Characterization Techniques**

### **3.5.1 X-Ray Diffraction Analysis**

X-Ray diffraction pattern for the samples were recorded by an X-ray diffractometer (RICH SIEFERT ISO DEBYE FLEX 2002, GERMANY) using Cu-K<sub>α</sub> radiation ( $\lambda = 1.54056 \text{ \AA}$ ). The diffraction patterns were recorded at a scanning speed of  $3^\circ \text{ min}^{-1}$  at room temperature. Specimens cooled from the reaction temperature were

sectioned perpendicular to the tensile axis and X-ray diffraction data were collected to determine the phases present.

### **3.5.2 Optical Microscopy**

Samples from different failed tensile samples were sectioned with a diamond cutoff wheel, mounted and diamond polished according to standard polishing techniques. Polishing of samples were done by grinding using a series of emery papers 1/0, 2/0, 3/0, 4/0. To remove fine scratches polishing was done with fine alumina. The final polishing was done with one-micron diamond, followed by 0.05-micron alumina. An optical microscope (Lietz) was used for microstructural examination of phases and phase distribution.

## **3.6 Mechanical Testing**

### **3.6.1 Tensile Test**

An UTM ( Universal Testing Machine) was used for carrying out all the tensile tests. Samples taken after casting were machined to improve the dimension and the surface finish. Before subjecting them to tensile test, cross sectional reading and gage length were noted with the help of a slide caliper. Load vs elongation curves were obtained after each test.

### **3.6.2 Hardness Test**

The Rockwell hardness test method consists of indenting the test material with a diamond cone or hardened steel ball indenter. Rockwell hardness values are expressed as a combination of a hardness number and a scale symbol representing the indenter and the minor and major loads.

## CHAPTER 4

### RESULTS AND DISCUSSION

---

#### 4.1 Introduction

Microstructure and mechanical properties of Al matrix in-situ particle composites produced with different proportion of  $\text{Al/Fe}_x\text{Al}_y/\text{Al}_2\text{O}_3$  were compared with those of conventional particle reinforced composites ( $\text{Al/Al}_2\text{O}_3$ ,  $\text{Al/SiC}$ ) and near eutectic Al-Si base alloy. Experiments were done at  $800^\circ\text{C}$  and  $1100^\circ\text{C}$  with a view to produce  $\text{Fe}_x\text{Al}_y$  intermetallic and  $\text{Al}_2\text{O}_3$  composites in-situ by melting route. Characterization of these composites involved XRD, optical microscopy, tensile test and hardness test. These results are discussed in the following sections.

#### 4.2 Microstructure and mechanical properties of Al-Si alloy at different temperatures

In order to understand the changes in microstructure and mechanical properties of base alloy, separate experiments were carried on Al-Si melts [Table 3.1]. Experiments were done at  $800^\circ\text{C}$ ,  $1000^\circ\text{C}$  and  $1100^\circ\text{C}$  with intermittent stirring. In the present case, numbers of stirrings used were 5 and 10. For higher number of stirrings, weight gain is about 1.5 times that of the weight gain observed at lower number of stirrings. This weight gain is attributed to the formation of  $\text{Al}_2\text{O}_3$ .

No definite correlation between weight gain with temperature was noticed during experiments [Table 3.1]. From this data, it appears that the effect of temperature on Al-Si alloy is marginal. It resulted in very mild oxidation of the melt. However, the effect of temperature is almost negligible. This could also attributed to presence of Si.

Optical micrographs of pure Al-Si alloy are shown in **Fig. 4.2**. At 800°C the microstructure shows larger Si particulates (as needle and also in the form of cuboids) where as at 1100°C, the particles are much finer and dispersed uniformly throughout the microstructure.

X-ray diffraction patterns show an intense  $\text{Al}_2\text{O}_3$  peak at 1100°C (**Fig. 4.1**) indicating more melt oxidation at higher temperature.

The mechanical properties assured from the cast Al-Si tensile samples at different temperatures are shown in **Table 4.1**. The tensile strength varies between 105 MPa and 117 MPa at 800°C and 1100°C respectively. Similarly, hardness values also show  $22.6 \pm 6.2$  and  $26.1 \pm 5.2$  at 800°C and 1100°C respectively. There is a scatter in the data. This is attributed to casting defect or inhomogeneous distribution of Si particles and morphology and formation of oxide particles at higher temperature (i.e., 1100°C). The wettability of Al on  $\text{Al}_2\text{O}_3$  is better because the contact angle decreases as the temperature increases. For this reason experiments are carried out and compared at two different temperatures i.e., 800°C and 1100°C.

### **4.3 Microstructure and mechanical properties of Al-Si-Fe at different temperatures**

Pure Fe was added into Al-Si melt to understand the changes in the microstructure and mechanical properties of  $\text{Al}_2\text{O}_3/\text{Fe}_x\text{Al}_y\text{-Al}$  in-situ composites. Experiments were done at 800°C and 1100°C with intermittent stirring [**Table 3.2**]. At a constant stirring condition, the weight gain (Al) and weight loss (Fe) was found to be more at higher temperature (i.e., 1100°C). As shown in **Table 3.2** the weight gain (Al) at 1100°C is about 3 times of the weight gain observed at 800°C and the weight loss (Fe) at 1100°C is about 4 times the weight loss at 800°C. This weight gain is attributed to the formation of  $\text{Al}_2\text{O}_3$  and  $\text{FeAl}_3$  while the weight loss of Fe is due to dissolution of Fe into Al-Si melt. Weight gain (and dissolution of Fe) observed more at 1100°C is because the formations of  $\text{Al}_2\text{O}_3$  and  $\text{Fe}_x\text{Al}_y$  into the Al-Si melt both are favourable at higher temperature. Or

may be noted from the Al-Fe phase diagram that solubility of Fe in Al is about 29% and 4% at 1100°C and 800°C respectively.

Optical micrographs of samples are shown in **Fig. 4.4**. At 800°C, the microstructure shows larger Si particulates (as needles and also in the form of cuboids) and fine  $\text{Al}_2\text{O}_3$  particles, where as at 1100°C the Si particles are much finer.  $\text{Al}_2\text{O}_3$  particles are not uniformly distributed, rather that are found to be segregated. This may be due to settlement of the particles. No intermetallic phase ( $\text{FeAl}_3$ ) was seen in any microstructure. In fact,  $\text{FeAl}_3$  appears as small patches, as reaction proceeds. Later  $\text{FeAl}_3$  patches join together to form a continuous layer and even after 1hr, its thickness does not exceed more than 10 $\mu\text{m}$  and could easily be missed or ignored. During microstructural analysis, more number of finer  $\text{Al}_2\text{O}_3$  and Si particulates are observed at higher temperature (1100°C) than that at lower temperature (800°C). The reason may be due to more homogenization and fragmentation of particles at higher temperature.

X-ray diffraction patterns show an intense  $\text{Al}_2\text{O}_3$  peak at 1100°C (**Fig. 4.3**). Appearance of intermetallic ( $\text{FeAl}_3$ ) was found as is evident from the XRD plot [**Fig. 4.3**] at 1100°C, which is not found at 800°C. It is because the solid solubility of Fe in Al is more at 1100°C (about 29%).

The mechanical properties assured from the cast  $\text{Al}_2\text{O}_3/\text{Fe}_x\text{Al}_y\text{-Al}$  tensile samples at different temperature are shown in **Table 4.2**. The tensile strength varies between 101 MPa and 215 MPa at 800°C and 1100°C respectively. Similarly, hardness values also show  $31.7 \pm 4.8$  and  $39.6 \pm 5.6$  at 800°C and 1100°C respectively. The above result may be due to the formation of  $\text{Al}_2\text{O}_3$  particles and more wettability of Al on  $\text{Al}_2\text{O}_3$  at 1100°C. The iron aluminide phase that is formed (as per phase diagram) in these reaction found to be  $\text{FeAl}_3$ .

#### 4.4 Microstructure and mechanical properties of Al-Si-Fe<sub>2</sub>O<sub>3</sub> at different temperatures

As mentioned in the literature review, the reaction between Fe<sub>2</sub>O<sub>3</sub> and Al is exothermic (1036 KJ) and a sharp temperature rise is expected during the reaction. In addition, the reaction gives two reaction products (Al+Fe<sub>2</sub>O<sub>3</sub>→Fe<sub>x</sub>Al<sub>y</sub>+ Al<sub>2</sub>O<sub>3</sub> with excess Al) which are expected to strengthen the matrix. In order to understand the changes in microstructure and mechanical properties of these in-situ composites, separate experiments were carried on by adding Fe<sub>2</sub>O<sub>3</sub> particles into the Al-Si melt. Experiments were done with 2%, 5% and 10% Fe<sub>2</sub>O<sub>3</sub> at 800°C and 1100°C with intermittent stirring [Table 3.3]. For higher temperature, the weight loss of metal was found to be 10 times of the weight loss observed at lower temperature. This is due to sharp temperature rise during exothermic reaction. more weight loss at 1100°C is attributed to the evaporation of Al at higher temperature. As the exothermic reaction between Al and Fe<sub>2</sub>O<sub>3</sub> at 1100°C leads to the temperature about 2660°C which is more than the boiling point of Al.

Optical micrographs of samples are shown in Fig. 4.6. At 800°C the microstructure shows larger Si particulates (as needle and also in the form of cuboids) also with some Al<sub>2</sub>O<sub>3</sub> particles where as at 1100°C, the particles are much finer. Dispersion of Al<sub>2</sub>O<sub>3</sub> are uniform at 1100°C where as the dispersion of Al<sub>2</sub>O<sub>3</sub> particles are found to be segregated at 800°C. The reason may be due to improper stirring as the melt is more sluggish at lower temperature. But in case of 2% Fe<sub>2</sub>O<sub>3</sub> micrographs show some lesser Si and Al<sub>2</sub>O<sub>3</sub> particles than that of 5% Fe<sub>2</sub>O<sub>3</sub> at same temperature [Fig. 4.8]. The reason may be small addition of Fe<sub>2</sub>O<sub>3</sub>.

X-ray diffraction patterns show an intense Al<sub>2</sub>O<sub>3</sub> peak at 1100°C (Fig. 4.5). Appearance of intermetallic (FeAl<sub>3</sub>) was found as is evident from the XRD plot (Fig. 4.5) at 1100°C, which is not evident at 800°C. It is because the solid solubility of Fe in Al is more at 1100°C (about 29%). Comparing XRD plots of 2% Fe<sub>2</sub>O<sub>3</sub> and 5% Fe<sub>2</sub>O<sub>3</sub> at 1100°C , some intense and more no of peaks were obtained in the case of 5% Fe<sub>2</sub>O<sub>3</sub>.

Reason may be due to the better reaction and more uniform distribution of finer  $\text{Al}_2\text{O}_3$  (Fig. 4.13).

The mechanical properties assured from the cast  $\text{Al}_2\text{O}_3/\text{Fe}_x\text{Al}_y\text{-Al}$  tensile samples at different temperature are shown in Table 4.3. The tensile strength varies between 98 MPa and 271 MPa at  $800^\circ\text{C}$  and  $1100^\circ\text{C}$  respectively. Similarly, hardness values also show  $38.9 \pm 3.3$  and  $61.9 \pm 7.1$  at  $800^\circ\text{C}$  and  $1100^\circ\text{C}$  respectively. The above result may be due to the formation of more finer  $\text{Al}_2\text{O}_3$  particles and more wettability of Al on  $\text{Al}_2\text{O}_3$  at  $1100^\circ\text{C}$ . Compared with 2%  $\text{Fe}_2\text{O}_3$  at  $1100^\circ\text{C}$  and 5%  $\text{Fe}_2\text{O}_3$  at  $1100^\circ\text{C}$  both hardness and tensile strength values of 2%  $\text{Fe}_2\text{O}_3$  found to be less [Fig. 4.15 and Fig. 4.17].

#### **4.5 Microstructure and mechanical properties of particulate (Al/ $\text{Al}_2\text{O}_3$ , Al/SiC) composites**

To compare the results of in-situ composites some particulate composites were produced by adding 2%  $\text{Al}_2\text{O}_3$  and 2% SiC into the Al-Si melt. No SiC were found in both micrographs as well as in the XRD patterns (Fig. 4.9 and Fig. 4.10). Reason may be due to small addition of SiC particles at such high temperature. But in case of 2%  $\text{Al}_2\text{O}_3$  addition, some finer  $\text{Al}_2\text{O}_3$  and Si (both needle and cuboids) were found in the micrographs (Fig. 12). XRD pattern also shows an intense peak of  $\text{Al}_2\text{O}_3$  (Fig. 4.11) which is due to the uniform dispersion of  $\text{Al}_2\text{O}_3$ . As at higher temperature the wettability of Al on  $\text{Al}_2\text{O}_3$  particles is more.

The mechanical properties are shown in the Table 4.4 and Table 4.5. The tensile strength varies between 111 MPa and 151 MPa at  $1100^\circ\text{C}$  for 2%  $\text{Al}_2\text{O}_3$  and 2% SiC respectively. Similarly, hardness values also show  $36.9 \pm 6.3$  and  $44.2 \pm 3.9$  at  $800^\circ\text{C}$  and  $1100^\circ\text{C}$  for 2%  $\text{Al}_2\text{O}_3$  and 2% SiC respectively.



## 4.6 Comparison of in-situ composites with Al/Al<sub>2</sub>O<sub>3</sub> and Al/SiC composites

The mechanical properties of in-situ (Al<sub>2</sub>O<sub>3</sub>/ Fe<sub>x</sub>Al<sub>y</sub>-Al) composites are found to be better than that of the conventional particulate (Al/ Al<sub>2</sub>O<sub>3</sub> and Al/SiC) composite (Fig. 4.14 and Fig. 4.16). The hardness and strength of in-situ composite is almost 1.5 and 2 times than that of conventional particulate composite. XRD peaks of in-situ composites are more intense with comparison to particulate composites. From the microscopical point of view more Al<sub>2</sub>O<sub>3</sub> and Si particles formation were noted in case of in-situ composites. This may be due to the better fragmentation of particles at higher temperature of the melt as the reaction in in-situ process is exothermic in nature. Also, wettability of Al on Al<sub>2</sub>O<sub>3</sub> is increased because the temperature of the melt rises which decreases the contact angle between Al and Al<sub>2</sub>O<sub>3</sub>.

# CHAPTER 5

## CONCLUSIONS

---

The following conclusions were made from the present research work:

- 1 Al-Si base cast metal matrix composites ( $\text{Fe}_x\text{Al}_y + \text{Al}_2\text{O}_3 + \text{Al-Si}$ ) are prepared using well known exothermic, self sustaining reaction i.e.  $\text{Fe}_2\text{O}_3 + \text{Al} \rightarrow \text{FeAl}_3 + \text{Al}_2\text{O}_3$ . This reaction is very useful to prepare Al composites with  $\text{Fe}_x\text{Al}_y$  and  $\text{Al}_2\text{O}_3$  particulate reinforcements. The reaction with metal phase (Fe) were also studied. The Al reaction with Fe leads to formation only  $\text{Fe}_x\text{Al}_y$  phase. No oxide is found
2. The composites are prepared at two different temperatures viz., 800 °C and 1100 °C. At lower temperature, the exothermic reaction was sluggish while at 1100 °C the reaction was rapid. The reactions at higher temperature are preferable because wettability between Al and  $\text{Al}_2\text{O}_3$  is also improved.
- 3 A weight loss was marked during composite preparation. That is due to the evaporation of Al at higher temperature. (Temperature rises to 2660°C due to exothermic reaction, which is for exceeding the boiling point of Al)
4. The mechanical properties of in-situ reacted composites are compared with those of particulate (Al-Si/ $\text{Al}_2\text{O}_3$ /SiC) composites. In-situ composites prepared at 1100°C show better mechanical properties than that of composites at 800°C. Cast Al-Si, Al-Si-Fe, Al-Si- $\text{Fe}_2\text{O}_3$ , Al-Si-2% $\text{Al}_2\text{O}_3$  and Al-Si-2%SiC have maximum strengths of 117.3MPa, 215.74MPa, 270.5MPa, 110.82MPa and 150.8MPa respectively. The hardness obtained in the above cases are  $26.1 \pm 5.2$ ,  $39.6 \pm 5.6$ ,  $61.9 \pm 7.5$ ,  $36.9 \pm 6.3$  and  $44.2 \pm 3.9$  on  $R_B$  scale respectively at 1100°C. Hence, the strengths obtained in case of the in-situ composites (Al-Si/ $\text{Fe}_2\text{O}_3$ /Fe) are each about 2 times more that the strength obtained in case of cast Al-Si. Also, hardness values of the in-situ

composites are higher than the values of cast Al-Si by 1.5 times (Al-Si-Fe) and 2.5 times (Al-Si-  $\text{Fe}_2\text{O}_3$ ) respectively.

## SUGGESTIONS FOR FUTURE WORK

---

1. Study of the in-situ composites by increasing the amount of  $\text{Fe}_2\text{O}_3/\text{Fe}$  into the pure Al melt.
2. Evaluation of mechanical properties of in-situ composites by powder metallurgy route and compared those with the in-situ composites produced by melting route.
3. Development of mathematical model based on porous-bed phenomenon to predict the composite growth.

**Table 2.1** Heat capacity of different materials. [51]

Material	Heat capacity( $C_p$ in J/mole.K)
Al,Fe	25
$Fe_3O_4$	48
$Al_2O_3$	25

**Table 2.2** Crystal structure and stability range of the phases formed in Fe–Al binary system at room temperature. [44, 76]

Phases	Crystal structure	Stability range (at.%)	Density ( $Mg\ mm^{-3}$ )
Fe solid solution	BCC	0–45	7.8
$\gamma$ -Fe	FCC	0–1.3	7.8
FeAl ( $\beta_2$ )	BCC (order)	23–55	5.58
$Fe_3Al$ ( $\beta_1$ )	Do3	23–34	6.72
$Fe_2Al_3$ ( $\epsilon$ )	Cubic (complex)	58–65	–
$FeAl_2$ ( $\zeta$ )	Triclinic	66–66.9	–
$Fe_2Al_5$ ( $\eta$ )	Orthorhombic	70–73	4.11
$FeAl_3$ ( $\theta$ )	Monoclinic	74.5–76.5	3.9
Al solid solution	FCC	99.998–100	2.69

**Table 2.3** Thermodynamic constants for the intermetallic phases form in Fe–Al binary system [62]

Intermetallic compound	$\Delta H_{298}$ ( $J\ mol^{-1}$ )	$\Delta S_{298}$ ( $K^{-1}\ mol^{-1}$ )	$\Delta G_{973}$ ( $J\ mol^{-1}$ )
FeAl <sub>3</sub> ( $\theta$ )	–112360	95.6	–22869
$Fe_2Al_5$ ( $\eta$ )	–194040	166.7	–19636
$FeAl_2$ ( $\zeta$ )	–81900	73.3	–16999
FeAl ( $\beta_2$ )	–51240	51	–11090
$Fe_3Al$ ( $\beta_1$ )	–57372	28	–4827

**Table 2.4.** Phase reactions in Fe–Al phase diagram. [76]

Reaction	Reaction composition (at.% Al)	Reaction temperature (°C)	Reaction type
$\alpha\text{Fe} \leftrightarrow \text{FeAl}$	45	1310	Critical
$\text{L} + \text{FeAl} \leftrightarrow \text{Fe}_2\text{Al}_3$	52	1232	Peritectic
$\text{L} \leftrightarrow \text{Fe}_2\text{Al}_3 + \text{Fe}_2\text{Al}_5$	70.5	1165	Eutectic
$\text{L} \leftrightarrow \text{Fe}_2\text{Al}_5 + \text{FeAl}_3$	72	1160	Unknown
$\text{L} \leftrightarrow \text{FeAl}_3 + \text{Al}$	76.6	655	Eutectic
$\text{Fe}_2\text{Al}_3 + \text{Fe}_2\text{Al}_5 \leftrightarrow \text{FeAl}_2$	70	1156	Peritectoid
$\text{Fe}_2\text{Al}_3 \leftrightarrow \text{FeAl} + \text{FeAl}_2$	55	1102	Eutectoid
$\text{L} \leftrightarrow \text{Fe}_2\text{Al}_5$	71	1169	Congruent
$\alpha\text{Fe} \leftrightarrow \text{FeAl}$	23.9	662	Tricritical
$\text{FeAl} \leftrightarrow \text{Fe}_3\text{Al}$	26.5	552	Critical
$\text{L} \leftrightarrow \delta\text{Fe}$	0	1538	Melting
$\text{L} \leftrightarrow \text{Al}$	100	660	Melting
$\delta\text{Fe} \leftrightarrow \gamma\text{Fe}$	0	1394	Allotropic
$\gamma\text{Fe} \leftrightarrow \alpha\text{Fe}$	0	912	Allotropic
Metastable phase, $\text{L} \leftrightarrow \text{kFeAl}_5 + \text{Al}$	85.7	653	Eutectic

Table 3.1 Weight gain of pure cast Al-Si in various conditions.

Expt. No	Type of Crucible	Temp °C	No of Stirrings. (Each of 30 Sec).	Initial Wt. of Al.(W <sub>1</sub> ), gm.	Final Wt. of Al.(W <sub>2</sub> ), gm.	Difference in weight. $\Delta W = (W_2 - W_1)$ gm.	% of Wt. gain
1	Alumina Tube	800	5	63.2745	63.9962	0.7215	1.140
2	Alumina Tube	800	10	64.9345	66.1737	1.2392	1.908
3	Alumina Tube	1000	5	65.9419	66.7665	0.8246	1.250
4	Alumina Tube	1000	10	66.6830	67.8982	1.2152	1.822
5	Alumina Tube	1100	5	66.9569	67.7487	0.7918	1.182
6	Alumina Tube	1100	10	66.9132	68.1344	1.2212	1.825
7	Graphite Crucible	800	5	72.4149	73.4975	1.0826	1.494
8	Graphite Crucible	800	10	75.1142	76.7355	1.6213	2.158
9	Graphite Crucible	1000	5	74.7651	75.8446	1.0795	1.443
10	Graphite Crucible	1000	10	73.1975	74.8388	1.6413	2.242
11	Graphite Crucible	1100	5	76.2324	77.3456	1.1132	1.460

\*In all experiment cooling was done in air.

**Table 3.2** Weight gain, loss of pure Al-Si/Fe when Fe was inserted into the Al melt at temp 800°C / 1100°C.

Expt. No	Temp °C	Initial Wt. of Al (W <sub>1</sub> ), gm.	Initial Wt. of Fe Sample, gm.(W <sub>2</sub> )	Final Wt. of solidified metal, gm.(W <sub>f</sub> )	Final Wt. of Fe sample (W <sub>f2</sub> ), gm.	Wt. gain of solidified metal, gm. (W <sub>f</sub> -W <sub>1</sub> )	Wt. loss of Fe sample, gm. (W <sub>2</sub> - W <sub>f2</sub> )	% gain in Wt. of Al	% loss in Wt. of Fe
1	800	85.697	6.1413	86.639	5.7386	0.942	0.4027	1.099	6.557
2	800	90.971	6.1407	92.093	5.6277	1.122	0.5130	1.233	8.354
3	1100	88.386	6.1410	91.549	4.1981	3.163	1.9429	3.578	31.638
4	1100	90.654	6.1417	93.538	4.1066	2.884	2.0351	3.181	33.134
5	1100	87.667	6.1409	90.689	4.2553	3.022	1.8856	3.447	30.705

\*No of stirring was kept constant for 10 and cooling was done in air.



**Table 3.3** Weight loss or gain when iron ore added to the Al-Si melt at different temperatures i.e. 800°C / 1100°C.

Expt. No	Temp °C	Initial Wt. of Al(W <sub>1</sub> ), gm.	Wt. of Fe <sub>2</sub> O <sub>3</sub> , gm.(W <sub>2</sub> )	Wt. % of Fe <sub>2</sub> O <sub>3</sub>	Final Wt. of solidified metal, gm.(W <sub>f</sub> )	Wt. of slag, gm.(W <sub>s</sub> )	Wt. of remaining powder, gm. (W <sub>p</sub> )	Wt. loss or gain of metal, (gm) (W <sub>f</sub> -W <sub>1</sub> )	Wt. loss or gain of metal, %
1	800	75.597	7.559	10	75.938	1.324	7.303	0.341	0.451
2	800	41.099	4.109	10	40.9711	1.161	4.064	-0.127	-0.309
3	800	100.826	5.041	5	100.614	1.927	5.491	-0.212	-0.210
4	800	93.346	4.667	5	93.227	1.798	4.195	-0.119	-0.127
5	800	100.621	2.012	2	99.981	0.885	1.729	-0.64	-0.636
6	800	100.818	2.016	2	99.117	1.441	1.811	-1.701	-1.687
7	1100	99.771	9.977	10	98.892	0.578	6.324	-0.879	-0.881
8	1100	73.202	7.320	10	70.432	0.989	5.124	-2.77	-3.784
9	1100	79.815	3.990	5	77.231	0.434	1.492	-2.584	-3.237
10	1100	88.414	4.420	5	84.771	0.553	1.868	-3.643	-4.120
11	1100	93.881	1.877	2	90.992	0.229	0.112	-2.889	-3.077
12	1100	88.515	1.770	2	85.974	0.331	0.091	-2.541	-2.870

\*Cooling was done in air for all experiments.

**Table 4.1** Mechanical properties of cast Al-Si alloy at various conditions.

Type of sample	Temp (°C)	Stirring	Sample cross section.	W (mm)	h (mm)	D (mm)	A (mm <sup>2</sup> )	Load (N)	Strength (MPa)	Hardness R <sub>B</sub> scale
Pure Al			Circular			8.5	56.74	11900	209.7	17.9 ± 3.9
Al-Si cast	800	present	Rectangular	7.6	7.4		56.24	5900	104.9	22.6 ± 6.2
Al-Si cast	1100	No	Rectangular	7.2	7.0		50.40	5300	105.1	23.9 ± 7.3
Al-Si cast	1100	No	Rectangular	7.2	7.0		50.40	5100	101.1	22.8 ± 5.8
Al-Si cast	1100	Present	Rectangular	7.2	7.1		51.12	6000	117.3	25.1 ± 3.6
Al-Si cast	1100	Present	Rectangular	7.2	6.9		49.68	5600	112.7	24.8 ± 5.2
Al-Si cast	1100	No	Rectangular	6.8	6.8		46.24	3700	80.0	24.1 ± 2.7
Al-Si cast	1100	Present	Rectangular	6.9	6.9		47.61	4200	89.5	23.1 ± 4.2
Al-Si cast	1100	Present	Rectangular	6.9	6.8		46.92	4025	85.7	22.6 ± 4.9
Al-Si cast	1100	Present	circular			5.9	27.33	3200	117.0	26.1 ± 5.2

**Table 4.2** Mechanical properties of cast Al- Si alloy with pure Fe at various conditions.

Type of sample	Temp (°C)	stirring	Sample cross section	W (mm)	h (mm)	D (mm)	A (mm <sup>2</sup> )	Load (N)	Strength (MPa)	Hardness R <sub>B</sub> scale.
Cast Al-Si/Fe	800	present	Rectangular	7.6	7.3		55.48	5600	100.9	31.7 ± 4.8
Cast Al-Si/Fe	1100	present	Rectangular	7.1	6.8		48.28	4800	99.4	33.7 ± 6.1
Cast Al-Si/Fe	1100	present	Rectangular	7.2	6.9		49.68	7800	157.0	36.5 ± 5.2
Cast Al-Si/Fe	1100	present	Rectangular	7.2	7.0		50.40	7000	138.8	35.9 ± 4.1
Cast Al-Si/Fe	1100	present	Circular			6.0	28.27	6100	215.74	39.6 ± 5.6

**Table 4.3** Mechanical properties of cast Al- Si alloy with  $\text{Fe}_2\text{O}_3$  at various conditions.

Type of sample	Wt. % of $\text{Fe}_2\text{O}_3$	Temp ( $^{\circ}\text{C}$ )	Sample cross section	W (mm)	h (mm)	D (mm)	A ( $\text{mm}^2$ )	Load (N)	Strength (MPa)	Hardness $R_B$ scale
Al-Si + $\text{Fe}_2\text{O}_3$	5	800	Rectangular	7.5	7.3		54.75	5350	97.7	38.9 $\pm$ 3.3
Al-Si + $\text{Fe}_2\text{O}_3$	5	1100	Rectangular	7.2	6.8		48.96	6400	130.71	43.8 $\pm$ 4.2
Al-Si + $\text{Fe}_2\text{O}_3$	5	1100	Rectangular	7.2	7.0		50.40	6200	123.0	41.4 $\pm$ 4.7
Al-Si + $\text{Fe}_2\text{O}_3$	2	1100	Rectangular	7.2	7.0		50.40	6400	126.98	41.7 $\pm$ 7.1
Al-Si + $\text{Fe}_2\text{O}_3$	2	1100	Rectangular	7.2	6.9		49.68	2700	54.34	35.1 $\pm$ 3.6
Al+Si $\text{Fe}_2\text{O}_3$	2	1100	Rectangular	7.2	7.1		51.12	10150	198.5	58.9 $\pm$ 2.2
Al-Si + $\text{Fe}_2\text{O}_3$	5	1100	Rectangular	7.2	7.1		51.12	7300	142.8	52.7 $\pm$ 5.1
Al-Si + $\text{Fe}_2\text{O}_3$	5	1100	Rectangular	7.2	7.0		50.40	10400	206.3	59.2 $\pm$ 3.2
Al-Si + $\text{Fe}_2\text{O}_3$	2	1100	Circular			6.0	28.27	6600	233.42	59.9 $\pm$ 8.2
Al+Si $\text{Fe}_2\text{O}_3$	2	1100	Circular			5.9	27.33	5200	190.1	55.3 $\pm$ 4.3
Al-Si + $\text{Fe}_2\text{O}_3$	5	1100	Circular			6.0	28.27	7600	268.8	61.7 $\pm$ 5.2
Al-Si + $\text{Fe}_2\text{O}_3$	5	1100	Circular			6.0	28.27	7650	270.5	61.9 $\pm$ 7.1

**Table 4.5** Mechanical properties of cast Al-Si alloy with 2% SiC at 1100°C.

Type of sample	Wt. % of SiC	Temp (°C)	Sample cross section	W (mm)	h (mm)	A (mm <sup>2</sup> )	Load (N)	Strength (MPa)	Hardness R <sub>B</sub> scale
Al-Si + SiC	2	1100	Rectangular	7.2	7.1	51.12	7200	140.9	41.6 ± 4.6
Al-Si + SiC	2	1100	Rectangular	7.1	7.1	50.41	7600	150.8	44.2 ± 3.9

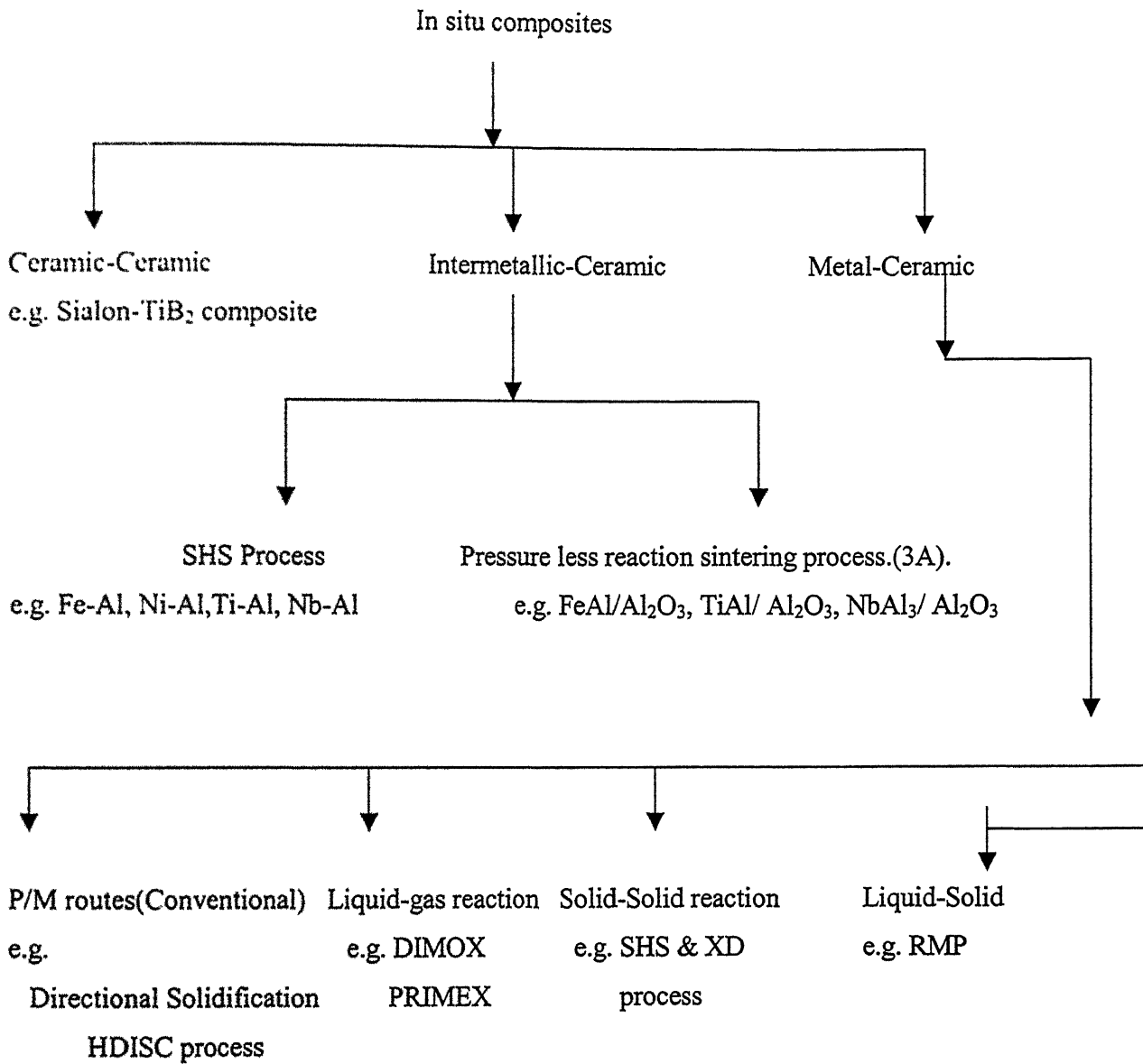


**Fig 1.1** Classification of in situ Composites.

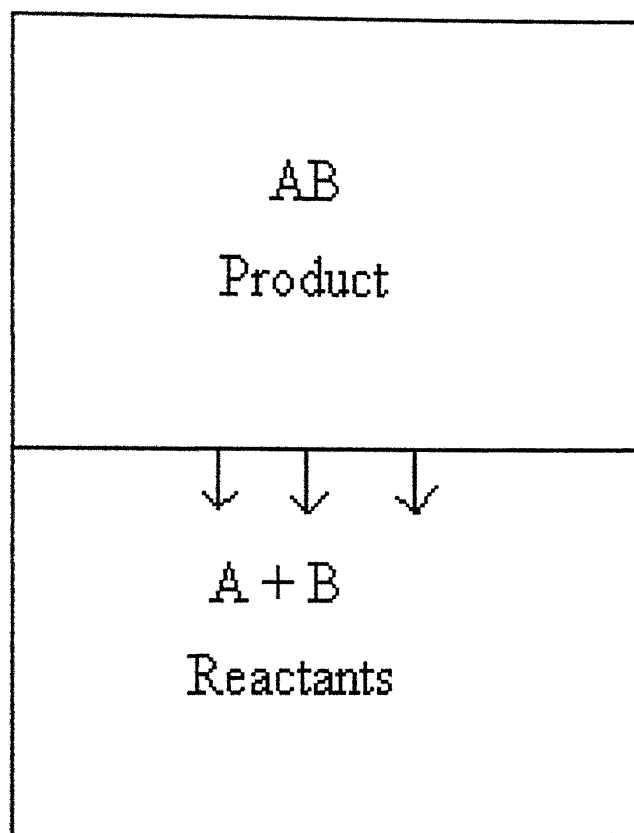


**Fig. 2.1(a)** Schematic representation of SHS process.

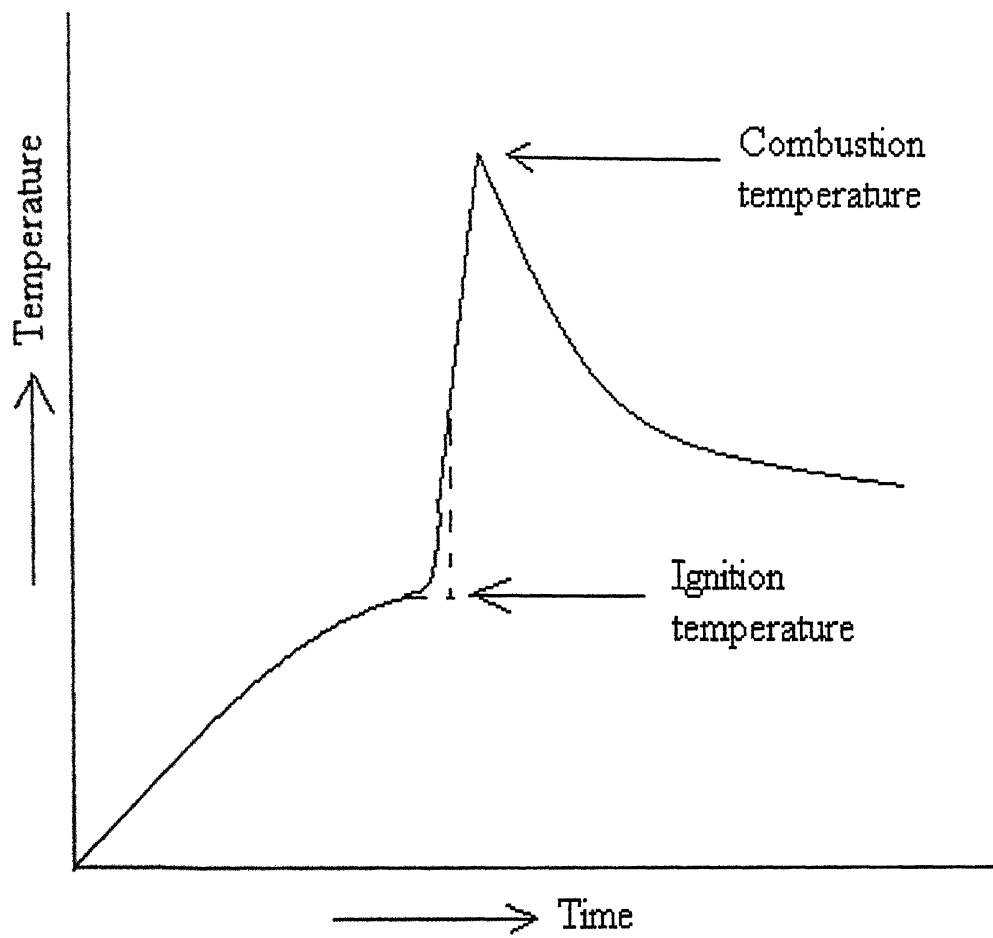


**Fig. 2.1(b)** Schematic representation of the temperature profile associated with passage of a combustion front



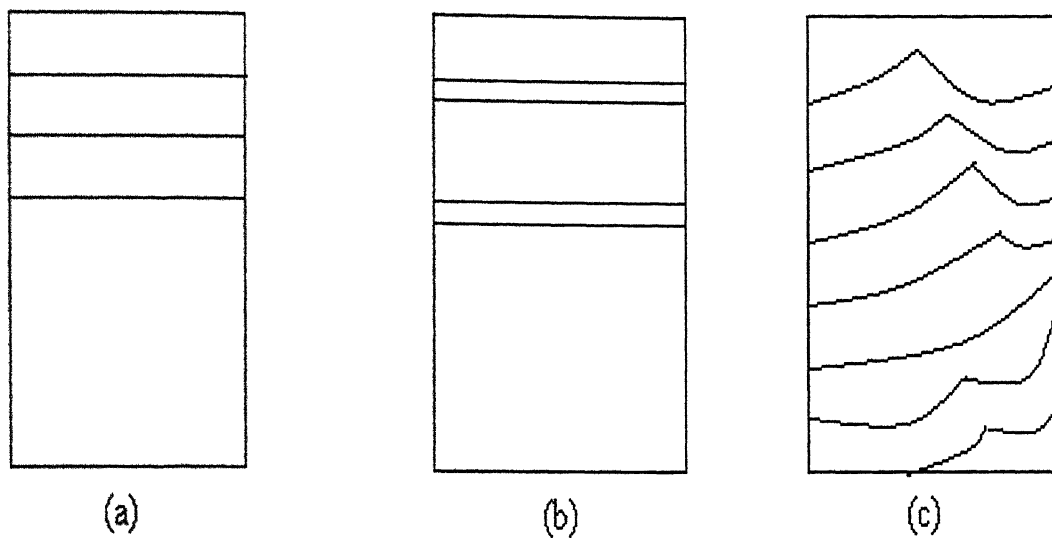
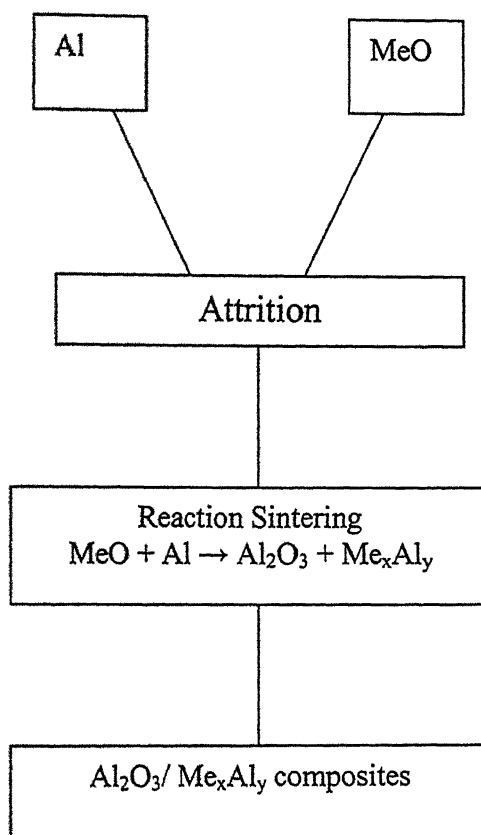


**Fig. 2.1(c)** Schematic representation of combustion wave propagation:  
 (a) Steady state, (b) Oscillatory, (c) Spin.

Route (a)



Route (b)

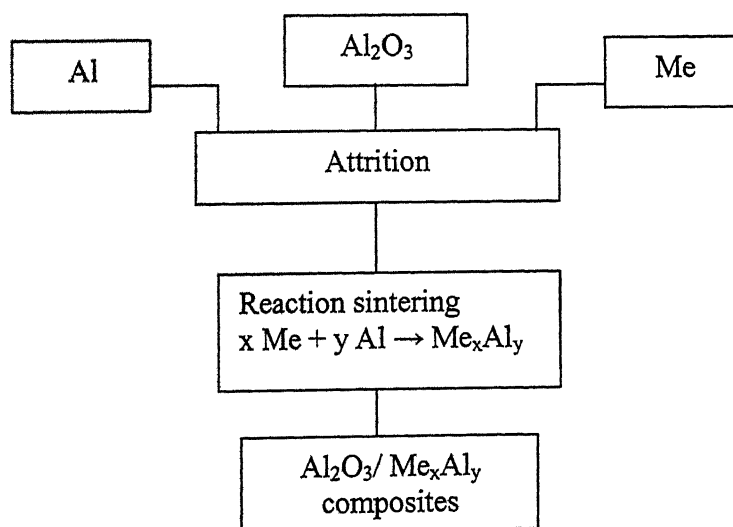


**Fig. 2.2** Two different 3A processing routes



**Fig. 2.3** Transmission electron micrographs of the shock consolidated specimens of (a) Al-10.7 pct Fe powder MA for 65h and (b) Al-25 pct Fe powder MA for 15h showing the presence of 25-30 nm nanocrystals [21].

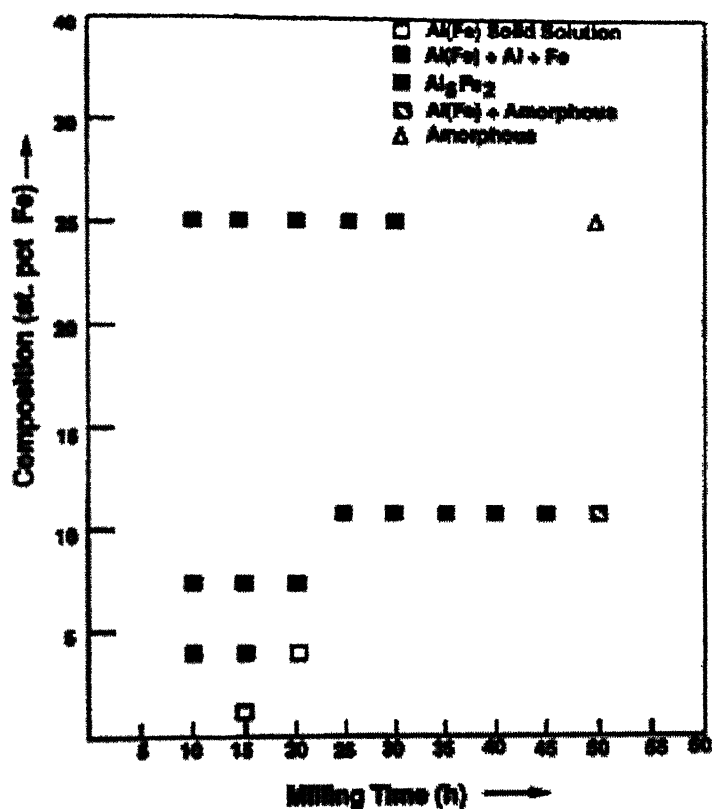
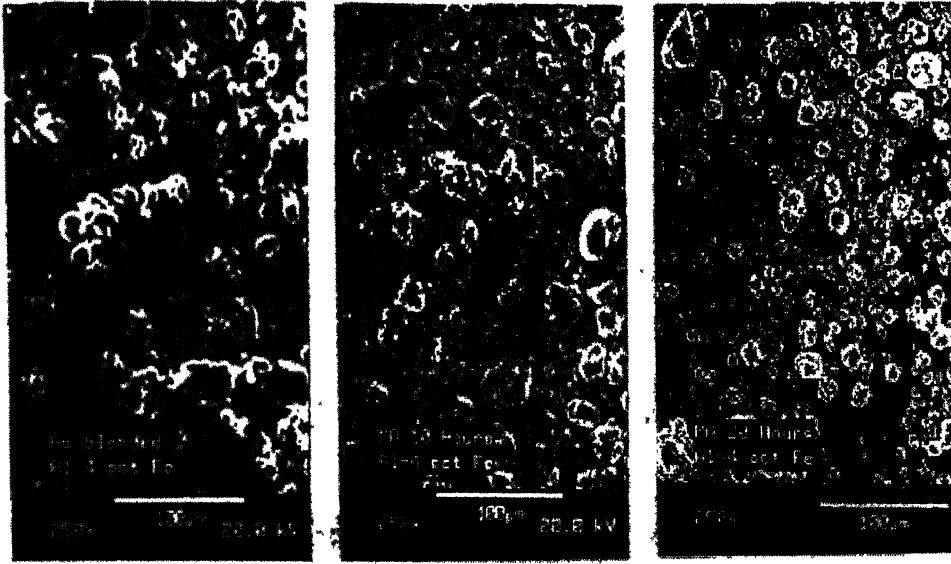
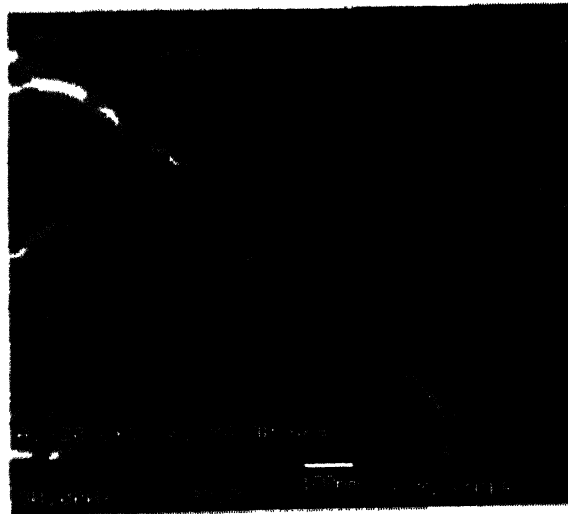


Fig. 2.4 A plot showing the summary of results of MA in different powder mixtures [21].



**Fig. 2.5** Scanning electron micrographs of the Al-4 pct Fe powder (a) as-blended (b) milled for 10h and (c) milled for 20h showing a decrease in the particle size with milling time [21].



**Fig. 2.6** Scanning electron micrograph of the Al-10.7 pct Fe powder MA for 30h, showing the presence of nanometer sized particles [21].

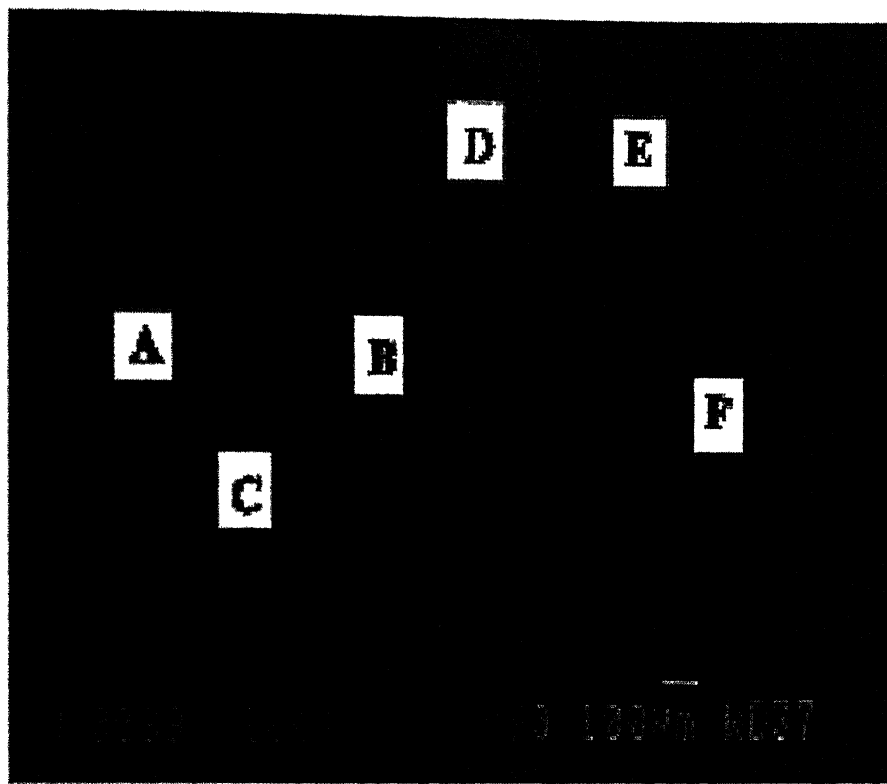


**Fig. 2.7** Backscattered SEM micrograph showing the cross section of the aluminum and  $\text{Fe}_2\text{O}_3$  interface reacted at  $1000^\circ\text{C}$  for 2 hours. A: Al, B:  $\text{Al}_2\text{O}_3$  and  $\text{FeAl}_x$  composite. C:  $\text{FeO}_x$  phase 1, D:  $\text{FeO}_x$  phase 1, E:  $\text{FeO}_x$  phase ii, F:  $\text{Fe}_2\text{O}_3$  [23].

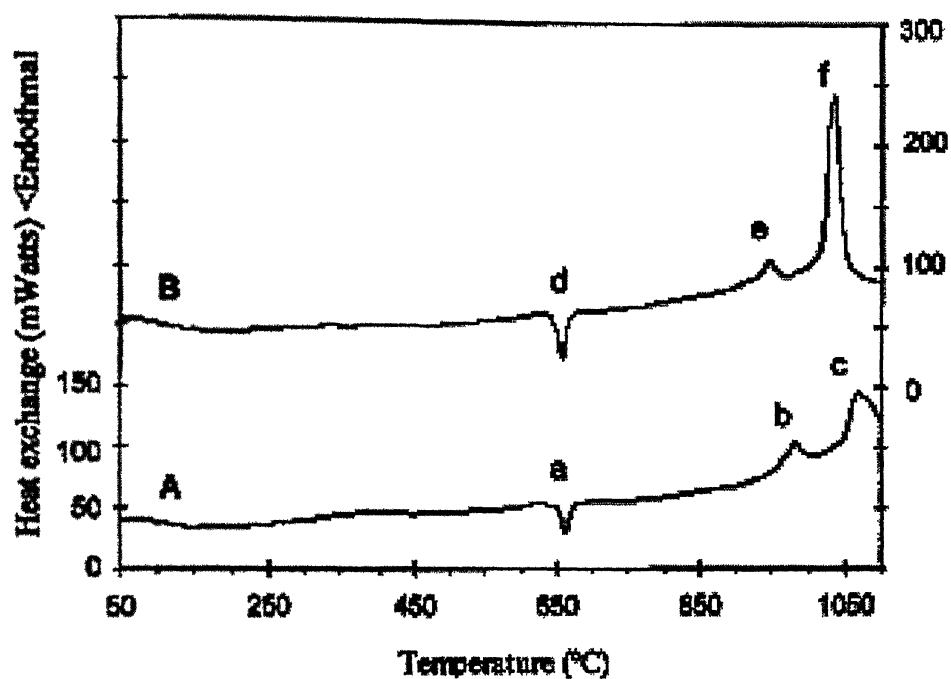


**Fig. 2.8** DTA spectra of mixed Al/Fe<sub>2</sub>O<sub>3</sub> samples. Top: pressed pellet, bottom: powder sample [23].

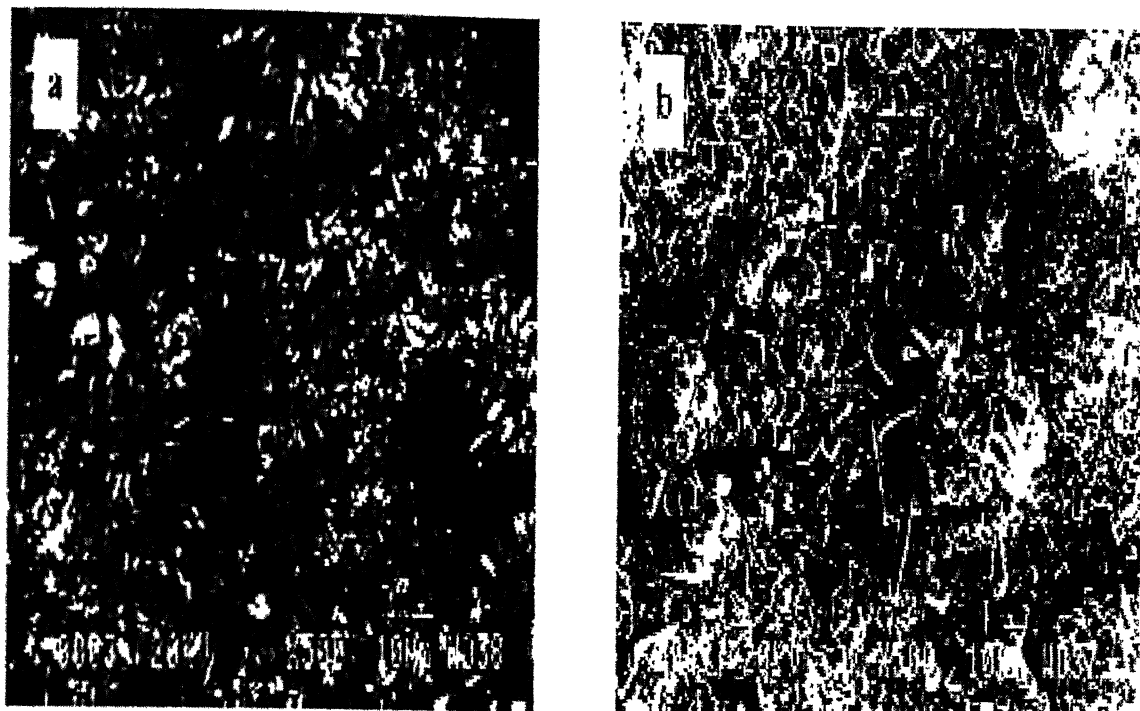


**Fig. 2.9** SEM images of the top surface of the pressed discs of Al and  $\text{Fe}_2\text{O}_3$  after a reaction at  $960^\circ\text{C}$  or  $1060^\circ\text{C}$  for 1 hour in an argon atmosphere. (a).  $960^\circ\text{C}$ , (b),  $1060^\circ\text{C}$  [23].



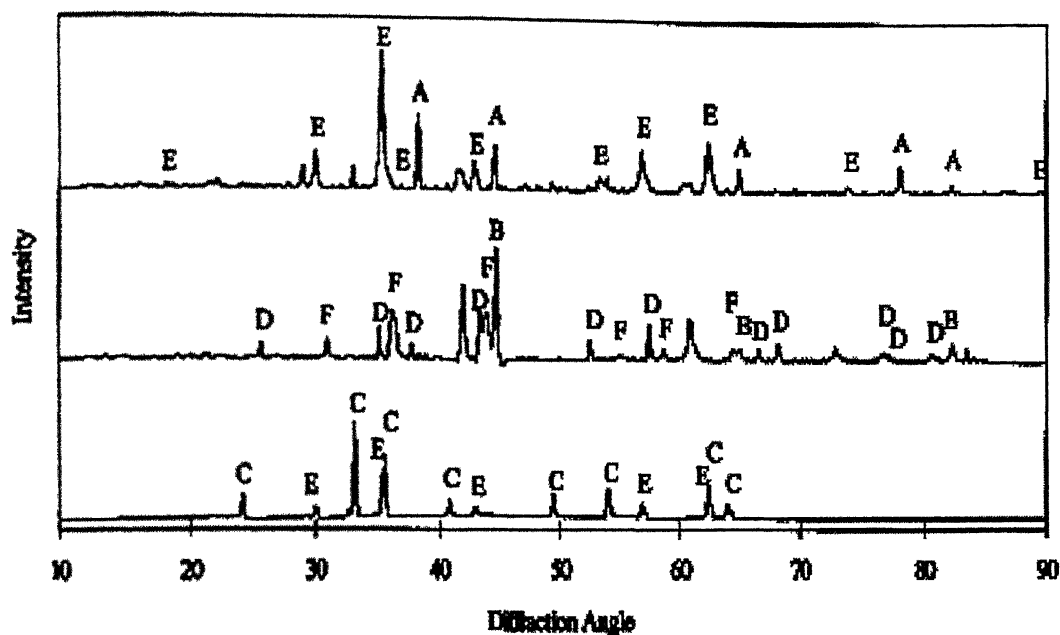


**Fig. 2.10** X-ray diffraction patterns of the reaction products between Al and  $\text{Fe}_2\text{O}_3$ . Top: spectrum of the sample reacted at  $960^\circ\text{C}$  in powder form, middle: spectrum of the sample reacted at  $1060^\circ\text{C}$ . peak A: Al, peak B: Fe, peak C:  $\text{Fe}_2\text{O}_3$ , peak D:  $\text{Al}_2\text{O}_3$ , peak E:  $\text{Fe}_3\text{O}_4$ , peak F:  $\text{FeAl}_2\text{O}_4$  [23].

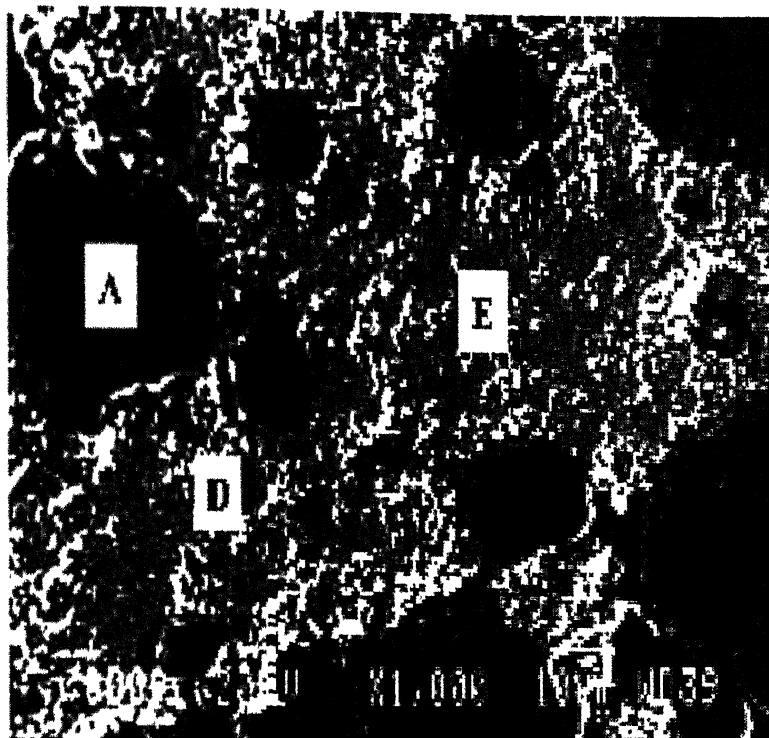


**Fig. 2.11** SEM image of the cross section of the reaction product between Al and  $\text{Fe}_2\text{O}_3$  at  $960^\circ\text{C}$ . A: Al, D:  $\text{Al}_2\text{O}_3$ , E:  $\text{Fe}_3\text{O}_4$  [23].

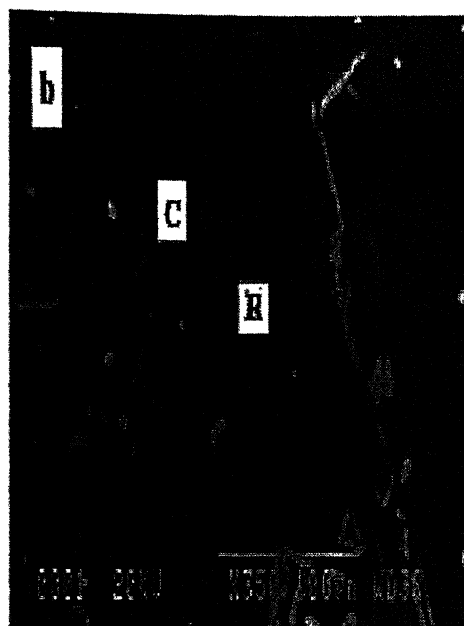


**Fig. 2.12** SEM images of the cross section of Al and  $\text{Fe}_2\text{O}_3$  reacted at  $1060^\circ\text{C}$ , (a), the region near to the top of the surface showing a layer of Fe or Iron oxide formed on the surface, (b), needle shaped single crystals of Fe or its oxide (labeled as C) formed on the top surface, R: embedding resin [23].

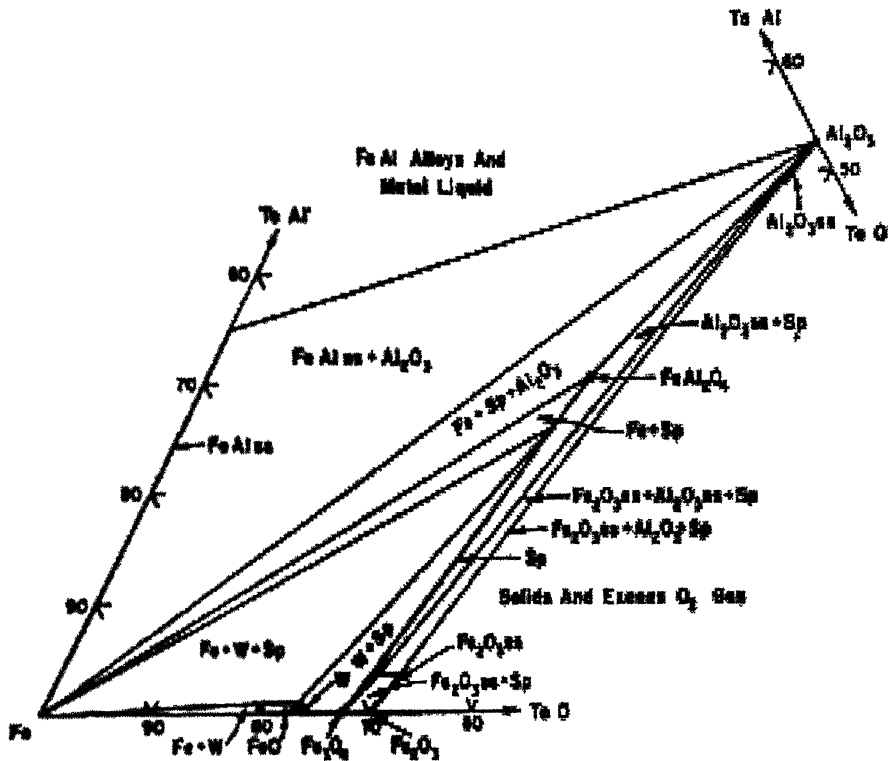
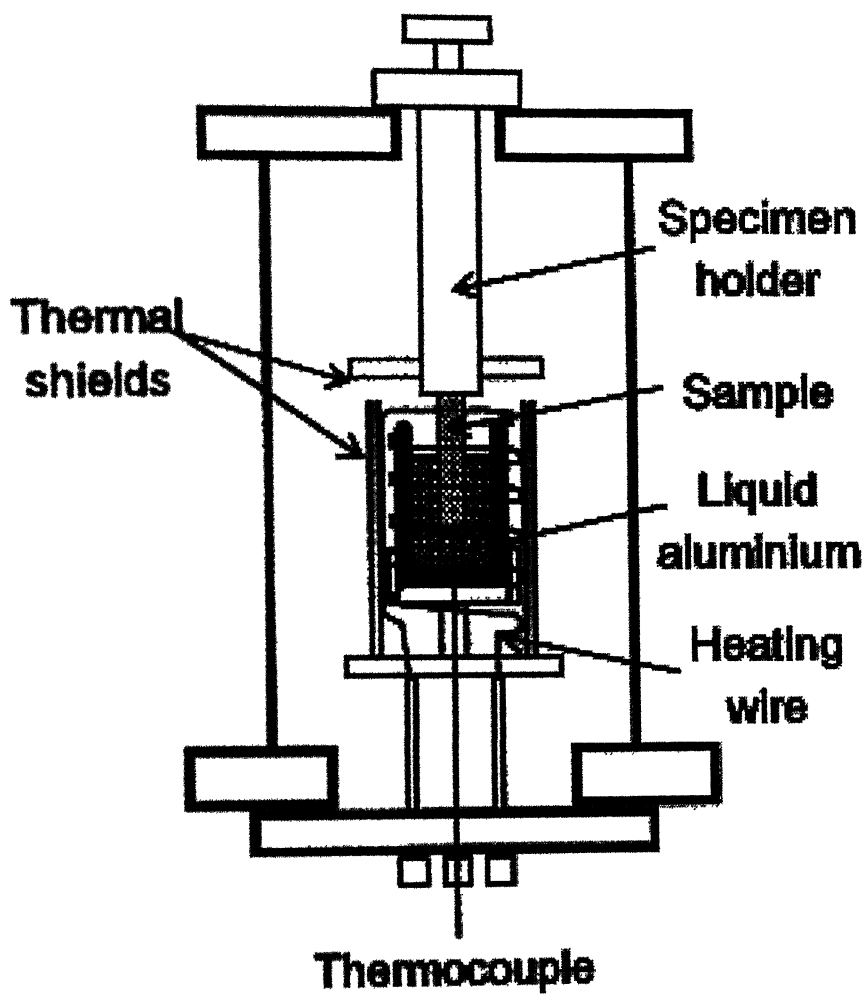


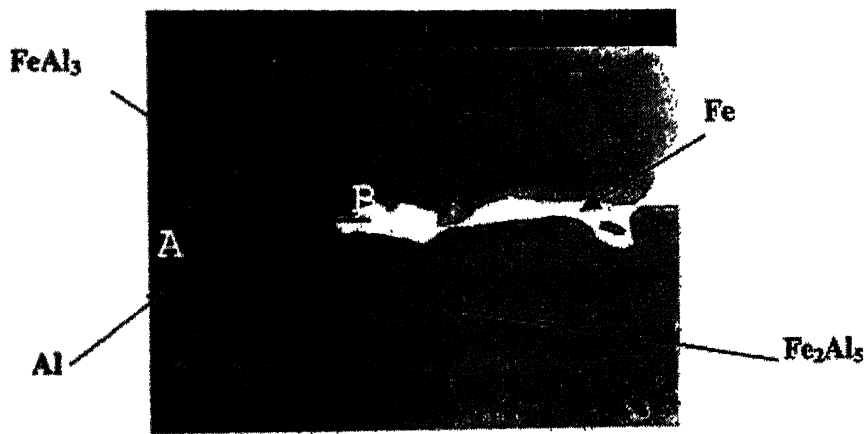
Fig. 2.13 Phase diagram of Fe-Al-O at 1000°C. sp =  $\text{Fe}(\text{Fe},\text{Al})_2\text{O}_4$  spinel, W= Wustite, ss=solid solution [23].



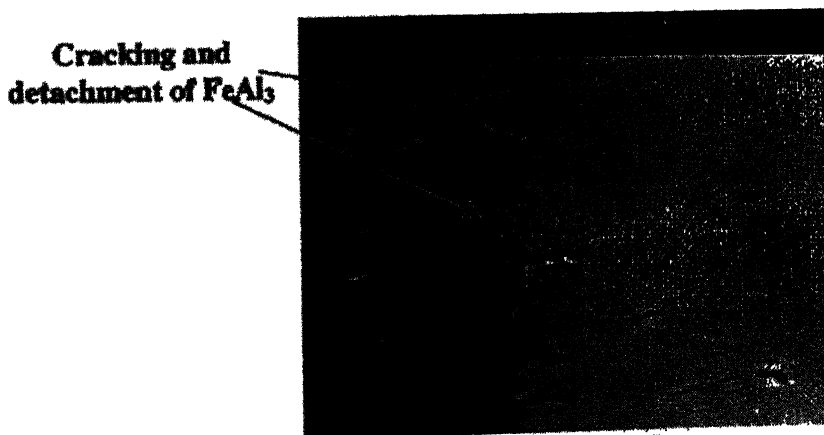
**Fig. 2.14** Schematic view of the device used for immersion tests [51].



(a) 185 seconds

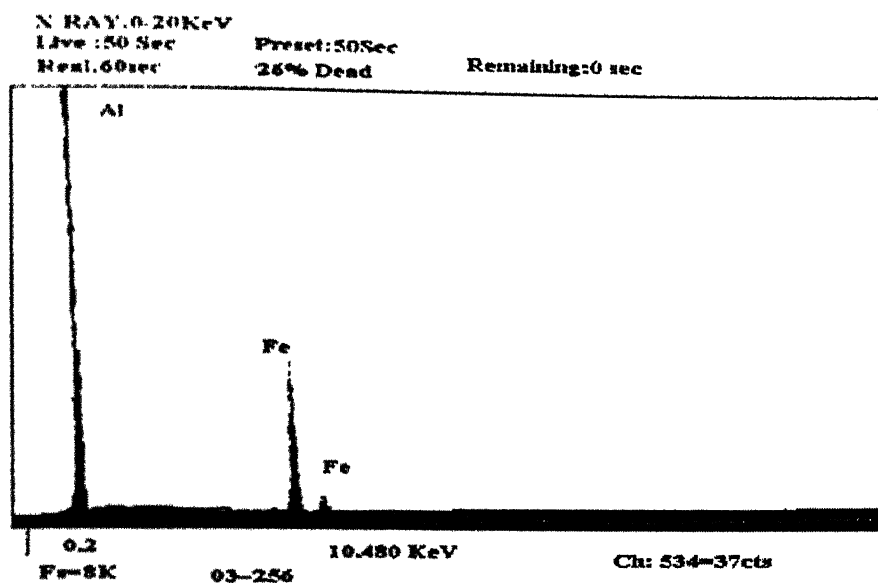


(b) 3000 seconds

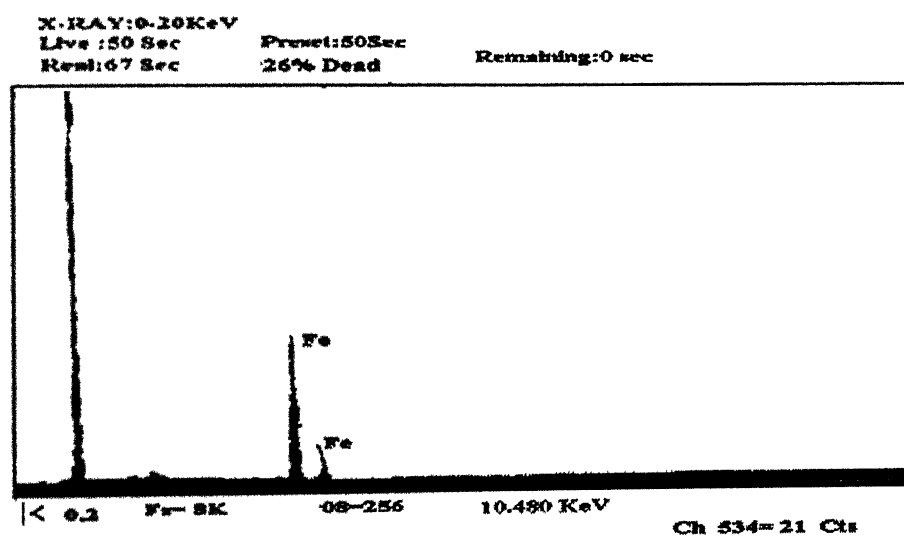


(c) 1500 seconds

**Fig. 2.15** BSE micrographs of the interface layer to show the formation of both  $\text{FeAl}_3$  and  $\text{Fe}_2\text{Al}_5$  intermetallic phases (a, b), and cracking and detachment of the  $\text{FeAl}_3$  (c) [51].

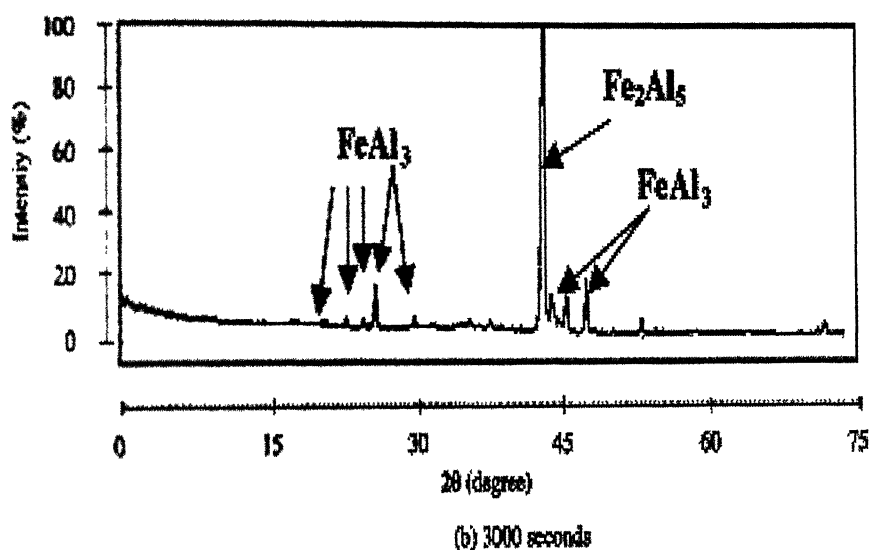
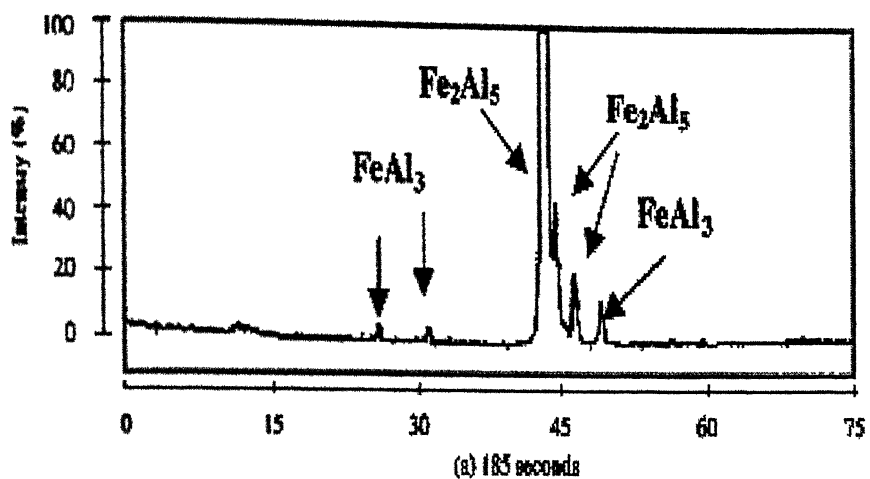


(a) Dark gray phase,  $\text{FeAl}_3$



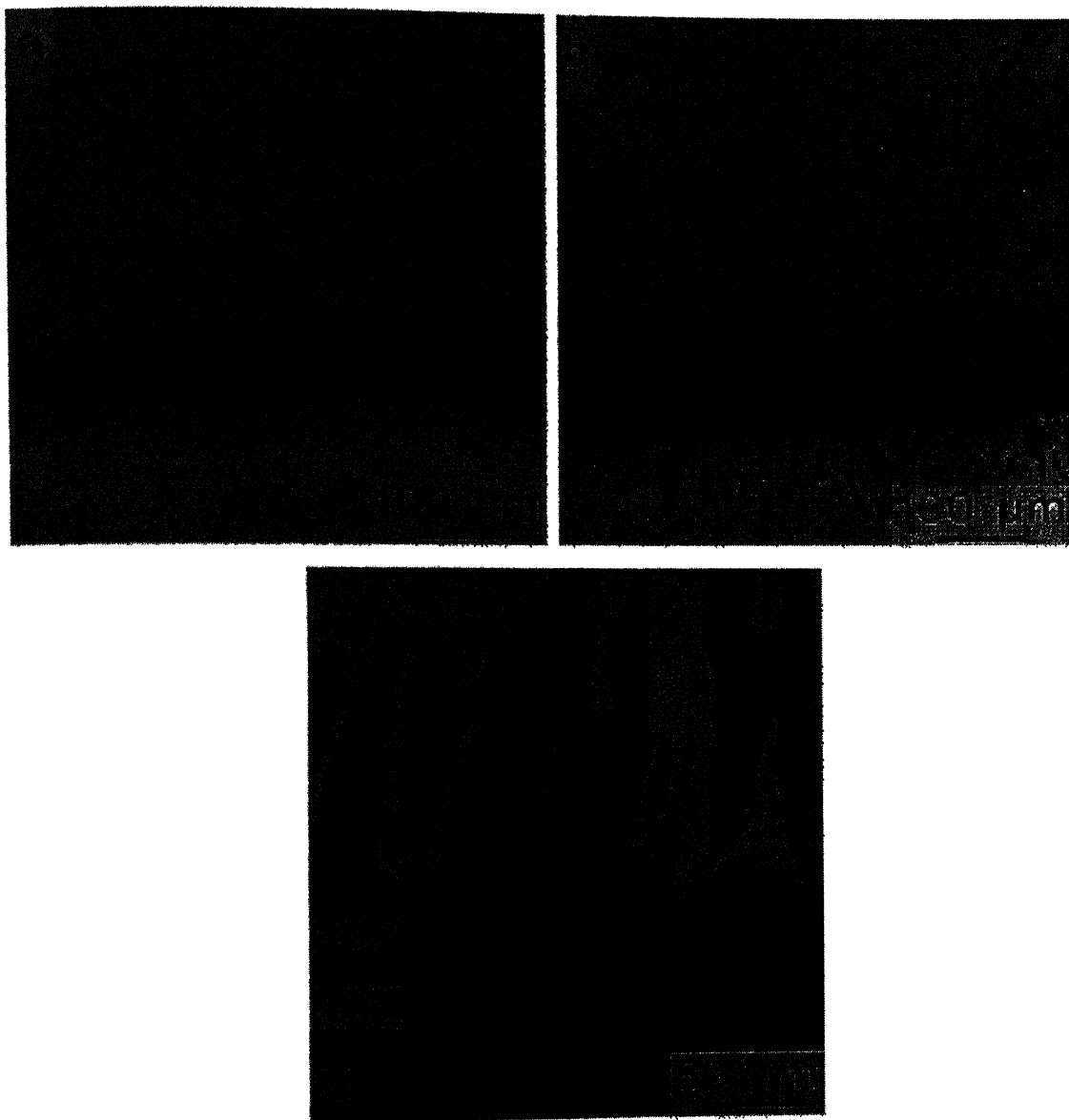
(b) Light gray phase,  $\text{Fe}_2\text{Al}_5$

Fig. 2.16 . EDS spectra of the intermetallic phases in Fig. 2.15 [51].



**Fig. 2.17** XRD spectra of phases formed within iron coupons dipped into molten aluminum [51].





**Fig. 2.18** Intermetallic compounds observed between solid iron and liquid aluminium at  $T=800^{\circ}\text{C}$ : (a) and (b), optical micrographs, respectively for  $t=30$  s and  $t=30$  min; (c) scanning electron micrograph showing  $\text{Fe}_2\text{Al}_5$  and  $\text{FeAl}_3$  formed after an immersion time equal to 15 min [51].

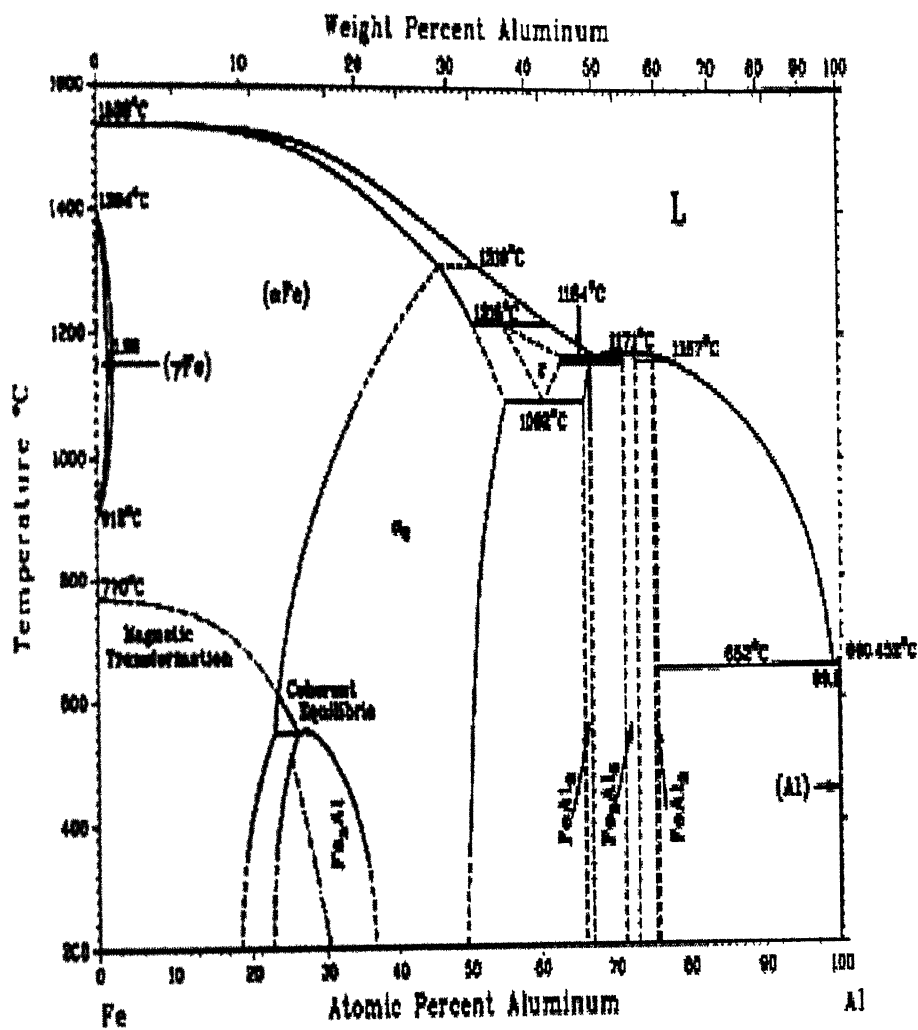
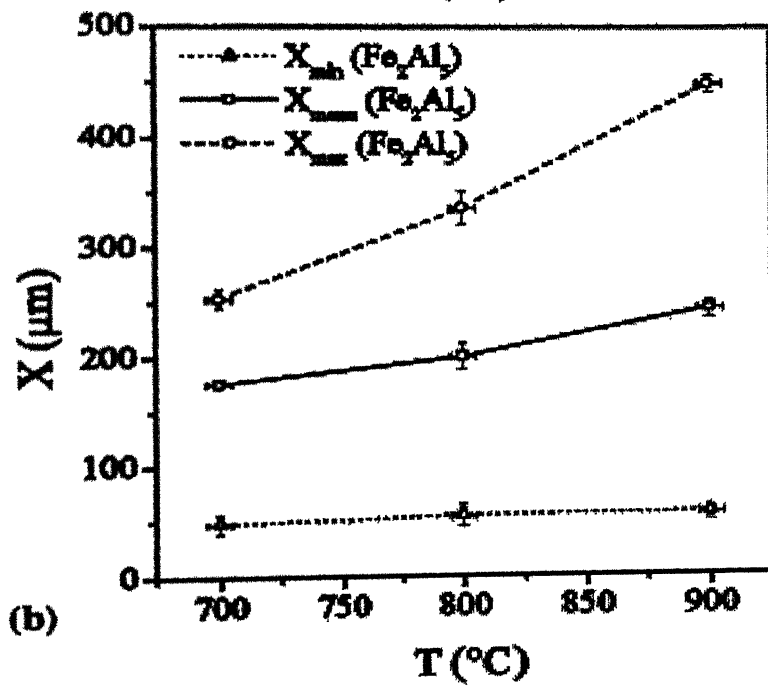
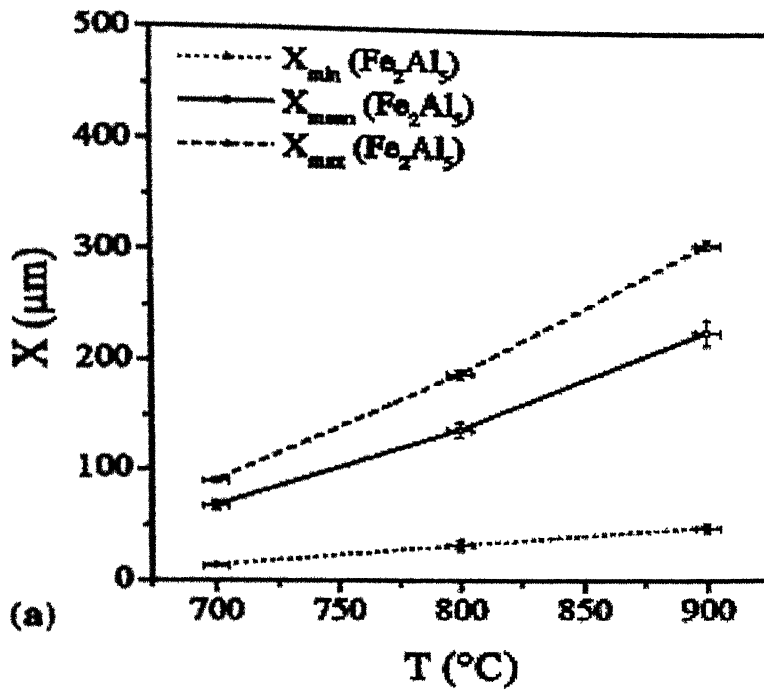
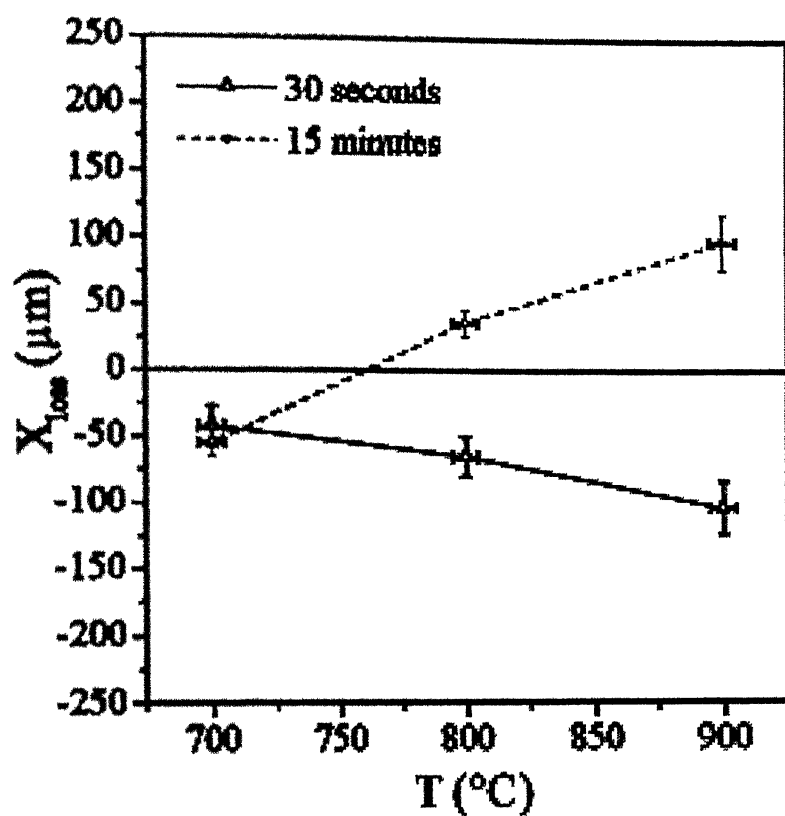


Fig. 2.19 Al-Fe phase diagram [44]



**Fig. 2.20** Temperature dependence of the  $\text{Fe}_2\text{Al}_5$  layer thickness: (a)  $t=30$  s; (b)  $t=15$  min [51].



**Fig. 2.21** Thickness loss of the solid versus temperature for two immersion times [51].

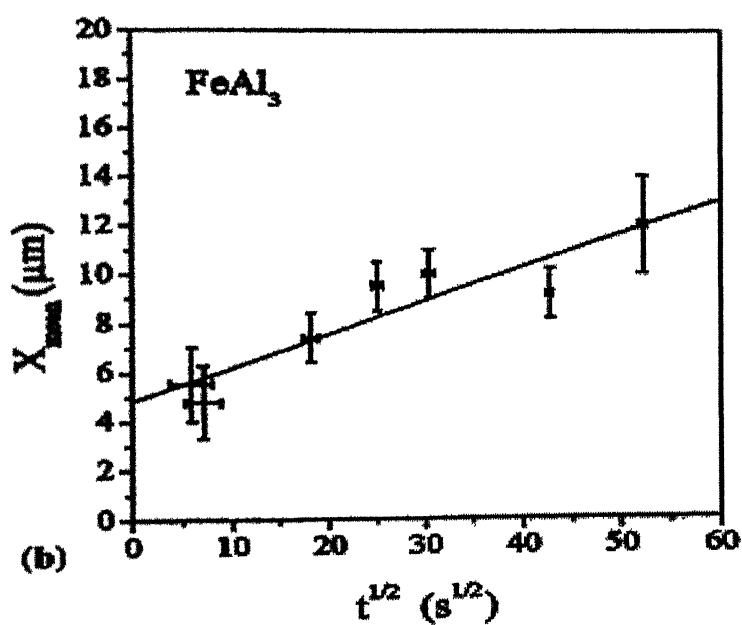
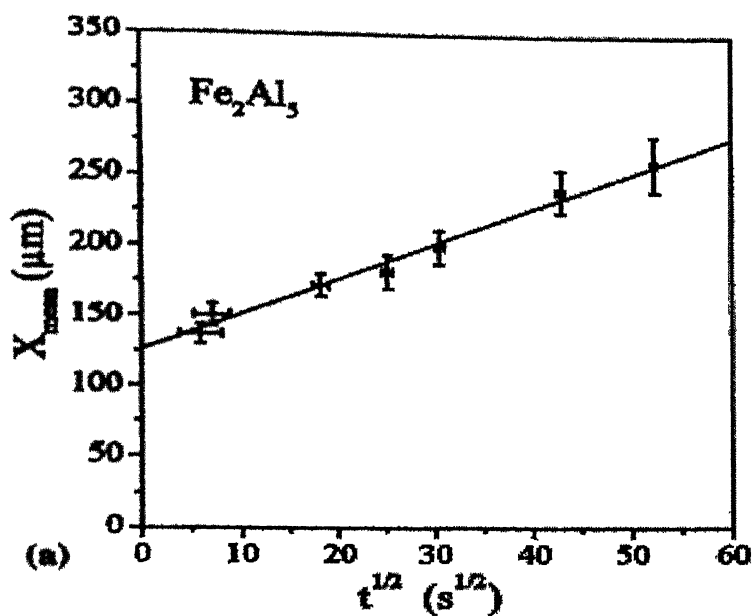
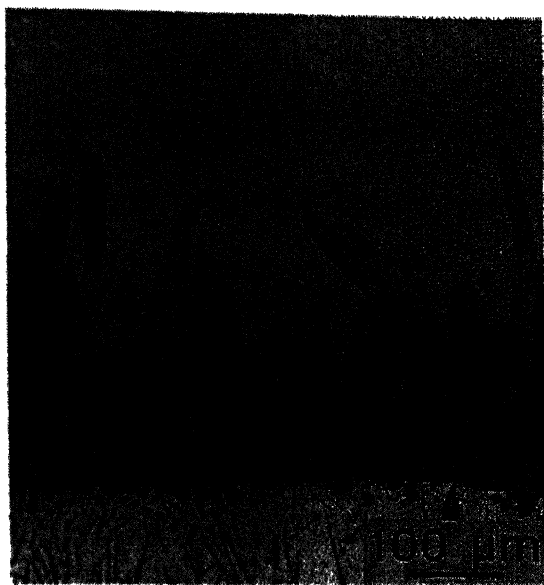
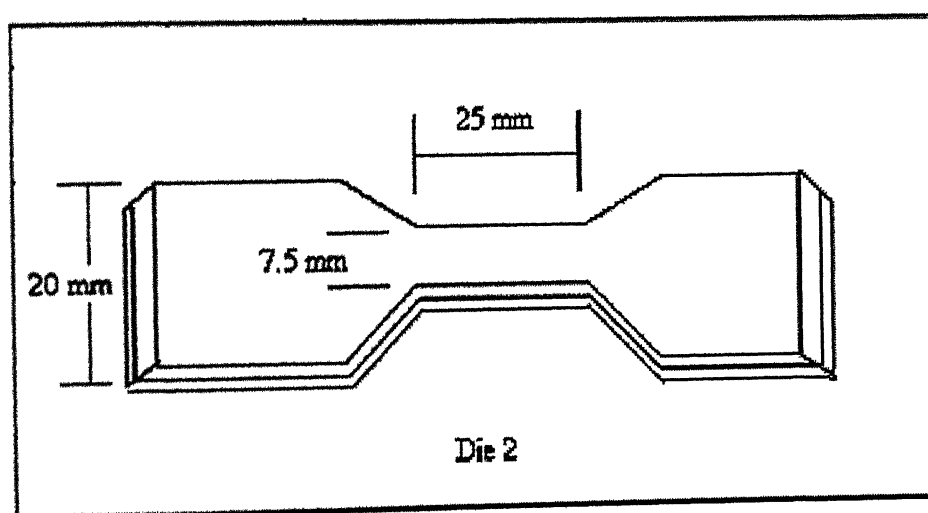
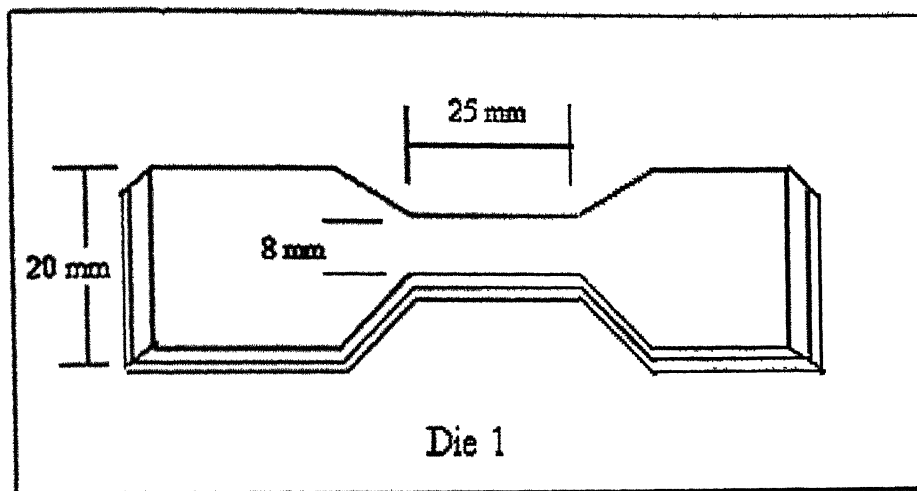


Fig. 2.22 Variation of the layer average thickness with  $t^{1/2}$  at  $T=800^\circ\text{C}$ : (a)  $\text{Fe}_2\text{Al}_5$ ; (b)  $\text{FeAl}_3$  [51].



**Fig. 2.23** Microstructure of the interface zone ( $T=800^{\circ}\text{C}$ ,  $t=15$  min) after etching: Fe is etched with 5% Nital and  $\text{Fe}_2\text{Al}_5$  is etched with 10% NaOH [51].



**Fig 3.1** Dimension of tensile test specimen die

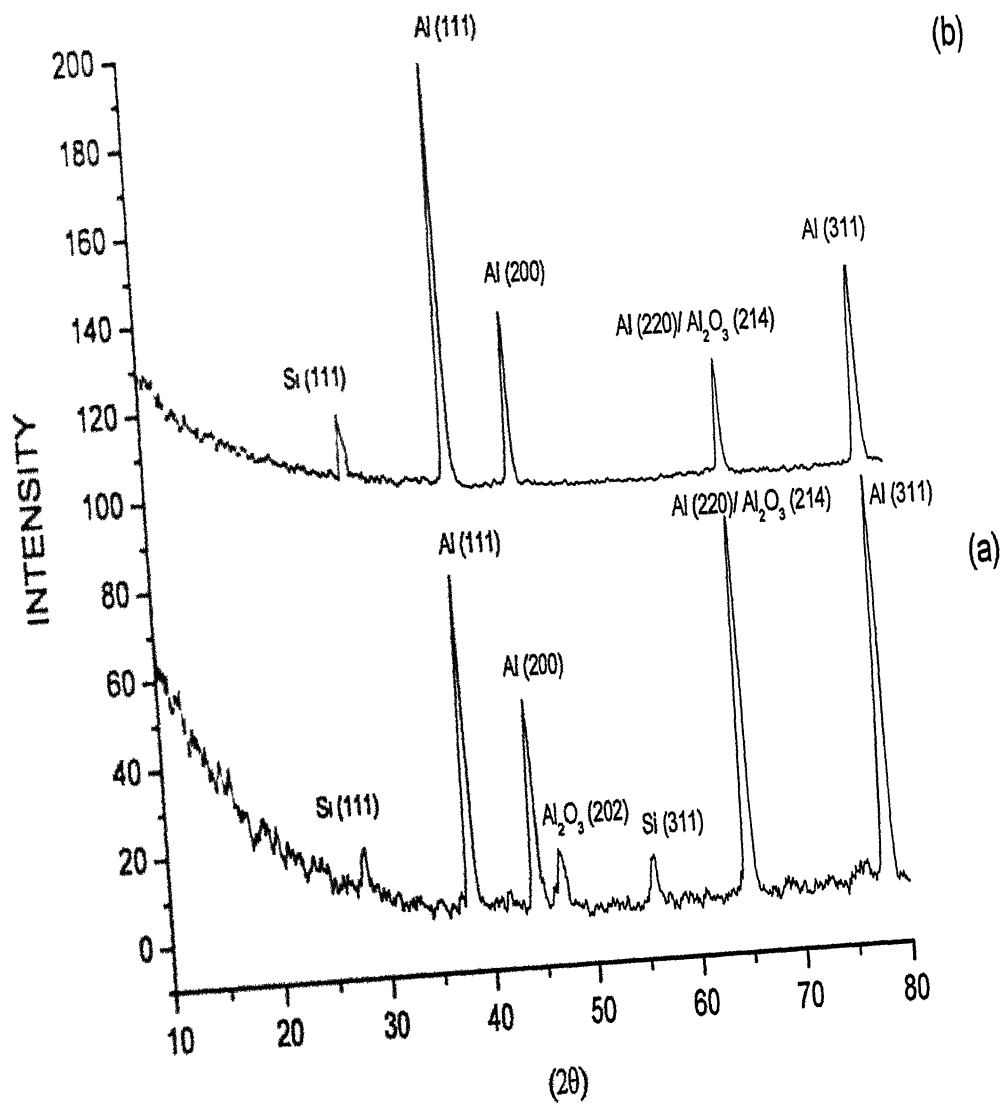
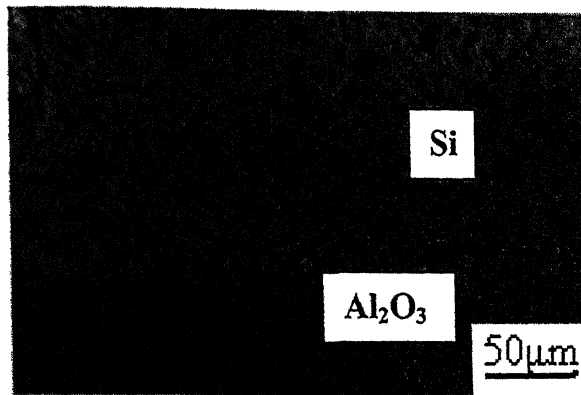
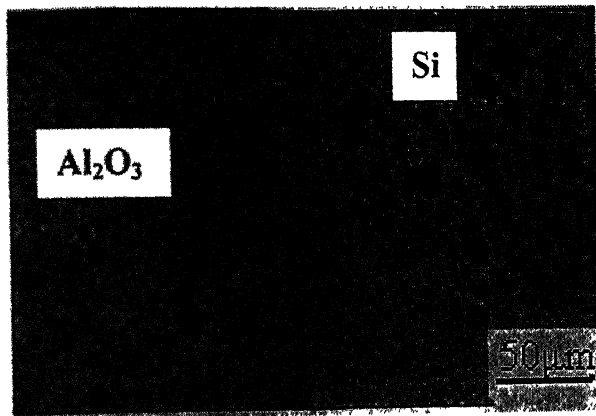


**Fig 4.1** XRD pattern of cast Al-Si base alloy (a) at 800 °C, (b) at 1100 °C.

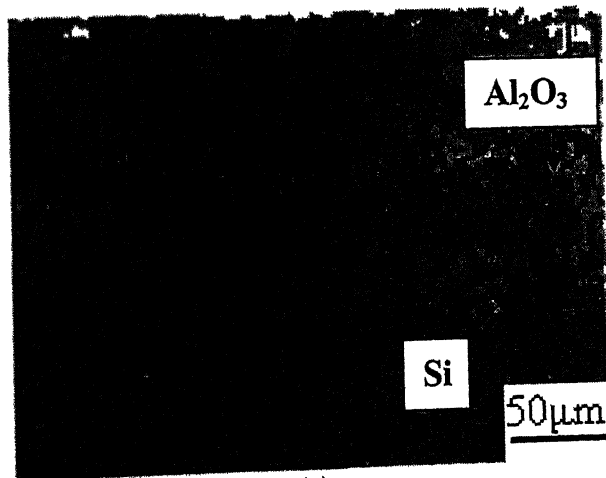




(a)



(b)



(c)

**Fig. 4.2** Shows the optical micrograph of cast Al- Si base alloy at 200 X. (a), (b) at 800°C, and (c) at 1100°C. Micrograph shows the Si flakes along with some modified Si and some distributed alumina.

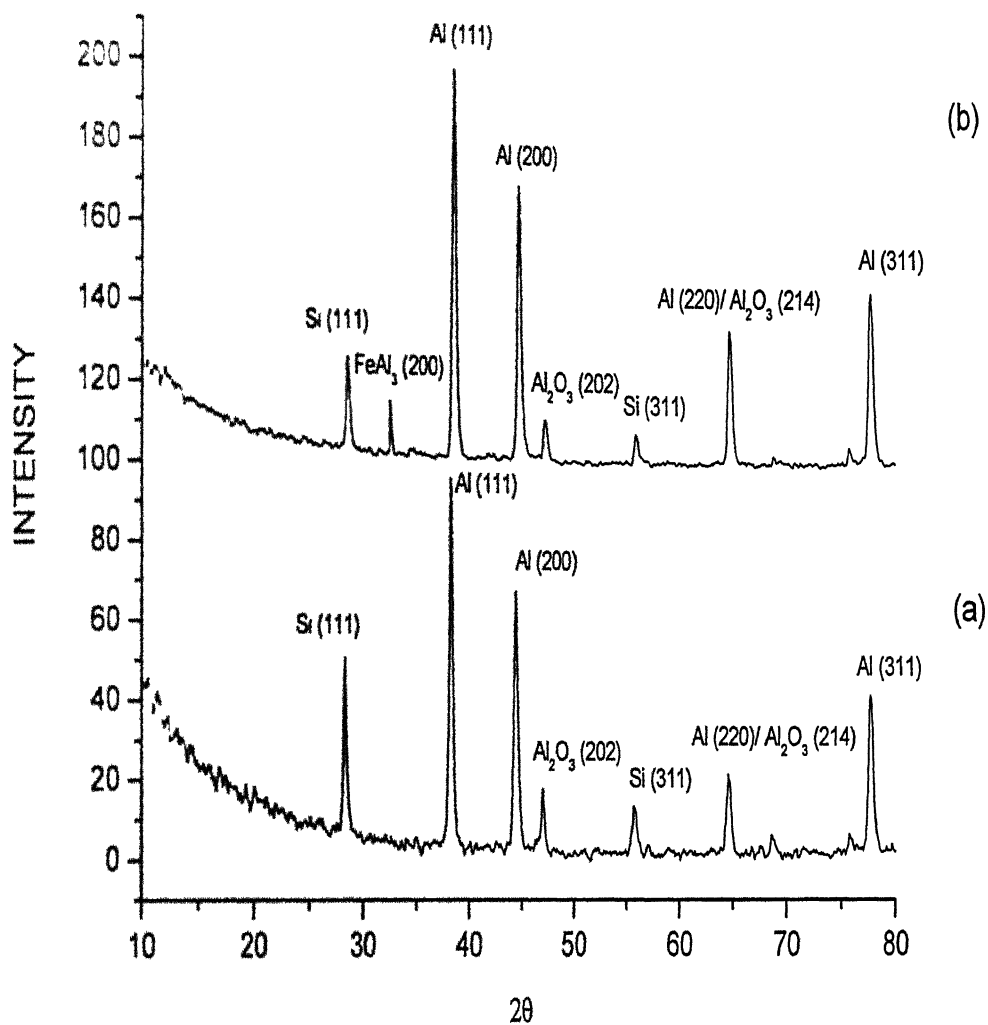
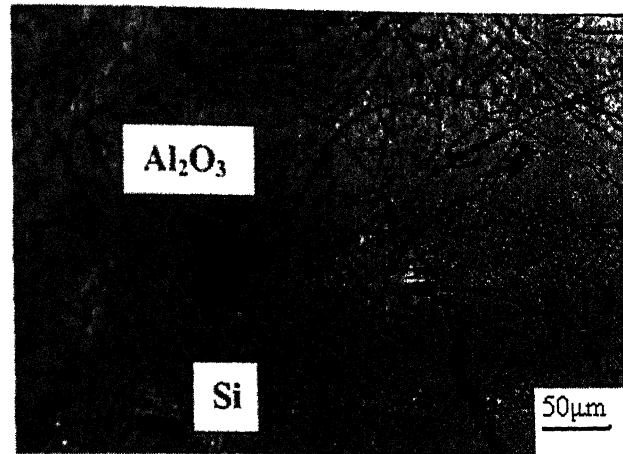
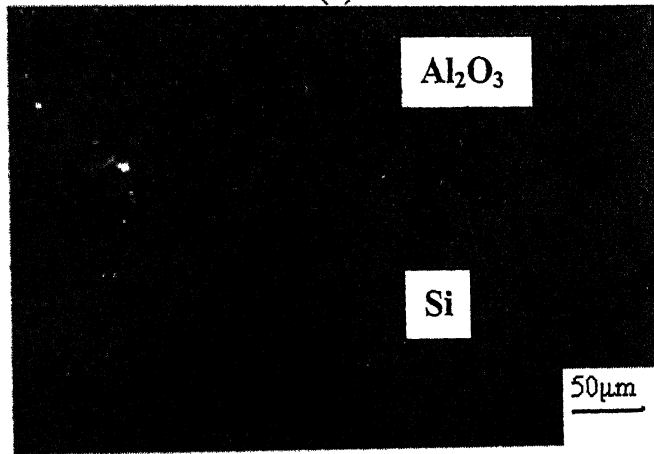


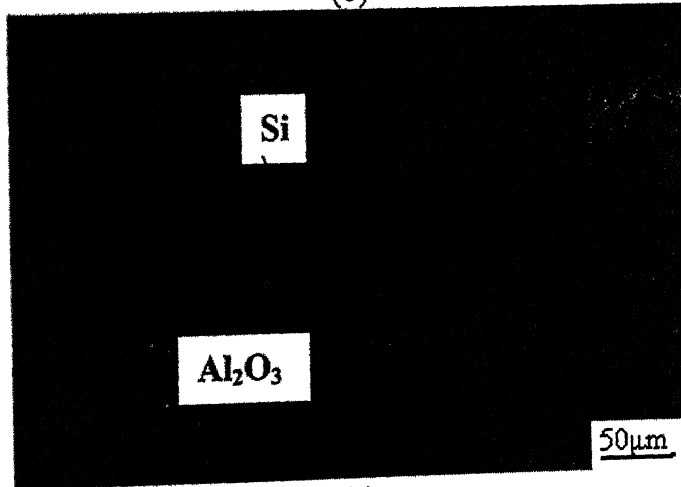
**Fig. 4.3** XRD pattern of cast Al-Si base alloy with pure Fe (a) at 800°C, (b) at 1100°C.



(a)



(b)



(c)

**Fig. 4.4** Shows the optical micrograph of cast Al- Si base alloy with pure Fe at 200 X. (a) at 800°C, (b) and (c) at 1100°C. Micrograph shows the presence of distributed alumina in the Al- Si matrix.

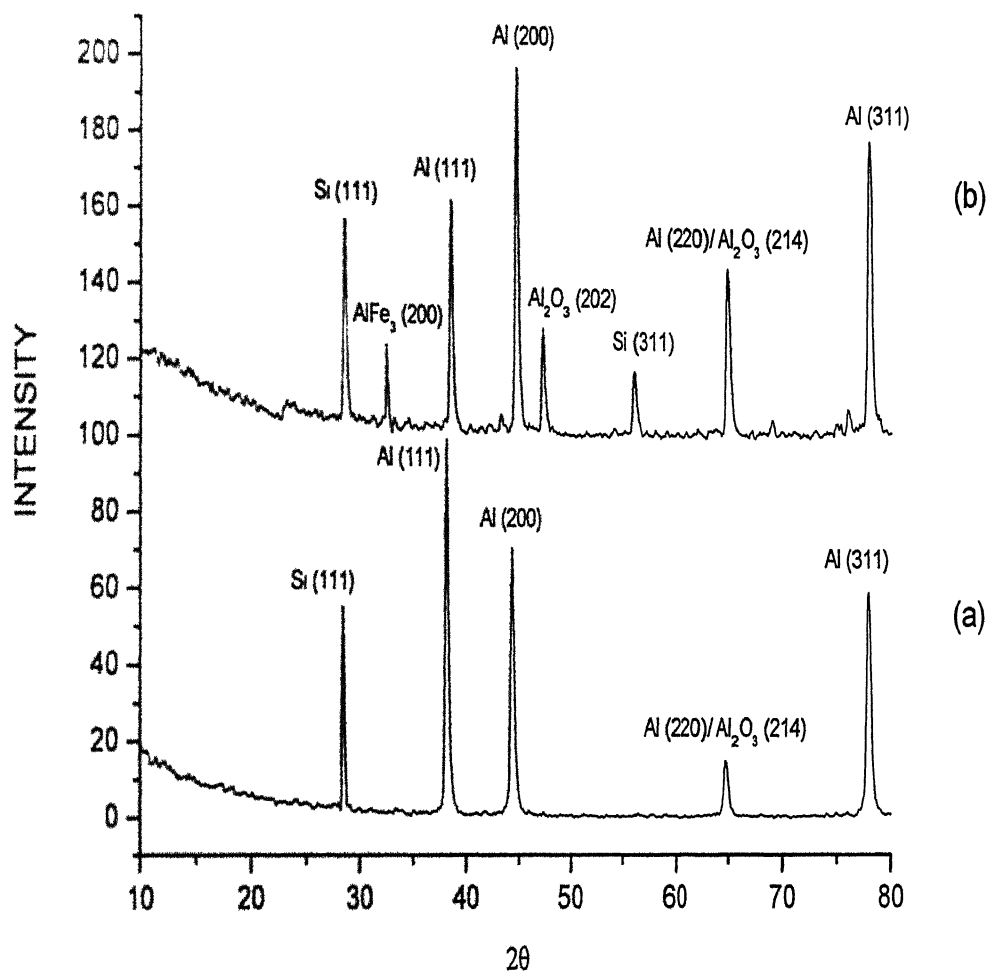
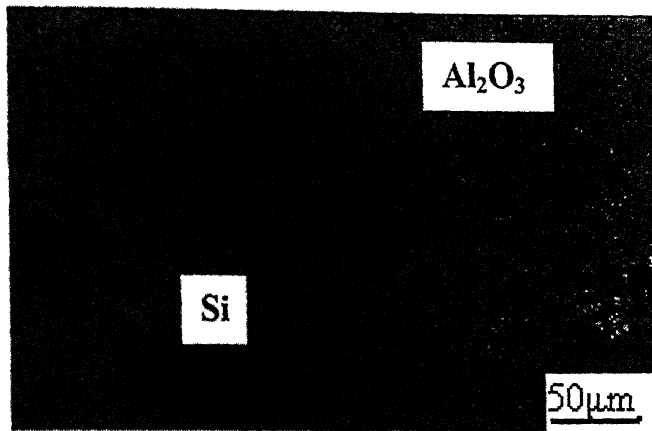
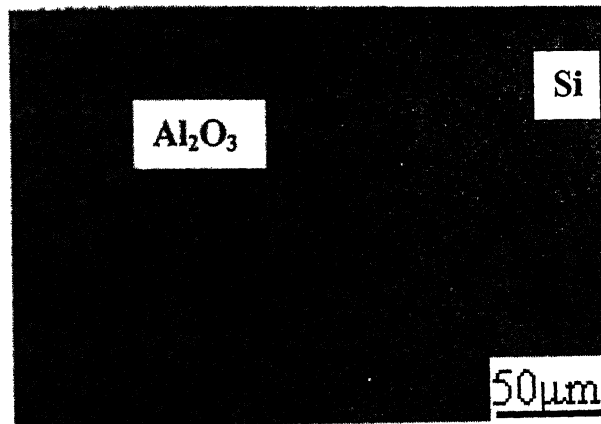


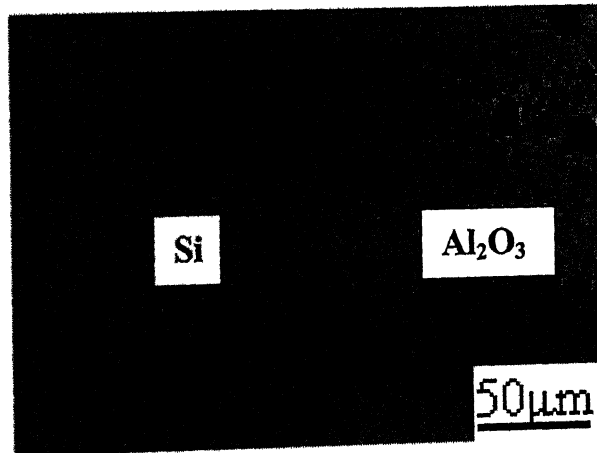
**Fig. 4.5** XRD pattern of cast Al-Si base alloy with 5% Fe<sub>2</sub>O<sub>3</sub> (a) at 800°C, (b) at 1100°C.



(a)



(b)



(c)

**Fig. 4.6** Shows the optical micrograph of cast Al- Si base alloy with 5%  $\text{Fe}_2\text{O}_3$  at 200 X. (a) at  $800^\circ\text{C}$ , (b) and (c) at  $1100^\circ\text{C}$ . Micrograph shows the presence of distributed alumina in the Al- Si matrix.

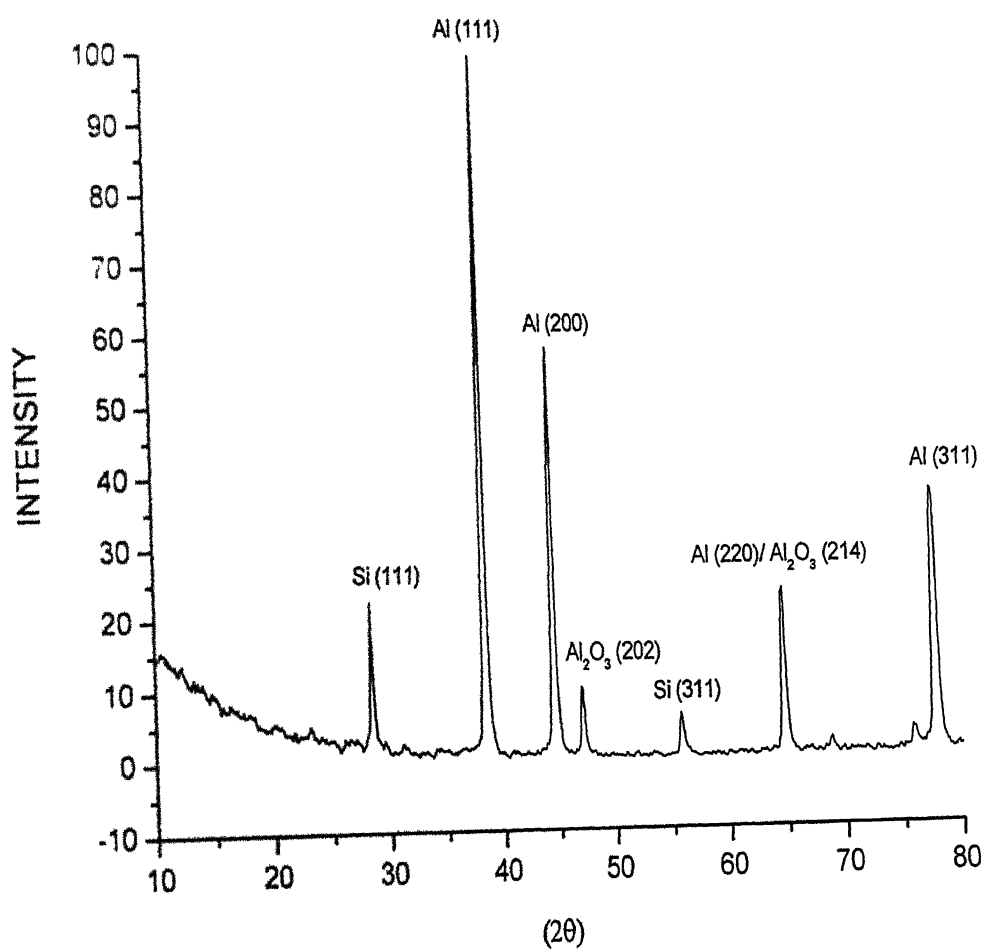
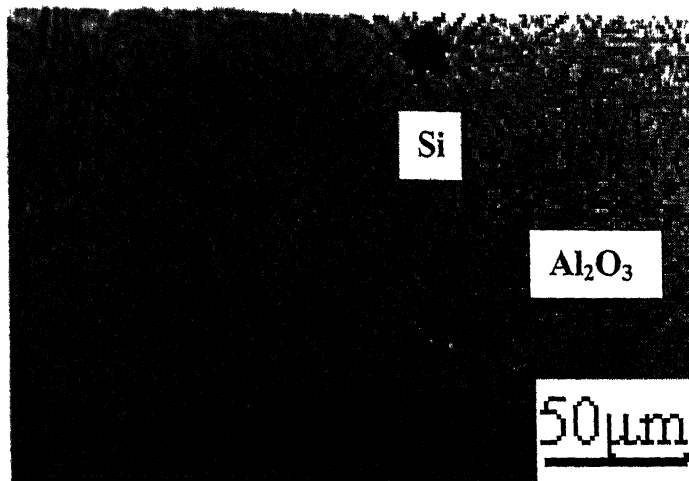
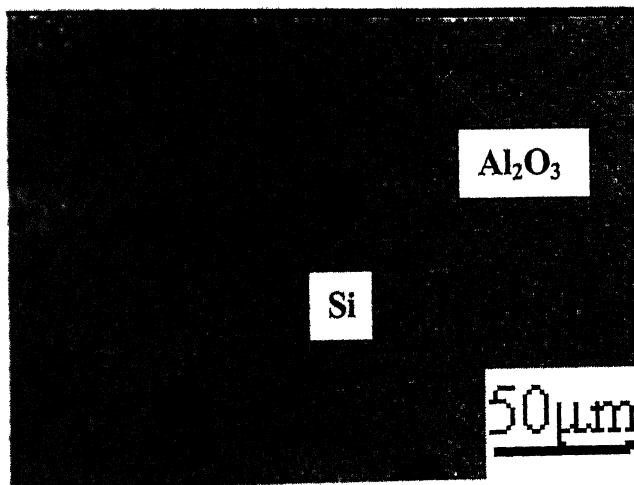


**Fig. 4.7** XRD pattern of cast Al-Si base alloy with 2% Fe<sub>2</sub>O<sub>3</sub> at 1100°C.



(a)



(b)

**Fig. 4.8** Shows the optical micrograph of cast Al- Si base alloy with 2%  $\text{Fe}_2\text{O}_3$  at 200 X. (a) and (b) both are at  $1100^\circ\text{C}$ . Micrograph shows the presence of distributed alumina in the Al- Si matrix.

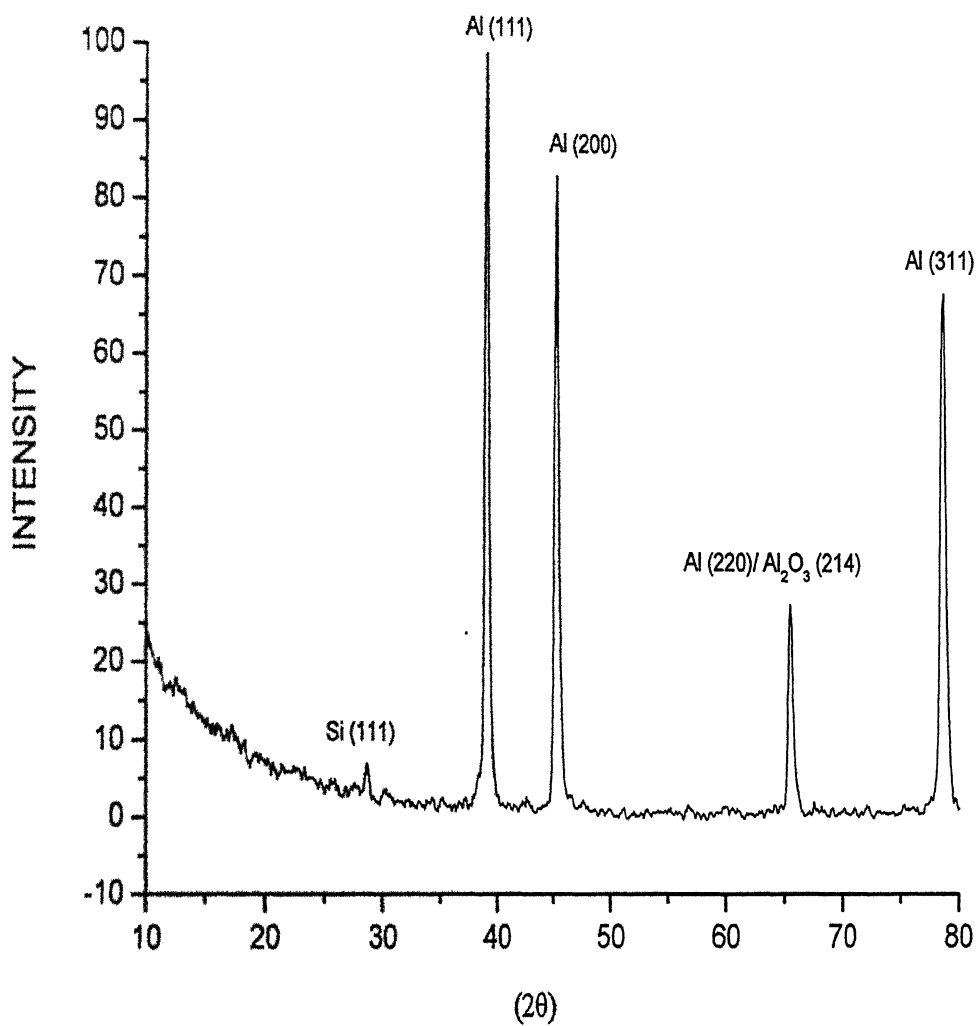
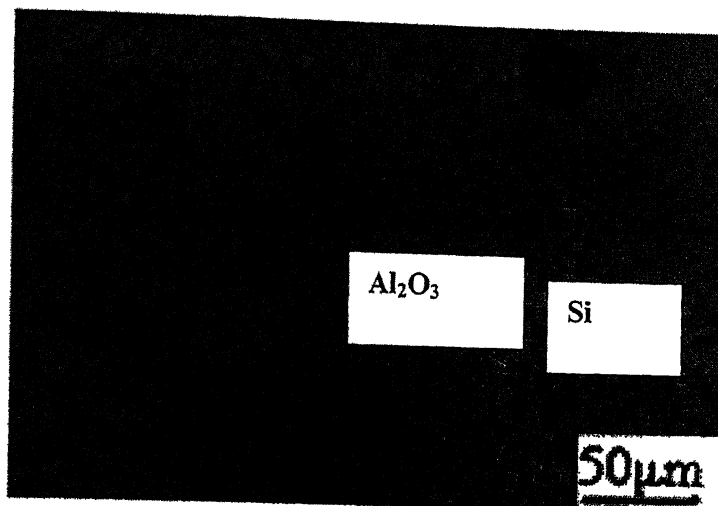
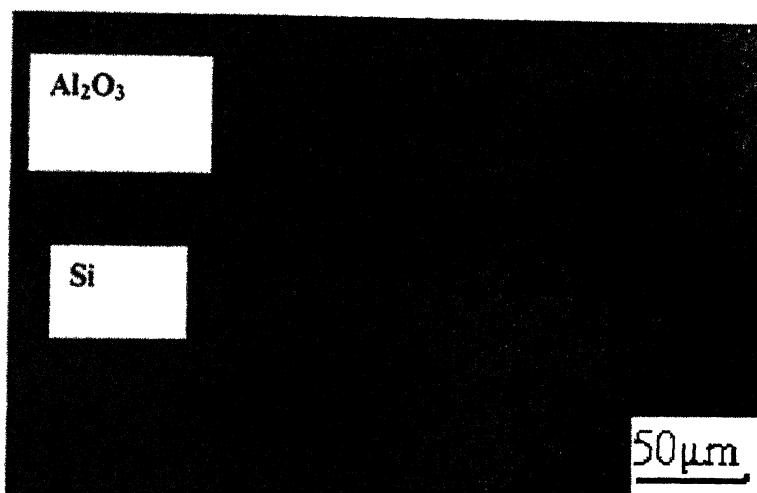


**Fig. 4.9** XRD pattern of cast Al-Si base alloy with 2% SiC at 1100°C.



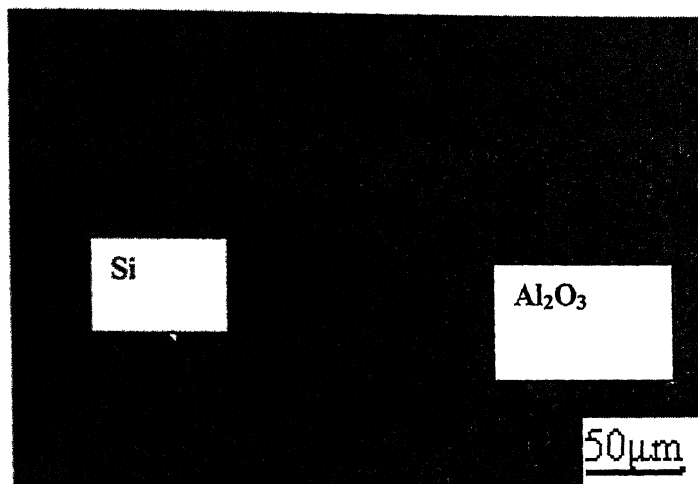


(a)

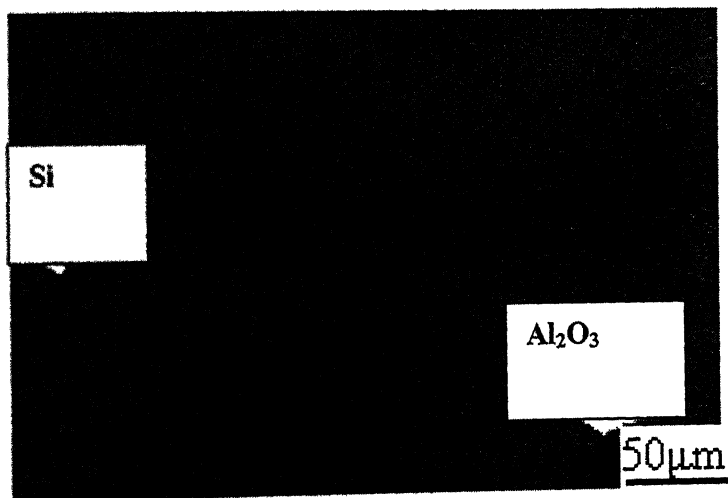


(b)

**Fig. 4.10** Shows the optical micrograph of cast Al- Si base alloy with 2% SiC at 200 X. (a) and (b) both are at 1100°C. Micrograph shows the presence of distributed alumina in the Al- Si matrix.



(a)



(b)

**Fig. 4.12** Shows the optical micrograph of cast Al- Si base alloy with 2%  $\text{Al}_2\text{O}_3$  at 200 X. (a) and (b) both are at  $1100^\circ\text{C}$ . Micrograph shows the presence of distributed alumina in the Al- Si matrix.

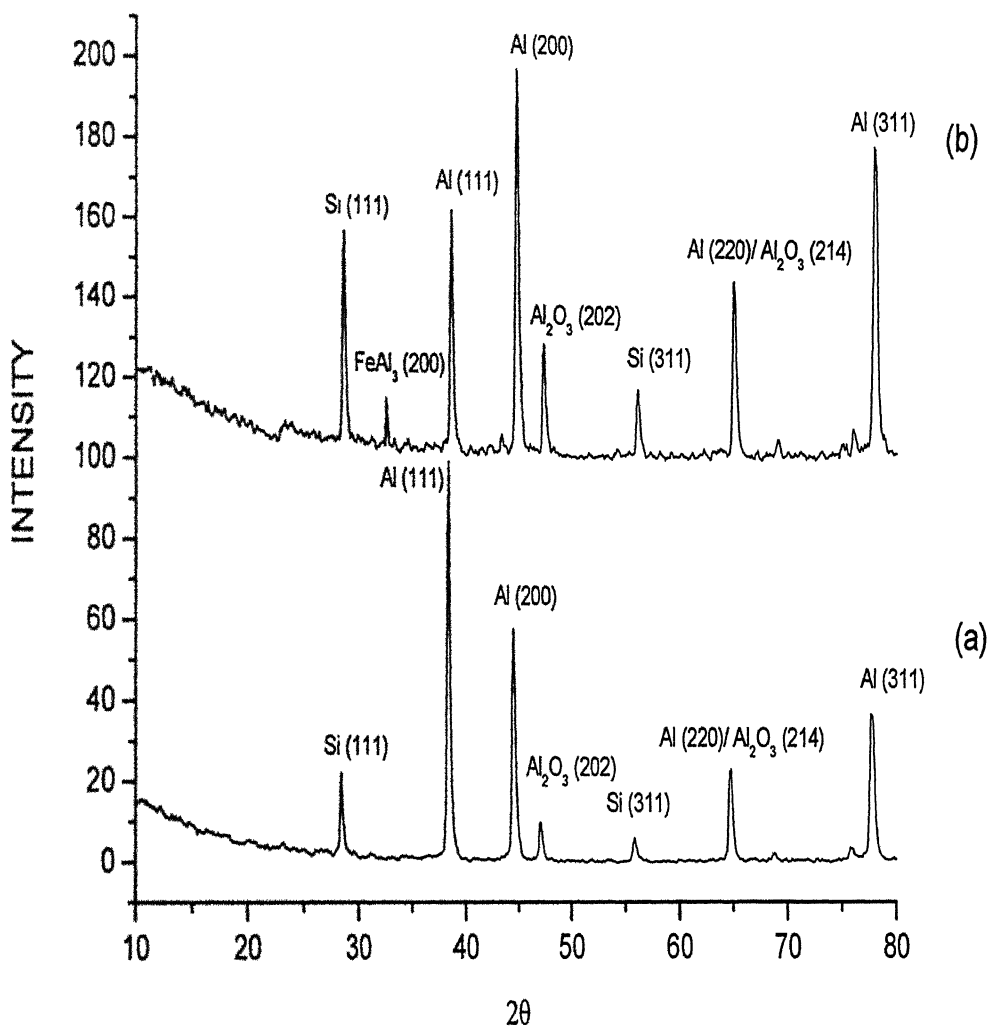


**Fig. 4.13** Comparison of XRD pattern between (a) 2 % (b) 5 %  $\text{Fe}_2\text{O}_3$  at  $1100^\circ\text{C}$

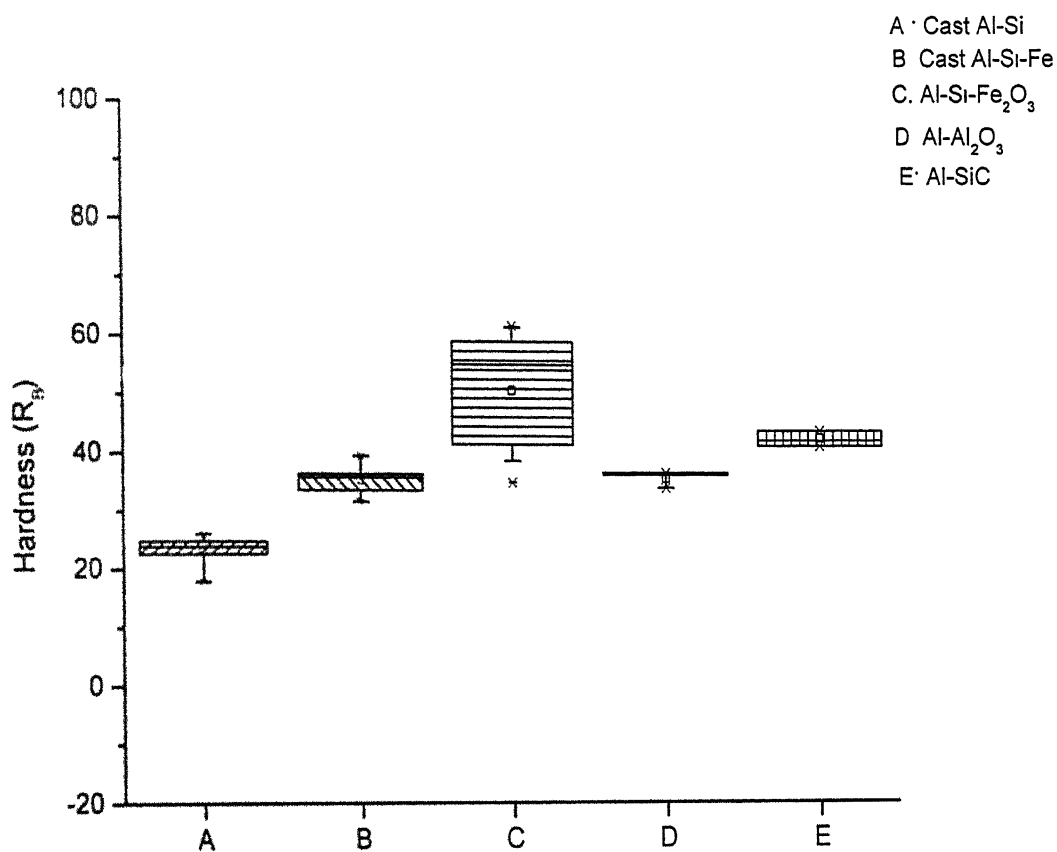


**Fig. 4.14** Hardness comparison of different samples prepared with different composition.

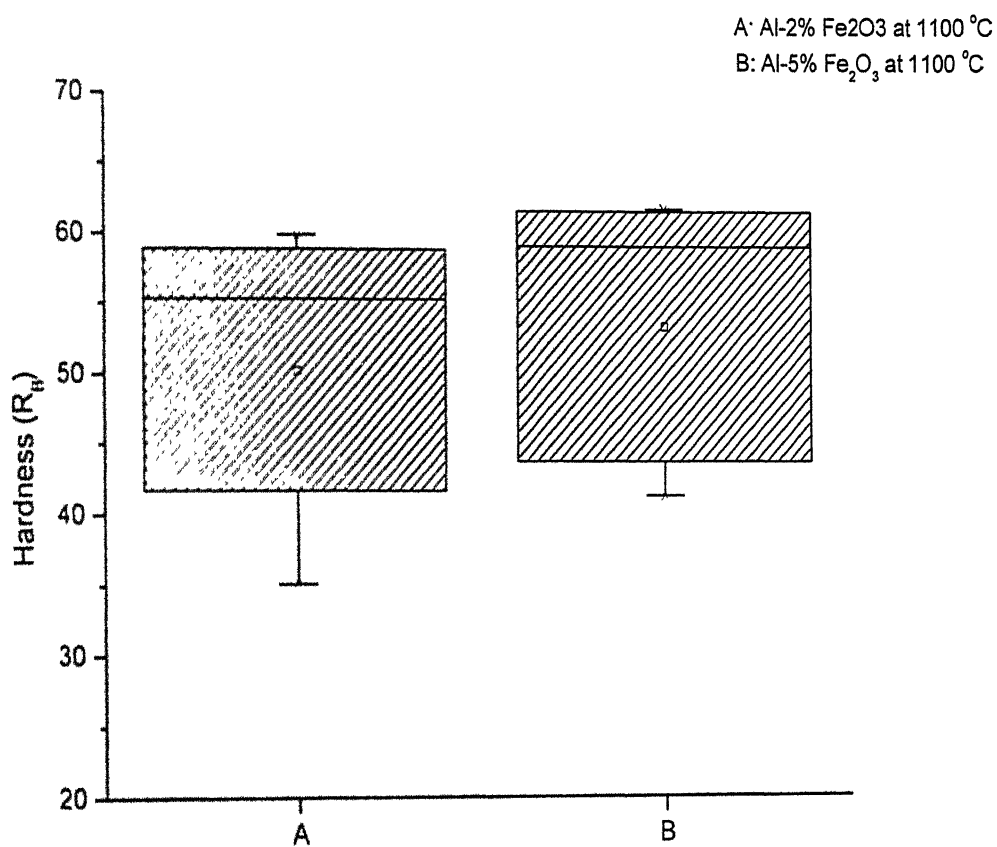


**Fig. 4.15** Hardness comparison of Al-Si- 2%  $\text{Fe}_2\text{O}_3$  and Al-Si- 5%  $\text{Fe}_2\text{O}_3$  at 1100°C.

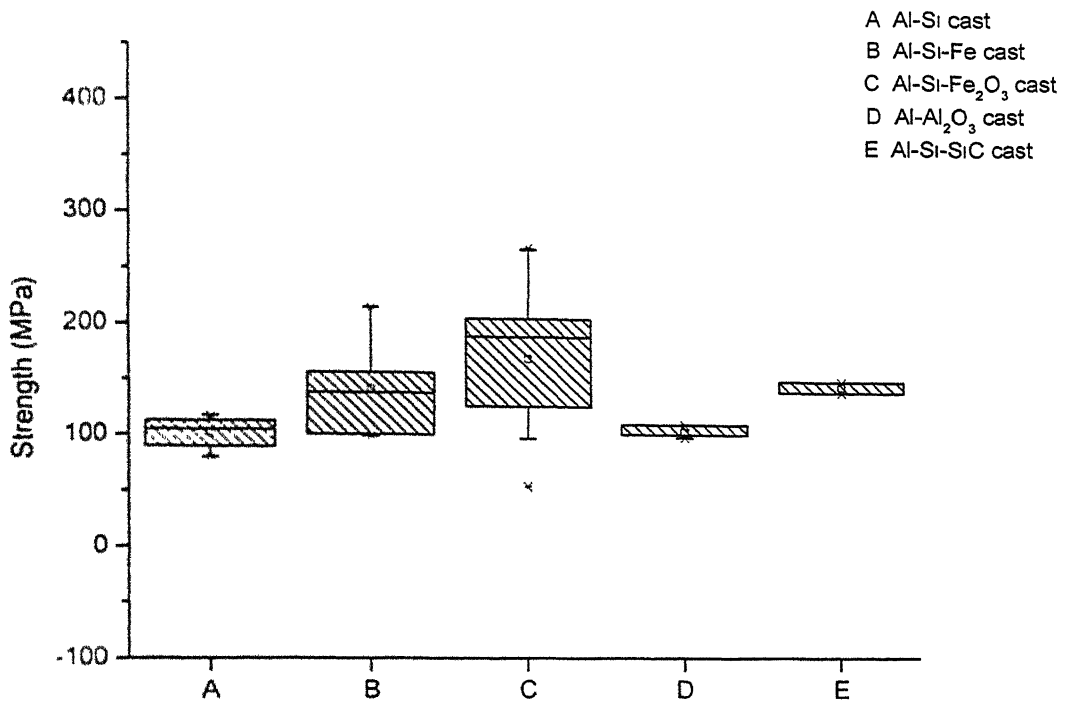


**Fig. 4.16** Strength comparison of different samples prepared with different composition.

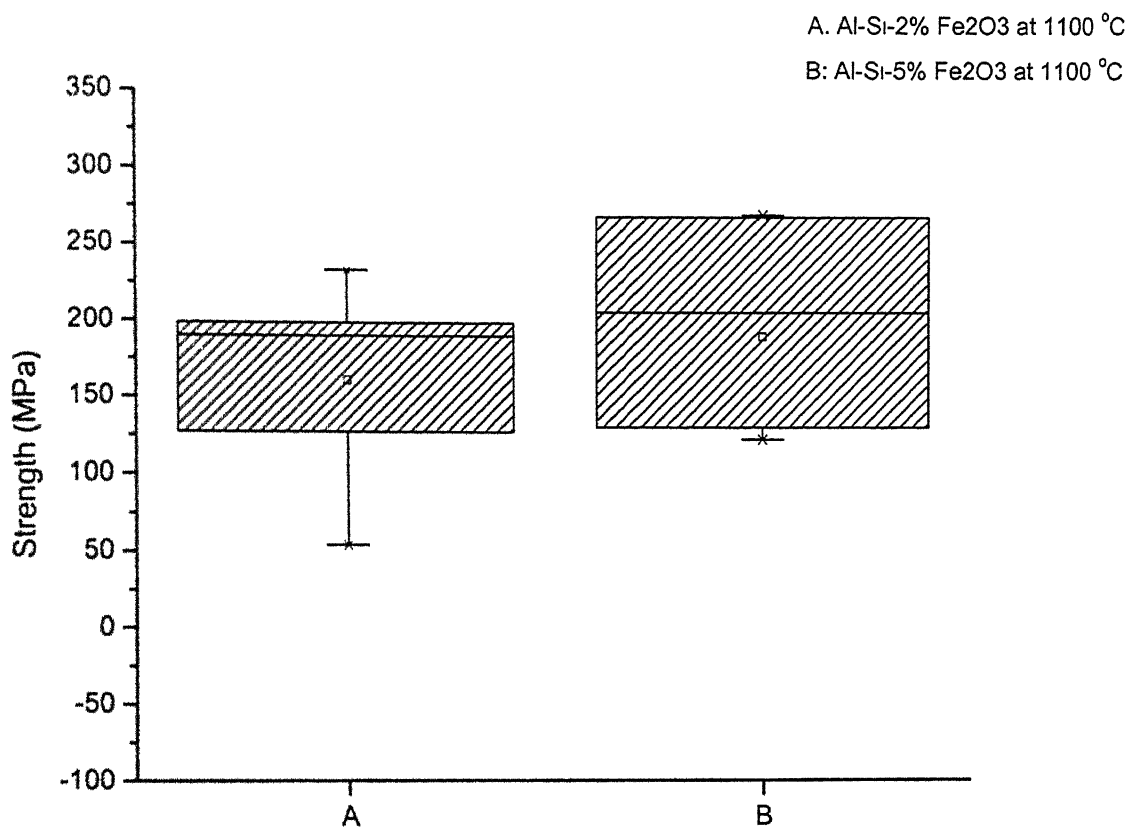


**Fig. 4.17** Strength comparison of Al-Si- 2% Fe<sub>2</sub>O<sub>3</sub> and Al-Si- 5% Fe<sub>2</sub>O<sub>3</sub> at 1100°C

Date Slip **A** 148415

[illegible]

44-38861-100